ANISOTROPIC SPIN RELAXATION IN MESOSCOPIC NONMAGNETIC CHANNELS

by

Fatih Kandaz

A dissertation submitted to the Faculty of the University of Delaware in partial fulfillment of the requirements for the degree of Doctor of Philosophy in Physics

Winter 2018

© 2018 Fatih Kandaz
All Rights Reserved

ANISOTROPIC SPIN RELAXATION IN MESOSCOPIC

NONMAGNETIC CHANNELS

by

Fatih Kandaz

Approved: _____
Edmund R. Nowak, Ph.D.
Chair of the Department of Physics and Astronomy

Approved: _____
George H. Watson, Ph.D.
Dean of the College of Arts and Sciences

Approved: _____
Ann L. Ardis, Ph.D.
Senior Vice Provost for Graduate and Professional Education

I certify that I have read this dissertation and that in my opinion it meets the academic and professional standard required by the University as a dissertation for the degree of Doctor of Philosophy.

Signed: _____

Yi Ji, Ph.D.
Professor in charge of dissertation

I certify that I have read this dissertation and that in my opinion it meets the academic and professional standard required by the University as a dissertation for the degree of Doctor of Philosophy.

Signed: _____

Edmund R. Nowak, Ph.D.
Member of dissertation committee

I certify that I have read this dissertation and that in my opinion it meets the academic and professional standard required by the University as a dissertation for the degree of Doctor of Philosophy.

Signed: _____

Qaisar Shafi, Ph.D.
Member of dissertation committee

I certify that I have read this dissertation and that in my opinion it meets the academic and professional standard required by the University as a dissertation for the degree of Doctor of Philosophy.

Signed: _____

Chaoying Ni, Ph.D.
Member of dissertation committee

ACKNOWLEDGMENTS

I would like to express my deepest appreciation to all those people who provided help to finish this dissertation.

First, I would like to thank my wife, Hatice, for her support, understanding and patience. She never failed to encourage me and stand behind me during difficult times. I also thank my wonderful children, Furkan Emir and Akif Emre. They were four and two years old at the time of writing this dissertation. I would have never been able to complete my Ph.D. research without their indefinite love and support. I am fortunate to have such a wonderful family.

Primarily I would like to thank my thesis advisor, Professor Yi Ji, for his professional guidance, encouragement and inspiration during my graduate studies at University of Delaware. I am grateful for his infinite patience, continuous help and motivation. He provided a comfortable and flexible research environment throughout my years in his group. This research project would not have been possible without his help and encouragement.

Next I would like to thank my thesis committee members: Professor Edmund Nowak, Professor Qaisar Shafi, and Professor Chaoying Ni for all of their guidance and help through my Ph.D. study. Special thanks for Professor Nowak for his supervision in the beginning of my graduate carrier and letting me use his lab and equipment for this study.

I would like to thank my lab mates, Dr. Shuhan Chen, Dr. Chuan Qin, Yunjiao Cai, Xingyu Shen, and Kevin Haughey. They are always kind and considerate to me

throughout my graduate school experience. I specially thank to Chuan and Yunjiao for valuable discussions and contributions to my studies. I also thank to our collaborators: Professor Yizheng Wu, Chao Zhou, and Mengwen Jia from Fudan University and Professor Zhe Yuan from Beijing Normal University for their help and contributions to my Ph.D. research.

I acknowledge all staff members and graduate students at the department of Physics and Astronomy for their friendship, support and assistance throughout the graduate program.

I would also like to thank all of my friends in Delaware for sharing life and experience during my years in Newark, DE. We have shared so many memories together and I will not forget them.

I am grateful to the Ministry of National Education of Republic of Turkey for supporting me to study and complete my Ph.D. in the U.S. I would also like to thank The Scientific and Technological Research Council of Turkey (TUBITAK) for supporting me in the beginning of my graduate years.

Last but not the least, I thank my family for their support and encouragement all these years. My parents, my brothers, my sister, my parents in law and my sisters in law made my life so beautiful. I want to give special thanks to Busra Ozbay for her help and encouragement. I am deeply thankful to all of my family members for their support.

TABLE OF CONTENTS

LIST OF FIGURES ix
ABSTRACT xvi

Chapter

1 INTRODUCTION 1

REFERENCES 6

2 BACKROUND OF NONLOCAL SPIN VALVES AND SPIN RELAXATION MECHANISMS 8

2.1 Introduction to Spintronics 8

2.1.1 Giant Magnetoresistance (GMR) 8
2.1.2 Spin Valve 11
2.1.3 Tunneling Magnetoresistance (TMR) 16

2.2 Introduction to Nonlocal Spin Valve 18

2.2.1 Generation of Pure Spin Current 20
2.2.2 Nonlocal Spin Valve Measurements 21
2.2.3 Principles of Nonlocal Spin Valves 24

2.3 Spin Relaxation Mechanisms 29

2.3.1 Elliot-Yafet Spin Relaxation Mechanism 30
2.3.2 D'yakonov-Perel' Spin Relaxation Mechanism 32

2.4 Spin-Orbit Coupling 34

2.4.1 Rashba Spin-Orbit Coupling 35

REFERENCES 39

3 DEVICE FABRICATION AND MEASUREMENT TECHNIQUES 43

3.1 Fabrication and Measurement Steps 43
3.2 Lithoghraphy 43

3.2.1 Photolithography 44

3.2.1.1 Cleaning of the Wafer 46
3.2.1.2 Spin Coating 46
3.2.1.3 Light Exposure 47
3.2.1.4 Development 47
3.2.1.5 Deposition and Lift-off 47

3.2.2 Electron Beam Lithography 48

3.2.2.1 Double Layer Shadow Mask 48

3.3 Electron Beam Evaporation 52

3.3.1 Principles 52
3.3.2 Electron Beam Evaporation Process 52
3.3.3 Shadow Evaporation Method 55

3.4 Experimental Setup for Spin transport Measurements 59

3.4.1 Wire Bonding 59
3.4.2 Electrical Measurements 60

REFERENCES 65

4 ANISOTROPIC SPIN RELAXATION IN MESOSCOPIC NONMAGNETIC CHANNELS INDUCED BY SURFACE SPIN-ORBIT EFFECTS 66

4.1 Introduction 66
4.2 Sample Fabrication and Measurement Setup 69
4.3 Experiments 71

4.3.1 Anisotropic Spin Signals 75
4.3.2 Anisotropic Signal Measurements by Sweeping Magnetic Field 76
4.3.3 Anisotropic signal measurements by Rotating Sample under the Fixed Magnetic Field 77

4.3.3.1 Baseline of the R_s versus B Curves and Implications on Measurements 79

4.3.4 Anisotropic Signal Measurements under the Rotational Magnetic Field 81

4.4 Origin of Anisotropic Effects 84
4.5 Discussion and Theory 90
4.6 Conclusions 100

REFERENCES 101

5 UNSOLVED QUESTIONS AND FUTURE WORK 106

5.1 Unsolved Questions 106
5.2 Suggestions for Future Work 109

REFERENCES 115

6 CONCLUSION 116

REFERENCES 119

Appendix

REPRINT PERMISSION LETTERS 120

LIST OF FIGURES

Figure 1.1: An illustration of a three-dimensional nonlocal spin valve device. Pure spin current is generated in the nonmagnetic channel and clearly detected. Reprinted with permission from [18]. Copyright 2013 Macmillan Publishers Limited. 4

Figure 2.1: a) Schematic diagram of a magnetic multilayer GMR b) Giant magnetoresistance effect as reported by Baibich et al. Resistivity change as a function of applied magnetic field. (b) is reprinted with permission from [5]. Copyright 1988 by the American Physical Society. 10

Figure 2.2: A schematic representation of electron transport in a spin valve based on the GMR effect: (a) In the parallel magnetic configuration only one spin type of electrons strongly scatter, which leads to lower resistance; (b) In the anti-parallel magnetic configuration both spin type of electrons strongly scatter which leads to higher resistance; (c) a typical magnetoresistance curve for spin valves. 12

Figure 2.3: Schematic diagrams of (a) CIP (current in plane) and (b) CPP (current perpendicular to plane) GMR spin valves (with NM spacer). MTJ's are similar to CPP configurations, but in these devices a thin layer of an insulator replaces the NM material in spacer layer. 15

Figure 2.4: Schematic representation of TMR effect in MTJs: (a) MTJ structure is shown for parallel (left) and antiparallel (right) alignments of the ferromagnetic layers. (b) Density of states schematic for spins of electrons tunneling process in P (left) and AP (right) configurations of MTJs. The density of states of both FM layers determines how large the electrons tunnel through insulator layer. 17

Figure 2.5: Illustration of the difference between unpolarized charge current, spin-polarized charge current and pure spin current. 19

Figure 2.6: The geometry of the spin injection experiment on a single crystal aluminum bar. Reprinted with permission from [33]. Copyright 1985 by the American Physical Society. 21

Figure 2.7: Non-local magnetoresistance measurement. (a) Scanning electron microscope image of a spin valve. (b) Schematic representation of the non-local spin valve structure. (c),(d) The measurement of the non-local spin signal at 293 K and 4,2 K respectively. Reprinted with permission from [34]. Copyright 2001 Macmillan Magazines Limited. 22

Figure 2.8: Non-local spin signal measurement: (a) SEM image of the sample. Aluminum wire is designed perpendicular to the two parallel cobalt wires. (b) Non-local resistance versus magnetic field curve at 4.2 K and 293 K. Reprinted with permission from [35]. Copyright 2002 Macmillan Magazines Limited. 23

Figure 2.9: Concept of the non-local spin valve. (a) Top view. (b) Side view. A schematic diagram of a non-local spin valve device. The charge current is injected from F_1 through the left end of the NM channel. The nonlocal voltage is detected between F_2 and the right end of the NM channel. (c) Schematic representation of densities of states for spin-up and spin down bands in F_1, N and F_2 in the NLSV geometry. Nonlocal spin resistance ΔR_s is determined by dividing the nonlocal voltage ΔV_{nl} by the injected current I_e. 25

Figure 2.10: Illustration of non-local spin signal within the magnetic field along the FM electrodes. The pairs of green arrows indicate magnetization states of F_1 and F_2. Blue solid line shows the spin resistance as a function of magnetic field, swept from the negative to positive field values. Red line corresponds to the swept magnetic field in the opposite direction. 27

Figure 2.11: Illustration of Elliot-Yafet spin relaxation mechanism. When the spins of electrons scatter through the Elliot-Yafet mechanism, spin-relaxation rate is directly proportional to the momentum scattering rate. 31

Figure 2.12: Illustration of D'yakanov-Perel spin relaxation mechanism. when the spins of electrons scatter through the D'yakanov-Perel mechanism, spin-relaxation rate is inversely proportional to the momentum scattering rate. 33

Figure 2.13: Schematic representations of the electronic band structure (a) Sketch of the Rashba spin-orbit effective magnetic fields and momentum directions at the surface. The effective magnetic field tends to align electron spins (red arrows) with the direction of the field, which is perpendicular to the electron's momentum (blue arrows). (b), (c) A schematic representation of the energy dispersion in 2D free electron gas model (b) in the absence of Rashba spin-orbit coupling, electrons with up spin and down spin are degenerate. (c) in the presence of Rashba spin-orbit coupling. Spin degeneracy is lifted because of the spin-orbit coupling the two bands carry opposite spins, shown by the orange and light blue arrows. Circular dots in (a) shows Fermi surface of this two-dimensional free electron gas with Rashba effect. 36

Figure 3.1: Flowchart shows the steps of sample fabrication. 44

Figure 3.2: Flowchart of a positive photolithography process (a) Si Substrate; (b) A positive photoresist is spun onto Si substrate; (c) The photoresist is exposed to UV light through a photomask; (d) After the development of photoresist; (e) desired material is deposited onto the substrate; (f) the material on the remaining resist are removed by lift-off of the resist. 45

Figure 3.3: (a-e) Electron beam lithography for fabrication of double layer shadow mask; (f) & (g) two different structures can be separated on the substrate by angle evaporation of the materials through a shadow mask; (h) after lift-off of remaining resists, desired patterns are left on the substrate. 49

Figure 3.4: (a) & (b) Optical microscope image and an illustration of the structure after the development of the top layer (PMMA); (c) & (d) Optical microscope image and an illustration of the shadow mask after the development of the bottom layer (PMGI). 51

Figure 3.5: A schematic diagram of electron beam evaporation process. Figure is adapted from [2]. 53

Figure 3.6: (a) A schematic diagram for a high vacuum deposition chamber. The three slits on the sample represent the magnified designed pattern for e-beam lithography. The materials are evaporated through those openings from different angles θ; b) Schematic representation of the six crucibles; only one of these target materials are deposited at a time, the other five are under the self-seal protector. 54

Figure 3.7: Schematic representation of the multi angle shadow evaporation technique in the fabrication of nonlocal spin valve structures; (a) & (b) Shadow evaporation of Py electrodes from two orientations at an angle θ to the substrate normal (c) & (d) Evaporation of AlO_x and Cu through normal direction so that the materials overlap to create a lateral spin valve device. Figure is adapted from [3]. 57

Figure 3.8: Scanning Electron Microscopy (SEM) images of a fabricated lateral spin valve device. 58

Figure 3.9: (a) A typical wire bonded substrate, contact pads of the devices is connected to the chip carrier with Al wires; (b), (c) & (d) the nonlocal spin valve devices on the substrate, (d) the image of an NLSV device from SEM microscopy. 59

Figure 3.10: Block diagram of the measurement setup performed in this work. Green lines indicate electric signals and blue lines indicate GPIB signals; (b) Schematic diagram of a cryogenic system for the low temperature measurement, the wire bonded substrate is mounted on the sample holder..... 61

Figure 3.11: Schematic diagram for the anisotropic spin signal measurement under the fixed magnetic field as the NLSV device is rotated between (a) 0^o position and (b) 90^o position periodically to alternate the aligned spins between the directions perpendicular to Cu channel and parallel to Cu channel, respectively. The 3-D diagrams at the bottom show the directions of the spins in the nonlocal spin valve devices for each case. The spins are directed along the direction of the applied magnetic field..... 63

Figure 4.1: Illustration of anisotropic spin transport. On the left NLSV, the spins are aligned in the x direction, which is perpendicular to the direction of spin current. On the right NLSV, the spins are aligned in the y direction, which is parallel to the direction of spin current. 68

Figure 4.2: (a) SEM image of an NLSV with L=470 nm. (b) Angle evaporation of NLSV structure through a mesescopic shadow mask. Adapted from [53]. (c) The R_s versus B curve at 295 K. 70

Figure 4.3: Spin signal ΔR_s as a function of channel length L at RT. Solid red line shows the fitting by the equation 4.1..... 73

Figure 4.4: (a) Cartoon illustration of x direction and y direction magnetic fields applied to an NLSV (on the left). (b) The R_s versus B_x curve for a typical NLSV at 10 K, and illustration of P and AP states for x spins and y spins. The R_s values of the P state and antiparallel state are symmetrical to the baseline. Copyright 2017 by the American Physical Society. 74

Figure 4.5: (a) The F_1 and F_2 of the NLSV are designed to make small but opposite angles (±3°) with the x direction. (b) The R_s versus B curves for this NLSV at 295 K, with field applied along the x direction (blue) and the y direction (red). Copyright 2017 by the American Physical Society. 76

Figure 4.6: (a) Illustrates the rotation of the NLSV relative to the fixed magnetic field, the spins alternate between the $+x$ and $+y$ directions periodically. (b) The R_s versus time plot at 295 K while the NLSV (the same as in Fig. 4.5) is rotated between 0° and 90° under a 0.2-T magnetic field. Copyright 2017 by the American Physical Society. (c) The R_s versus time plot while the same NLSV is rotated between 0° and 90° under zero magnetic field. 78

Figure 4.7: (a) Illustration of a fixed bias field B_{bias} in the x direction and an applied field that can be oriented either in the x direction or in the y direction. (b) The R_s versus B_x curve with applied field in the x direction in the presence of the bias field. Due to bias field, the spins are aligned well into a P state even at $B_x = 0$. (c) and (d) are measurements with applied field B_y in the y direction while bias field is still along x direction. (c) The applied field B_y as a function of time (d) The measured signal R_s as a function of time. The measurements in this figure are carried out at 10 K. Copyright 2017 by the American Physical Society. 82

Figure 4.8: (a) Calculated percentage signal change (ΔRsy-ΔRsx)ΔRsx as a function of L for various values of λ_x. The anisotropic change of λ is assumed to be $(\lambda_y - \lambda_x) / \lambda_x = 10\%$ (b) The same results as in (a) are plotted as a function of normalized channel length L/λ_x. Three curves collapse onto a single curve. Copyright 2017 by the American Physical Society. 84

Figure 4.9: The percentage anisotropic signal, (ΔRsy-ΔRsx)ΔRsx, as a function of (a) L and (b) L/λ_x at 10 K for NLSVs on substrate A. The percentage anisotropic signal, (ΔRsy-ΔRsx)ΔRsx, as a function of (c) L and (d) L/λ_x at 10 K for NLSVs on substrate B. The shaded areas in (c) and (d) are calculation by randomized parameters in the range: $\lambda_x = 670 \pm 180$ nm and $(\lambda_y - \lambda_x) / \lambda_x = (9\pm5)\%$. (e) The plot of (ΔRsy-ΔRsx)ΔRsx versus L/λ_x for NLSVs on both substrates A (blue symbols) B (red symbols). The solid line in (b) and (e) are guidance to eyes. (a-d) Copyright 2017 by the American Physical Society..... 86

Figure 4.10: (a) The spin-diffusion length λ_x versus resistivity ρ for substrate A at 10 K and the fit (solid line) by Elliott-Yafet model (b) The λ_x versus ρ plot and fit (solid line) for substrate B at 10 K. The λ_x value on the fitted curve is used to determine normalized distance L/λ_x in Figure 4.9. Copyright 2017 by the American Physical Society..... 87

Figure 4.11: The estimated anisotropic change in spin diffusion length $(\lambda_y - \lambda_x)$ at 10 K is plotted as a function of estimated λ_x for NLSVs on (a) substrate A and (b) substrate B. The percentage change $(\lambda_y - \lambda_x) / \lambda_x$ versus λ_x at 10K for (c) substrate A and (d) substrate B. The dashed lines indicate average values. 89

Figure 4.12: Calculated spin accumulation in bulk Cu as a function of distance from the Py/Cu interface. While the upper data are obtained using the real SO strength of bulk Cu, the lower ones are calculated with the SO strength artificially increased by a factor of 7. In both cases, the spins parallel to the spin-current direction (y spins, red symbols) are the same as the spins perpendicular to it (x spins, blue symbols), indicating the bulk SO interaction does not introduce the anisotropic spin relaxation. Copyright 2017 by the American Physical Society. 91

Figure 4.13: Surface spin-orbital effects. When electrons are scattered by a surface, the spin-flip probabilities are higher for spins perpendicular to the surface than for spins parallel to surface. (a) Scattering rate for x spins (on the left) is larger than scattering rate for y spins (on the right) on the side surfaces. (b) Scattering rate for x spins (on the left) is equal to scattering rate for y spins (on the right) on the top/bottom surfaces. 94

Figure 4.14: Sketch of the SO effective magnetic fields at the side and top surfaces of a Cu channel. Copyright 2017 by the American Physical Society. 96

Figure 5.1: (a) The R_s versus B_y curve. (b) The R_s versus time plot at 295 K while the same NLSV is rotated between 0°, 90°, 180°, and 270° under a 0.2-T magnetic field. c) Illustrates the rotation of the NLSV relative to the fixed magnetic field, the spins alternate between the +*x*, +*y*, -*x*, and –*y* directions. 106

Figure 5.2: (a) Illustration of a fixed bias field B_{bias} in the *x* direction. (b) The applied field in *y* direction B_y as a function of time and the R_s as a function of time. 107

Figure 5.3: (a) The (Rs + y-Rs-y)ΔRsx versus L/λ_x for NLSVs on substrate A. (b) The (Rs + y-Rs-y)ΔRsx versus L/λ_x for devices on substrate B..... 108

Figure 5.4: Illustration of anisotropic spin transport. The spins are aligned in the (a) *x*, (b) *y*, and (c) *z* direction. 110

Figure 5.5: Illustration of anisotropic effects as changing the dimensions of Cu channels. (a) 300-nm thick and 100-nm wide Cu channel should have little influence from the top and bottom surfaces. (b) 30-nm thick and 300-nm wide Cu channel should have little influence from the side surfaces. 112

ABSTRACT

Spin–orbit (SO) effects, which are essential for spintronics, not only generate spin currents and spin torques but also provide ways to modulate spin currents. However, SO effects induce higher rates of spin relaxation and therefore lead to shorter spin-relaxation lengths in materials. This contradicts the general desire for a longer spin-relaxation length to transport a spin current over distance. In this work, we demonstrate that substantial surface spin-orbit effects and a long spin-relaxation length can coexist in mesoscopic Cu channels.

It is a common perception that the transport of a spin current in polycrystalline metal is isotropic and independent of the polarization direction, even though spin current is a tensorlike quantity and its polarization direction is a key variable. We demonstrate surprising anisotropic spin relaxation in mesoscopic polycrystalline Cu channels in nonlocal spin valves. For directions in the substrate plane, the spin-relaxation length is longer for spins parallel to the Cu channel than for spins perpendicular to it, by as much as 9% at 10 K. Spin-orbit effects on the surfaces of Cu channels can account for this anisotropic spin-relaxation. The finding suggests novel tunability of spin current, not only by its polarization direction but also by electrostatic gating.

Chapter 1

INTRODUCTION

Conventional electronics is based on only the electron's charge and the resulting electric current when charge flows. The density of electronic devices is described by the Moore's law [1], which states that the number of transistors per square inch doubles in every 18 months. However, as the density of transistor increases, power dissipation and heat management become a serious problem and miniaturization of the transistors eventually becomes unsustainable. An alternative solution to this issue is spintronics, which relies on the electron spin in addition to or in place of electron charge. An electron spin is an intrinsic quantum property of the electrons and it can have only two possible spin values, $m_s = 1/2$ or $m_s = -1/2$, known as spin-up and spin-down states.

The field of spintronics has shown remarkable progress in both fundamental science and technological applications. Discovery of the giant magnetoresistance, which is a spin-dependent transport phenomenon in magnetic/nonmagnetic metallic multilayer structures, has been deemed as the birth of the spintronics. Albert Fert [2] and Peter Grunberg [3] received the 2007 Nobel Prize for the discovery of giant magnetoresistance in 1988. Giant magnetoresistance is the large change in electrical resistance in magnetic/nonmagnetic multilayer systems depending on the relative orientation of magnetizations of the ferromagnetic layers. This new technology is used in GMR magnetic sensors and read heads of the hard disc drives in our computers. After the discovery of GMR, even larger magnetoresistance effect, tunneling

magnetoresistance (TMR), is reported at room temperature in 1995 [4,5] in a similar system in which the non-magnetic metal between the two layers of magnetic materials is replaced by a thin insulating tunnel barrier. The discoveries of GMR and subsequent TMR led to a very rapid increase in magnetic storage densities in hard disc drives and triggered the idea of novel non-volatile magnetoresistive memories, also known as Magnetic Random Access Memories (MRAM).

More recently, spin transfer torque (STT) effect, which has an influential impact on the designing of modern spintronic devices, was theoretically predicted [6,7] in 1996 and experimentally observed [8,9] in 1998. STT is an effect in which the magnetization orientation of a magnetic layer in GMR spin valves or magnetic tunnel junctions (MTJ) structures can be changed by using a spin-polarized current, instead of an external magnetic field. The discovery of STT has enabled a new generation of Magnetic Random Access Memories, known as STT-RAM or STT-MRAM, with the advantages of improved scalability and durability, lower power consumption and high access speed. Scientists are now excited by the prospect that emerging memory devices may eventually enable the integration of memory with logic circuits in computers, which will significantly increase compute density while also reducing the energy consumption.

In recent years, basic and fundamental research in spintronics field has increased our knowledge and achieved surprising and exciting results which may lead to new applications. In particular, spin-orbit interaction has attracted considerable interest. For example, symmetry breaking in magnetic materials and spin-orbit interaction give rise to chiral domain walls and magnetic skyrmions, which are promising in the next generation spintronic devices as information carriers. Other

spin-orbit interactions generate spin current and provide an efficient magnetic switching on ferromagnets via spin-orbit torques. Furthermore, spin-orbit effects offer the prospect of modulation of spin currents via electrostatic gating [10–13].

Spin-orbit interactions induce higher rates of spin relaxation and thereby shorter spin-relaxation length. However, long spin-relaxation length and substantial spin-orbit effects are both highly desirable. While the former enables efficient transport of a spin current over a distance in spintronic circuits, the latter allows for effective modulation of spin currents using an electrostatic gate [10–13]. In semiconductor spintronics, ballistic channels of two-dimensional electron gas have been used to overcome the spin relaxation while maintaining spin-orbit effects [10,11]. It was also proposed theoretically two opposite types of SO effects in group III – V semiconductors can quench the spin relaxation [14–16]. Overall, the exclusive nature of long spin-relaxation length and SO interactions remain a challenge.

Mesoscopic channels are unique in bringing together these two traits. While the surfaces of channels break the inversion symmetry and give rise to Rashba effects [17], the interior is free from SO effects and preserve a long spin-relaxation length. In this dissertation, spin-orbital effects on the surfaces of mesoscopic metallic Cu channels have been explored in the presence of long spin-relaxation length (larger than 600 nm). For this study, anisotropic spin transport measurements are carried out in nonlocal spin valve (NLSV) structures. An NLSV is a unique lateral structure consisting two ferromagnetic electrodes bridged by one mesoscopic nonmagnetic channel. Figure 1.1 illustrates a typical nonlocal spin valve structure. The spin accumulation in the ferromagnetic material is injected into the mesoscopic nonmagnetic channel and the gradient of the spin accumulation drives a pure spin

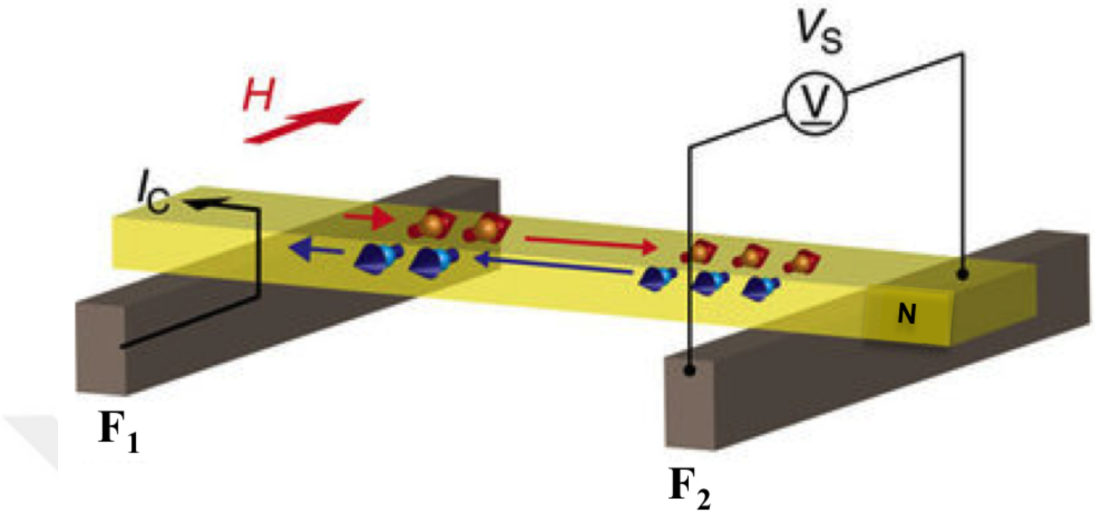

Figure 1.1: An illustration of a three-dimensional nonlocal spin valve device. Pure spin current is generated in the nonmagnetic channel and clearly detected. Reprinted with permission from [18]. Copyright 2013 Macmillan Publishers Limited.

current along the channel. We performed anisotropic measurements for two different spin polarization directions, and observed that the spins polarized along the Cu channel have different spin-relaxation length than the spins polarized perpendicular to Cu channel. Therefore, we demonstrated that spin relaxation is anisotropic and depends on the spin orientations. This effect is attributed to spin-orbital effects on the surfaces of Cu channel. The rare combination of the spin-orbit effects and the long spin-relaxation length (600 nm to 1500 nm) inspires the possibility of electrical modulation of large spin currents in mesoscopic Cu channels.

This dissertation is organized in five chapters. Chapter 1 gives a general introduction to spintronics and emphasizes the motivation of the study. Chapter 2 reviews fundamental concepts and theories of spintronics, including nonlocal spin

valves and spin-orbit interactions to construct a background. Chapter 3 describes the experimental techniques and detailed sample fabrication processes to generate nonlocal spin valve devices. Then the electrical measurement setup and anisotropic measurement techniques will be described. Chapter four introduces the main research outcomes about anisotropic spin relaxation in mesoscopic Cu wires. In this chapter, NLSV structures are used for spin transport measurements and different magnitudes of spin signals are observed depending on the polarization direction of spins in Cu channels. We have performed quantitative data analysis and concluded that anisotropic spin signal originate from the anisotropic spin relaxation in the nonmagnetic Cu channel. In the last section of the chapter, theoretical explanation for the anisotropic spin relaxation is discussed. The spin-orbital effects on the surfaces of mesoscopic Cu channel induce anisotropic spin relaxation. Chapter 5 points to unanswered questions, and discusses future directions. Finally, chapter 6 summarizes the work.

REFERENCES

[1] G. E. Moore and L. Fellow, Proc. IEEE **86**, 82 (1998).

[2] M. N. Baibich, J. M. Broto, A. Fert, F. N. Van Dau, F. Petroff, P. Eitenne, G. Creuzet, A. Friederich, and J. Chazelas, Phys. Rev. Lett. **61**, 2472 (1988).

[3] G. Binasch, P. Grünberg, F. Saurenbach, and W. Zinn, Phys. Rev. B **39**, 4828 (1989).

[4] J. S. Moodera, L. R. Kinder, T. M. Wong, and R. Meservey, Phys. Rev. Lett. **74**, 3273 (1995).

[5] T. Miyazaki and N. Tezuka, J. Magn. Magn. Mater. **139**, 231 (1995).

[6] J. C. Slonczewski, J. Magn. Magn. Mater. **159**, 1 (1996).

[7] L. Berger, Phys. Rev. B **54**, 9353 (1996).

[8] M. Tsoi, A. G. M. Jansen, J. Bass, W. Chiang, M. Seck, V. Tsoi, and P. Wyder, Phys. Rev. Lett. **80**, 4281 (1998).

[9] J. A. Katine, F. J. Albert, R. A. Buhrman, E. B. Myers, and D. C. Ralph, Phys. Rev. Lett. **84**, 3149 (2000).

[10] S. Datta and B. Das, Appl. Phys. Lett. **56**, 665 (1990).

[11] H. C. Koo, J. H. Kwon, J. Eom, J. Chang, S. H. Han, and M. Johnson, Science **325**, 1515 (2009).

[12] W. Y. Choi, H.-J. Kim, J. Chang, S. H. Han, H. C. Koo, and M. Johnson, Nat. Nanotechnol. **10**, 666 (2015).

[13] A. Manchon, H. C. Koo, J. Nitta, S. M. Frolov, and R. A. Duine, Nat. Mater. **14**, 871 (2015).

[14] N. S. Averkiev and L. E. Golub, **60**, 15582 (1999).

[15] J. Schliemann, J. C. Egues, and D. Loss, Phys. Rev. Lett. **90**, 146801 (2003).

[16] B. A. Bernevig, J. Orenstein, and S. Zhang, Phys. Rev. Lett. **97**, 236601 (2006).

[17] Y. A. Bychkov and E. I. Rashba, JETP Lett. **39**, 66 (1984).

[18] K. Fujiwara, Y. Fukuma, J. Matsuno, H. Idzuchi, Y. Niimi, Y. Otani, and H. Takagi, Nat. Commun. **4**, 1 (2013).

Chapter 2

BACKROUND OF NONLOCAL SPIN VALVES AND SPIN RELAXATION MECHANISMS

2.1 Introduction to Spintronics

Electrons have three fundamental properties: charge, mass, and spin. Conventional electronics utilizes only the charge degree of freedom of electrons and ignores the spin degree of freedom. The technology of spintronics, however, utilizes this spin degree of freedom, which plays a key role in transforming, processing and storing information.

The goal of the spintronics is to achieve new functionality and better energy efficiency in electronic devices using electron spins as information carrier. Spin injection, transport, and relaxation in electronic materials are among the fundamental issues in the research of spintronics.

2.1.1 Giant Magnetoresistance (GMR)

Resistance is caused by collisions between charge carriers and phonons, impurities, and defects in the lattice. In a perfect lattice there will be no collision of electrons. However, the impurities and defects in the lattice act as scattering centers for electrons. In addition, thermal vibration (phonons) of atoms at a temperature above absolute zero increase the collision of electrons and causes an increase of the resistance of the crystal. The magnetic forces on the moving charges also increase the number of collisions between the electrons. Hence resistance of a material changes

with an applied magnetic field. This dependence of the resistance with magnetic field is known as Ordinary Magnetoresistance (OMR). OMR is found in all metals and is proportional to the intensity of the magnetic field so resistance increases while increasing the magnetic field. The magnitude of the OMR effect is usually very small and typically in the order of 1% for the field of 1 Tesla.

The earliest measurement of spin dependent transport was the demonstration of anisotropic magnetoresistance (AMR), [1] in which the resistance of the ferromagnetic material depends on the relative orientation between the charge current and the direction of the magnetization [2]. In ferromagnetic materials this effect originates from the spin-orbit interactions leading to spin dependent scattering of electrons. Typically, the electrical resistance is larger when the magnetic field is oriented parallel to the direction of the electric current than when magnetic field is perpendicular to current [3]. However, the size of the effect (the percentage change in resistance between the parallel and perpendicular magnetic alignments) is small, generally at most in the order of 5% [4].

Therefore it has attracted a great deal of attention in 1988 when a much larger magnetoresistance was discovered in Fe and Cr alternating multilayers [5]. The discovery of this enormous magnetoresistive effect, now known as giant magnetoresistance (GMR), opened the door to a new field of research: spintronics. Nobel Prize was awarded to Albert Fert and Peter Grunberg for the independent discoveries of GMR. In their experiments, while the group of Peter Grunberg [6] used Fe/Cr/Fe trilayer systems, group of Albert Fert [5] used Fe/Cr/Fe multilayers.

A GMR device is a multilayer structure in which ferromagnetic layers is separated by thin non-magnetic (NM) metallic spacers. A basic structure of a GMR

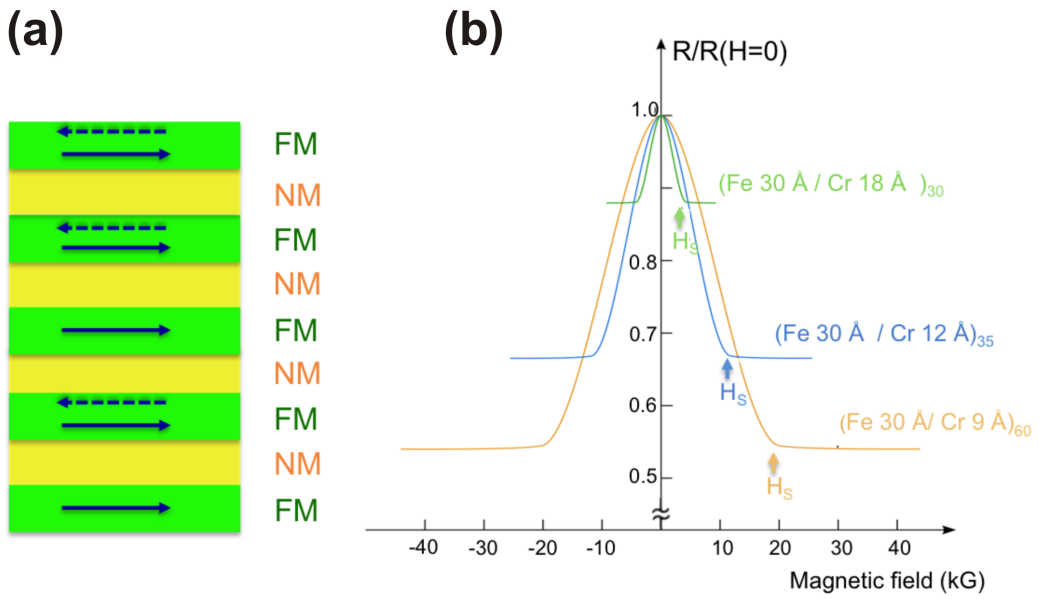

Figure 2.1: a) Schematic diagram of a magnetic multilayer GMR b) Giant magnetoresistance effect as reported by Baibich et al. Resistivity change as a function of applied magnetic field. (b) is reprinted with permission from [5]. Copyright 1988 by the American Physical Society.

device is shown in **Figure 2.1(a)**. GMR effect is a result of spin dependent scattering of spin polarized conduction electrons through these multilayer structures. GMR effects are produced when the external field changes the spin dependent scattering rate. **Figure 2.1(b)** shows experimental results of resistance change with the application of external magnetic field for different Fe/Cr multilayers [5]. The thickness of the nonmagnetic layer is significant to GMR effect, and must be smaller than the mean free path of the electrons, only a few atomic layers thickness, so that the electrons feel the relative orientations of the ferromagnetic layers. In the absence of the external field, the magnetizations of the adjacent FM layers are either oriented ferromagnetically parallel or antiferromagnetically antiparallel as a function of the distance between the ferromagnetic layers by indirect exchange coupling of spins in

FM layers by conduction electrons in the NM metallic spacer, known as the Ruderman-Kittel-Kasuya-Yosida (RKKY) interaction [7,8]. But amplitude of the coupling strength decreases exponentially with the thickness of the NM layer [9]. Hence, it is important to choose optimum thickness of nonmagnetic layer to create antiferromagnetic coupling between the neighboring FM layers and then realign the magnetic moments by an external magnetic field, which is necessary to observe GMR.

2.1.2 Spin Valve

Interlayer exchange coupling is very strong in GMR structures and that coupling is disadvantageous since a very large magnetic field is required to achieve the parallel alignments of the magnetic layers. Fortunately, it is later seen that such coupling is not needed to reach AP states in the spin valve GMR structures.

The spin valves, displayed in **Figure 2.2**, are the most basic structures where the GMR effect can be observed. This device consists a trilayer GMR structure in which a thin nonmagnetic metal is sandwiched between two ferromagnetic metals. In these devices antiparallel alignment of FM layers is obtained in the absence of antiferromagnetic interlayer exchange coupling, by introducing two ferromagnetic electrodes which have different coercive fields [10,11] The thickness of the NM layer is large enough that ferromagnetic layers are not coupled via RKKY interaction and so their magnetizations are independent. Since the soft ferromagnetic material has smaller coercive field than the hard one, the magnetization of that FM layer switches direction at a reversal field that is smaller than that of the hard ferromagnetic layer. Thus, owing to the different coercive forces, parallel and anti-parallel alignment of FM layers can be achieved at different magnetic fields by sweeping the magnetic field as seen in **Figure 2.2(c)**.

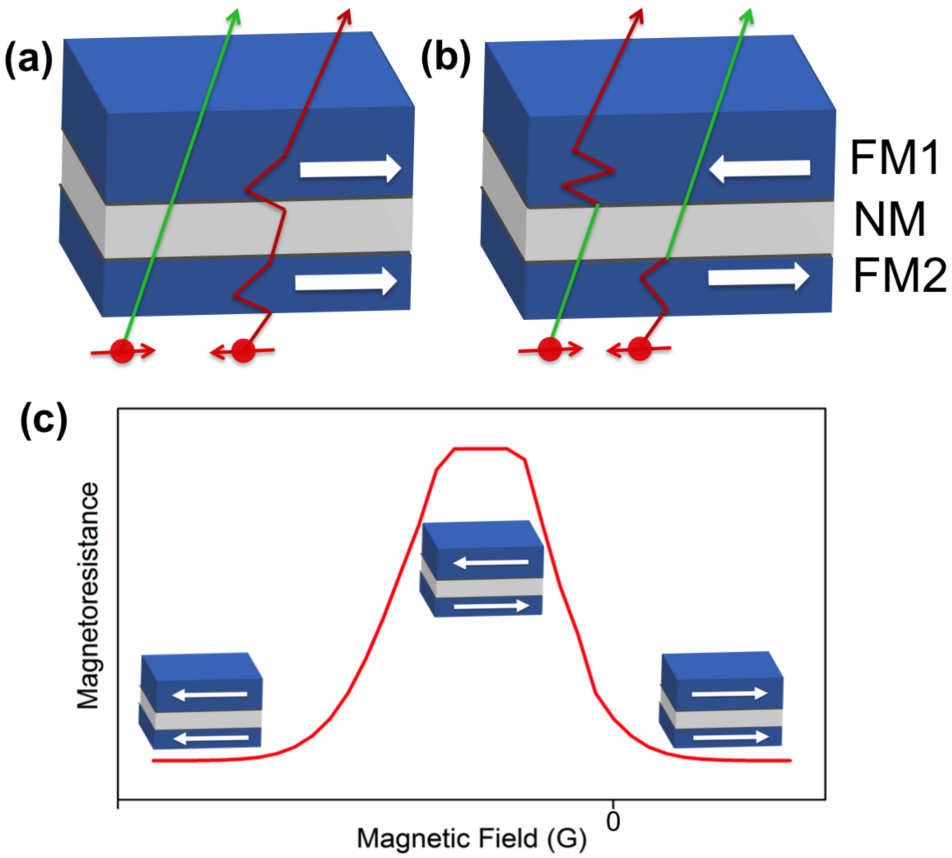

Figure 2.2: A schematic representation of electron transport in a spin valve based on the GMR effect: (a) In the parallel magnetic configuration only one spin type of electrons strongly scatter, which leads to lower resistance; (b) In the anti-parallel magnetic configuration both spin type of electrons strongly scatter which leads to higher resistance; (c) a typical magnetoresistance curve for spin valves.

When a strong enough external magnetic field is applied in the system, the magnetization of the ferromagnetic layers is aligned parallel. Then if an electric current is applied through the system, in which the electric current consists two types of electrons: one type with spin orientation parallel to the magnetization direction of the ferromagnetic layers and the other with spin orientation antiparallel. Electrons with

spins antiparallel to the magnetizations of the ferromagnetic layers will be more strongly scattered than electrons with spins parallel to the magnetizations **[Fig 2.2(a)]**. Hence, the latter serves as the primary conduction channel and gives lower resistance for parallel-magnetized ferromagnetic layers. On the other hand, when the applied magnetic field is reversed, one of the ferromagnetic layers switches direction before the other one and the FM electrodes reaches antiparallel state at some range of applied magnetic field. In this antiparallel state, when the electric current is applied, one type of spins will be scattered strongly in one of the ferromagnetic layers and the other type of spins will be scattered strongly in the other oppositely magnetized ferromagnetic layer as seen in **Figure 2.2(b)**. In this case both types of spins of the electrons experience strong scattering process and this gives higher resistance for the antiparallel state than that for the parallel state. As a result, the lower resistance is observed when the magnetic moments of the FM layers aligned parallel and higher resistance is observed when they aligned antiparallel.

The Percentage difference in resistance between the parallel and antiparallel orientations of ferromagnetic layers

$$\frac{\Delta R}{R_P} = \frac{R_{AP} - R_P}{R_P} \tag{4.1}$$

is defined as the giant magnetoresistance, where R_{AP} and R_P corresponds to the resistances of antiparallel and parallel alignment of ferromagnetic layers, respectively.

Antiparallel alignment of FM layers can also be obtained by using an antiferromagnetic pinning layer. One of the two ferromagnetic layers in a trilayer GMR structure can be attached to an anti-ferromagnetic layer so that the magnetization of this FM layer is pinned in a certain direction by exchange coupling

to the antiferromagnetic pinning layer. Therefore, the magnetization of the pinned FM layer is not sensitive to any reversal fields of moderate size [12]. The magnetization of the other unpinned FM layer is sensitive to the magnetic field and can be easily switched with a relatively small-applied reversal field. Thus, the magnetizations in the two FM layers are switched between an anti-parallel orientation and a parallel orientation by applying a small magnetic field. In these spin valve devices antiparallel alignment of FM layers is not due to the interlayer exchange coupling but because of the exchange coupling of one of the magnetic layer to the pinning antiferromagnetic layer.

Since the easy manipulation of spin structure in the magnetic layers has several advantages for the fundamental research, non-coupled spin valve GMR structures is used in the most applications of GMR, for instance GMR based read-heads of hard-disk drives in 1997 [13,14], magnetic field sensors, non-volatile electronics such as MRAM [10,15–18] etc.

There are two kind of geometries for measuring the GMR, based on the direction of the current flow in the layers. The first one is current-in-plane (CIP-geometry) **[Fig. 2.3(a)]**, where the current flows parallel to FM/NM interfaces, and the second one is current-perpendicular-plane (CPP-geometry) **[Fig. 2.3(b)]**, where the current flows perpendicular to FM/NM interfaces. While the CIP geometry is harder to analyze theoretically, the CPP-geometry is more difficult to achieve experimentally since the resistance of that geometry is too small to be detected unless lateral confinement by lithography is implemented.

During the early years of the discovery of GMR, the experiments were performed in the geometries where the current flows in plane of the devices, but later,

CPP-geometry was more attractive by scientists since it produces larger magnetoresistive effect than CIP geometry [19].

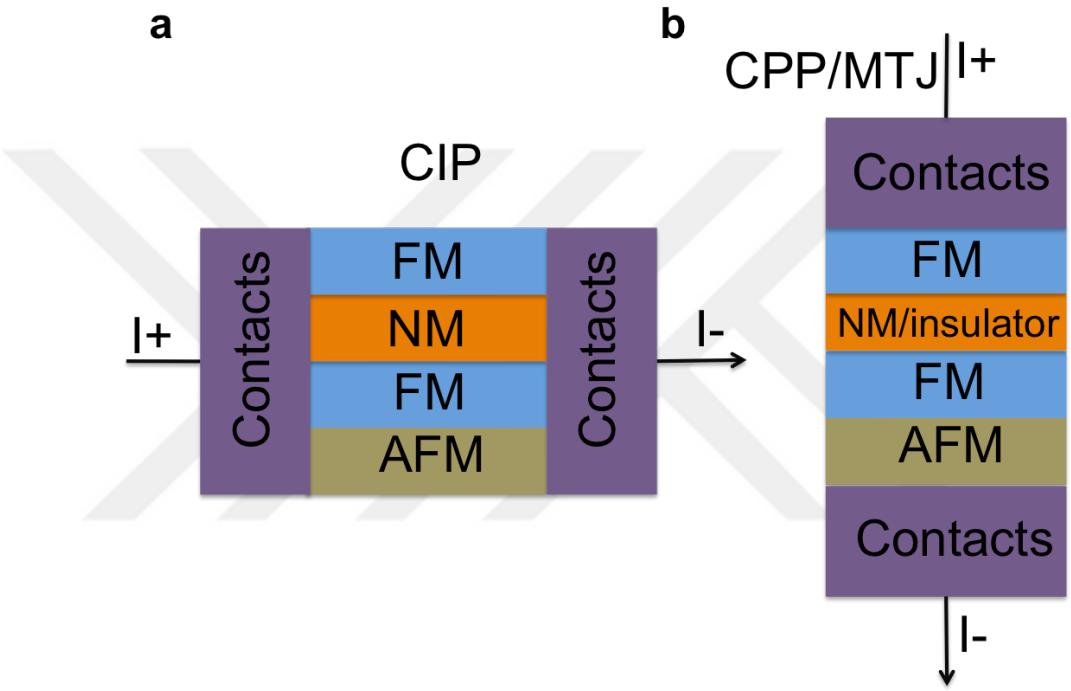

Figure 2.3: Schematic diagrams of (a) CIP (current in plane) and (b) CPP (current perpendicular to plane) GMR spin valves (with NM spacer). MTJ's are similar to CPP configurations, but in these devices a thin layer of an insulator replaces the NM material in spacer layer.

In the CIP geometry, the layers must be thinner than the mean free path of the electrons to provide the flow of electrons between adjacent ferromagnetic layers [20]. However, in the CPP geometry the thickness of the spacer must be smaller than the spin diffusion length in order to conserve the spin information across the NM layer.

The spin diffusion length is typically longer than the mean free path. In CPP-geometry, a spin accumulation build up at the FM/NM interface and this effect induces a spin polarized current diffusing through the NM channel at a large distance from the interface. The spin diffusion length of a material is defined as the mean free path of the electrons between the spin-flipping collisions, and the long spin diffusion length is strongly desired in the research of spintronics.

2.1.3 Tunneling Magnetoresistance (TMR)

Large magnetoresistance that is even greater than GMR was found in magnetic tunnel junctions (MTJs). In these MTJ devices, a thin (a few nanometers) insulating layer is sandwiched between two magnetic layers as shown in **Figure 2.3(b),** and serves as a tunneling barrier for spin-polarized electrons.

First study of MTJs are done by Julliere [21] in 1975 but they observed small TMR effect, around 14% at 4.2 K, but since it was small and not reproducible it is not attracted by scientists until 1995 when a large TMR is discovered, as much as 30% at 4.2 K and 18% at 300 K by Miyazaki et al. [22], and Moodera et al. [11]. Magnetoresistance effect from MTJ devices is significantly larger than GMR devices and recently up to 604% resistance change at room temperature is observed [23]. MTJs are attracted increasing interest because of its potential application in spintronic devices such as more sensitive magnetic filed sensors, magnetic read head of hard disk drives and magnetic random access memories (MRAM) [24,25].

Similar to GMR devices, the resistance of MTJ devices changes depending on the magnetic configurations of the FM layers. While the parallel states give lower resistance, the anti-parallel states give higher resistance. But the physics of TMR is different from that of GMR and is related to the unequal tunneling probabilities of

spin-up and spin-down electrons through a tunneling barrier between two ferromagnets. **Figure 2.4** shows an illustration of spin dependent tunneling. Unlike nonmagnetic materials, in a magnetized ferromagnet, density of states are different for spin-up and spin-down electrons. Conductance in ferromagnetic materials occurs in two independent spin-up and spin-down channels [26,27]. When the FM electrodes are magnetized parallel, majority spin electrons in the first FM material tunnel into the unfilled states of the same majority spin electrons in the second FM material, and minority spin electrons tunnel into the same minority spin states. So in this case,

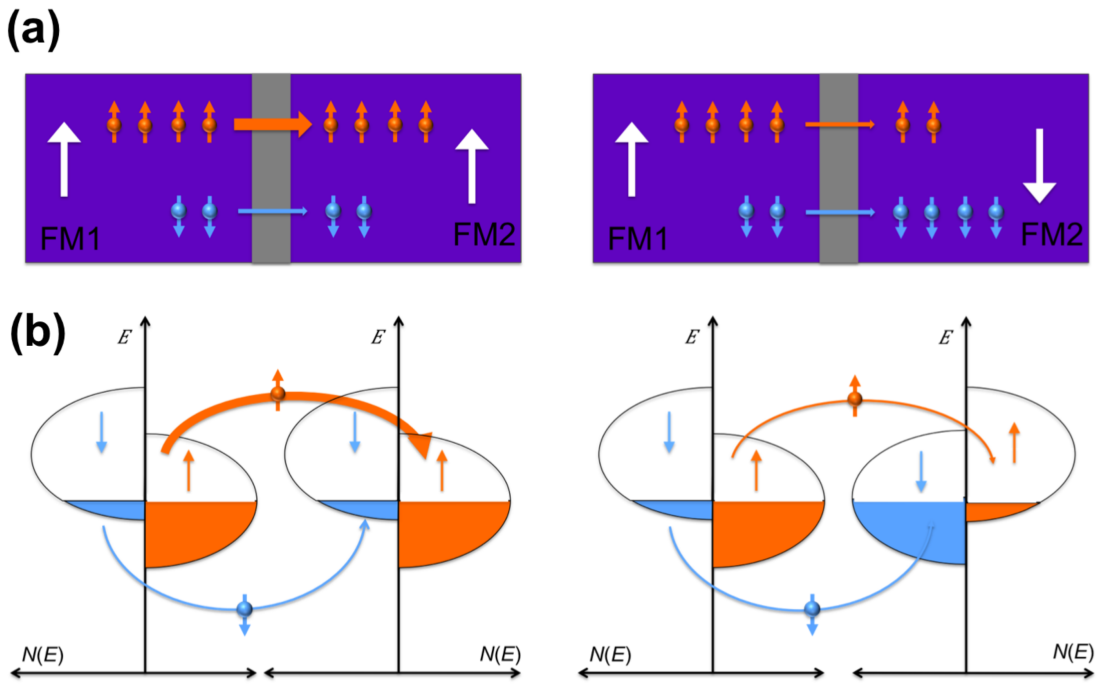

Figure 2.4: Schematic representation of TMR effect in MTJs: (a) MTJ structure is shown for parallel (left) and antiparallel (right) alignments of the ferromagnetic layers. (b) Density of states schematic for spins of electrons tunneling process in P (left) and AP (right) configurations of MTJs. The density of states of both FM layers determines how large the electrons tunnel through insulator layer.

for one of the spin channel the conductance is dominant and gives lower resistance. However, for antiparallel magnetization of FM electrodes, majority spin electrons in the first FM material tunnel into the minority spin states in the second FM material and vice versa. This results in lower conductivity for both spin channels and gives higher resistance in antiparallel configuration. TMR ratio is defined as the resistance difference between parallel and antiparallel alignments, normalized by the parallel resistance and based on the Julliere's model [28], the TMR can be written as follows:

$$TMR = \frac{(R_{AP} - R_P)}{R_P} = \frac{2P_L P_R}{1 - P_L P_R} \tag{2.2}$$

where R_{AP} and R_P corresponds to the resistances of antiparallel and parallel alignment of ferromagnetic layers, and P_L and P_R are the spin polarizations of the left and right ferromagnetic electrodes and is defined by

$$P_{L(R)} = \frac{N^{\uparrow}_{L(R)}(E_F) - N^{\downarrow}_{L(R)}(E_F)}{N^{\uparrow}_{L(R)}(E_F) + N^{\downarrow}_{L(R)}(E_F)} \tag{2.3}$$

where $N^{\uparrow}_{L(R)}(E_F)$ and $N^{\downarrow}_{L(R)}(E_F)$ is the density of states for spin-up and spin-down electrons at the Fermi energy E_F of the left and right ferromagnetic electrodes, respectively. The Julliere's equation shows that higher spin polarization gives higher TMR ratio, so the materials with higher spin polarization is attractive for spintronics-based applications.

2.2 Introduction to Nonlocal Spin Valve

Spintronic devices such as GMR spin valves and MTJ devices were built in vertical structures and have only two terminals. In these vertical spin valve devices, spin polarized charge currents flow through nonmagnetic channels and transport at small distances, in the range of nonmagnetic materials' thicknesses. At short transport

distances spin manipulation is limited, because it is difficult to have additional control terminals such as a gate electrode. Alternatively, it is intriguing to fabricate the lateral structures with multi-terminal devices like nonlocal spin valve (NLSV) devices.

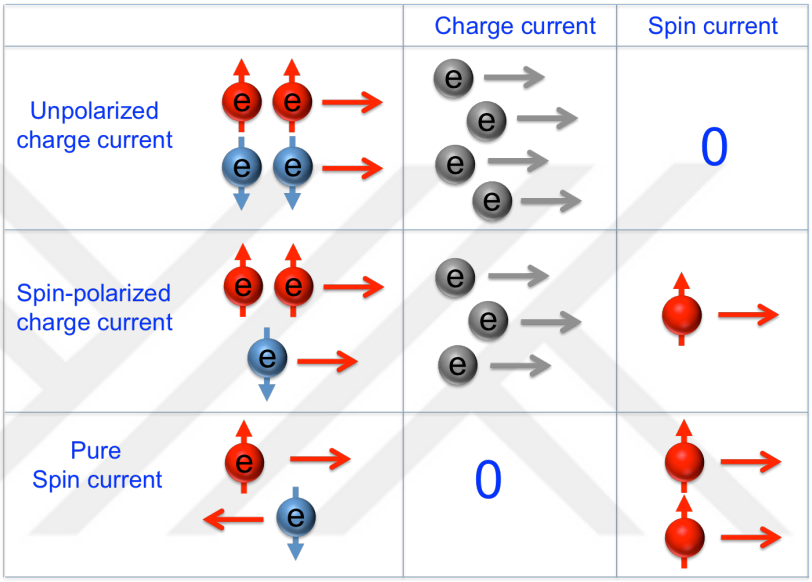

Figure 2.5: Illustration of the difference between unpolarized charge current, spin-polarized charge current and pure spin current.

NLSVs are lateral multi-terminal devices in which pure spin current can easily be generated and transport at longer distances. Therefore, there is more degrees of freedom for the manipulation of electron spins in non-local spin valves, and these devices are attractive to investigate spin transport in metals, semiconductors, and graphene.

2.2.1 Generation of Pure Spin Current

In the field of spintronics, spin current, the flow of spin angular momentum, provides crucial functionalty. The injection and transport of spin current through nonmagnetic metals are of fundamental research of interest. Conventional electronics is based on unpolarized charge current with no associated spin transport. However, the field of spintronics takes advantage of spin degree of freedom of electrons to create new generation of spin based electronic devices with extended functionalities.

A current that consist of unequal number of spin-up and spin-down electrons flowing in the same directions are known as spin polarized charge current where spin current is accompanied with charge current. However, pure spin current is flow of same number of electrons with different spins in opposite directions, Therefore, there will be no net charge current flow in a pure spin current ($J_e = J_\uparrow + J_\downarrow = 0$); however, there will be only spin current ($J_e \neq J_\uparrow + J_\downarrow = 0$). **Figure 2.5** shows a schematic illustration of charge current, spin polarized charge current and pure spin current with electron movement. The other approach to consider pure spin current would be spin diffusion in a material. If there is accumulation of non-equilibrium spins in a nonmagnetic metal, the accumulated spins diffuses away from injection point and give rise to a pure spin current at a given location.

There are several methods to generate pure spin currents like spin pumping [29] which requires microwave technology, spin Seeback effect [30,31] which requires temperature gradient, and spin Hall effect [32] which results from charge current. In this thesis, we used the method of electrical generation of a pure spin current in non-local spin valve devices. A non-local spin valve is a mesoscopic lateral structure consisting of two FM electrodes bridged by one non-magnetic channel where two FM electrodes work as an injector and detector. A pure spin current can be

generated in the non-magnetic channel by injecting a charge current from one of the FM spin injector into the non-magnetic channel, and then non-local voltage can be measured between the other FM electrode and the other end of the nonmagnetic channel. Due to separation of injection and detection circuit, the spin current is decoupled from the charge current enabling the generation of pure spin current.

2.2.2 Nonlocal Spin Valve Measurements

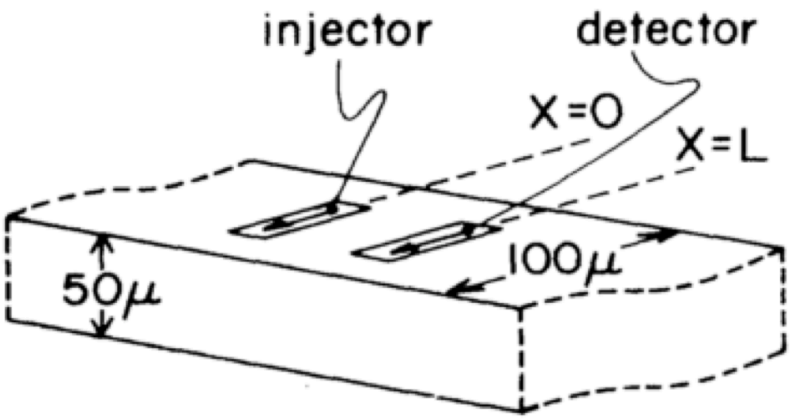

Figure 2.6: The geometry of the spin injection experiment on a single crystal aluminum bar. Reprinted with permission from [33]. Copyright 1985 by the American Physical Society.

The first experiment of electrical spin injection in non-local structures was done in 1985 by Johnson and Silsbee [33]. The geometry is illustrated in **Figure 2.6**. This device consists of two parallel 15 μm wide permalloy ($Ni_{80}Fe_{20}$ alloy) contacts is patterned on the top surface of a 50 μm thick, 100 μm wide and 1.5 cm long bulk aluminum (Al) metal. In this experiment, a pure spin current is injected from

permalloy injector into an aluminum (Al) single crystal and diffuses away from the injection point. Later in 2001, Jedema and coworkers performed spin injection experiments in the mesoscopic non-local lateral spin valve structures [34]. To

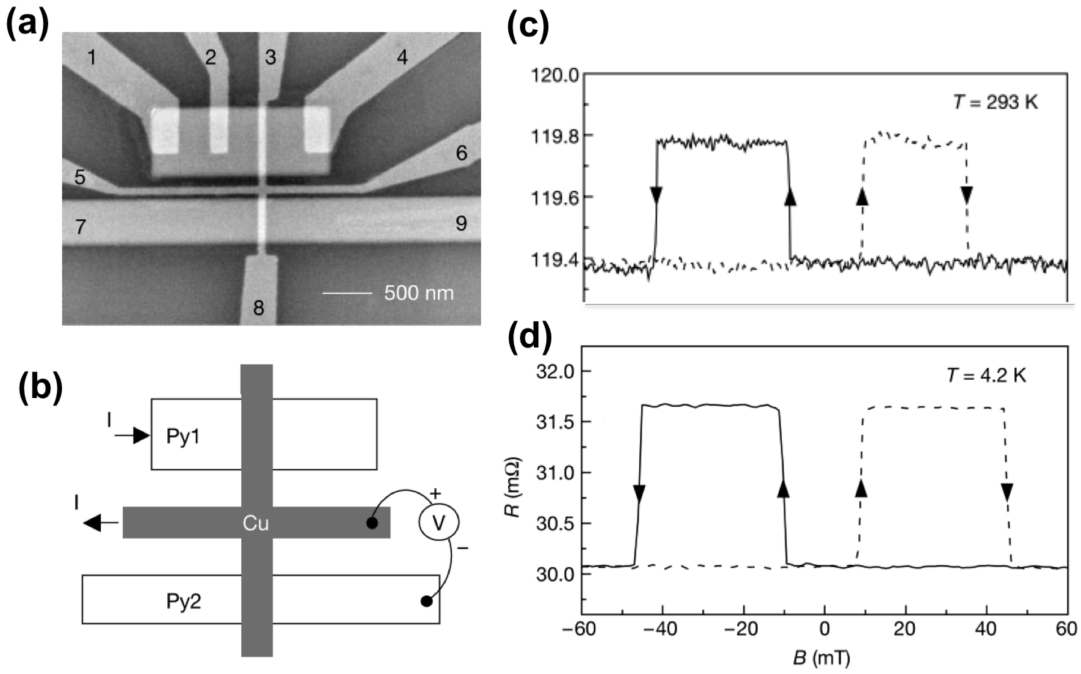

Figure 2.7: Non-local magnetoresistance measurement. (a) Scanning electron microscope image of a spin valve. (b) Schematic representation of the non-local spin valve structure. (c),(d) The measurement of the non-local spin signal at 293 K and 4,2 K respectively. Reprinted with permission from [34]. Copyright 2001 Macmillan Magazines Limited.

fabricate this structure, two permalloy electrodes with variable separations are first deposited under a crossed nonmagnetic Cu strips. They observed clear spin signals at T = 4.2K and even at room temperature with non-local measurements **[Fig. 2.7]**.

Subsequently in 2002, the same group fabricated Co/Al NLSV devices with an inserted oxide barrier between the FM and NM channels [35]. They first evaporated Al strip on the substrate, and the surface of the Al strip is oxidized in oxygen

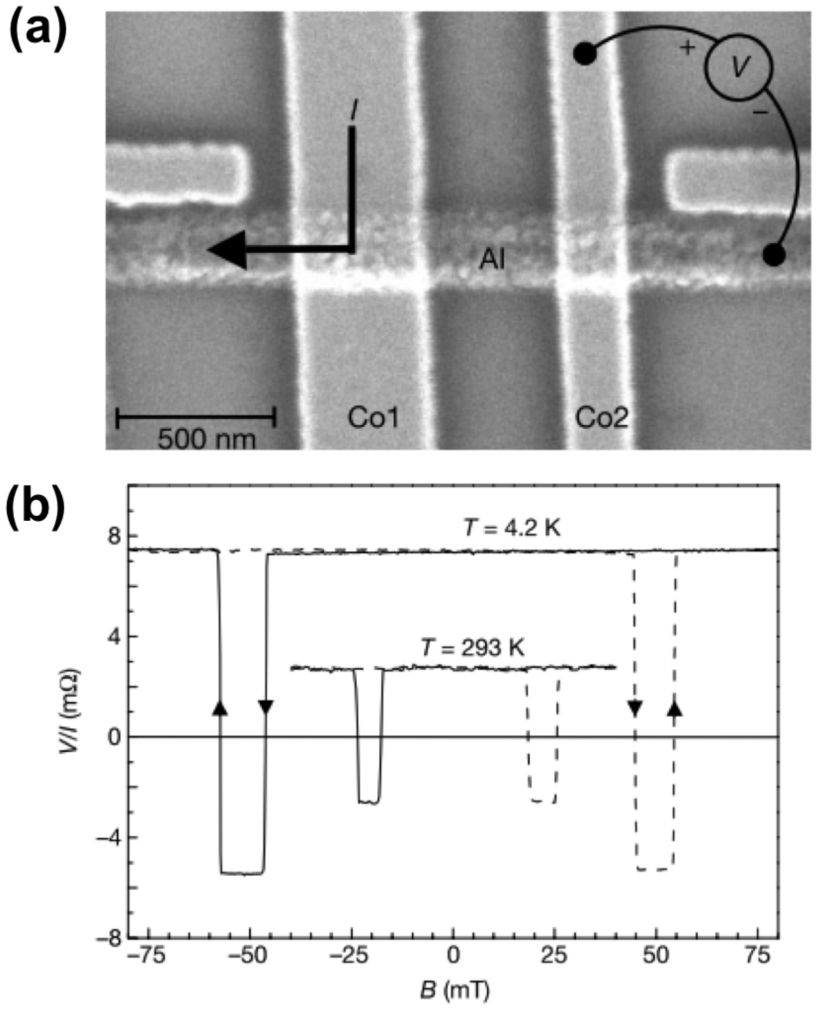

Figure 2.8: Non-local spin signal measurement: (a) SEM image of the sample. Aluminum wire is designed perpendicular to the two parallel cobalt wires. (b) Non-local resistance versus magnetic field curve at 4.2 K and 293 K. Reprinted with permission from [35]. Copyright 2002 Macmillan Magazines Limited.

environment (O_2) to develop Al_2O_3 barrier on the top of the Al channel. In the next step, two ferromagnetic Cobalt (Co) electrodes are evaporated; forming two $Co/Al_2O_3/Al$ oxide tunnel junctions for spin injection and spin detection, as shown in **Figure 2.8**. Spin polarized current is driven from the injector Co electrode into the Al strip, and then a large spin signal is observed at T = 4.2K. It is shown that spin injection and detection efficiency is greatly increased in tunnel-junction based NLSV devices, resulting in enhanced non-local spin signals. These non-local spin injection and detection experiments were followed by many groups using different materials and geometries [36–42].

2.2.3 Principles of Nonlocal Spin Valves

The principles of a non-local spin valve device are illustrated in **Figure 2.9**. A typical NLSV device consists of a nonmagnetic channel N connected to a parallel pair of ferromagnetic injector and detector electrodes, as shown in **Figures 2.9(a)** and **(b)**. These two FM electrodes are fabricated by different geometric dimensions, so that they will have different switching fields. When there is no current in the system, Fermi level for spin up and spin down electrons in the NM channel should be equal since spin polarization of a nonmagnetic material is zero. **Figure 2.9(c)** shows schematic representation of the band structures for the FM injector F_1, NM channel N, and FM detector F_2 in the NLSV geometry. During the measurement, while an external magnetic field is swept in the direction parallel to the FM electrodes, charge current I is sent from F_1 injector into the left side of the NM channel N. In this case, since the spin population around the Fermi level in the F_1 electrode should be unequal, it will derive a spin-polarized current go through the interface and into the N channel. This would lead to non-equilibrium spin accumulation, ΔM, in the vicinity of the FM/NM

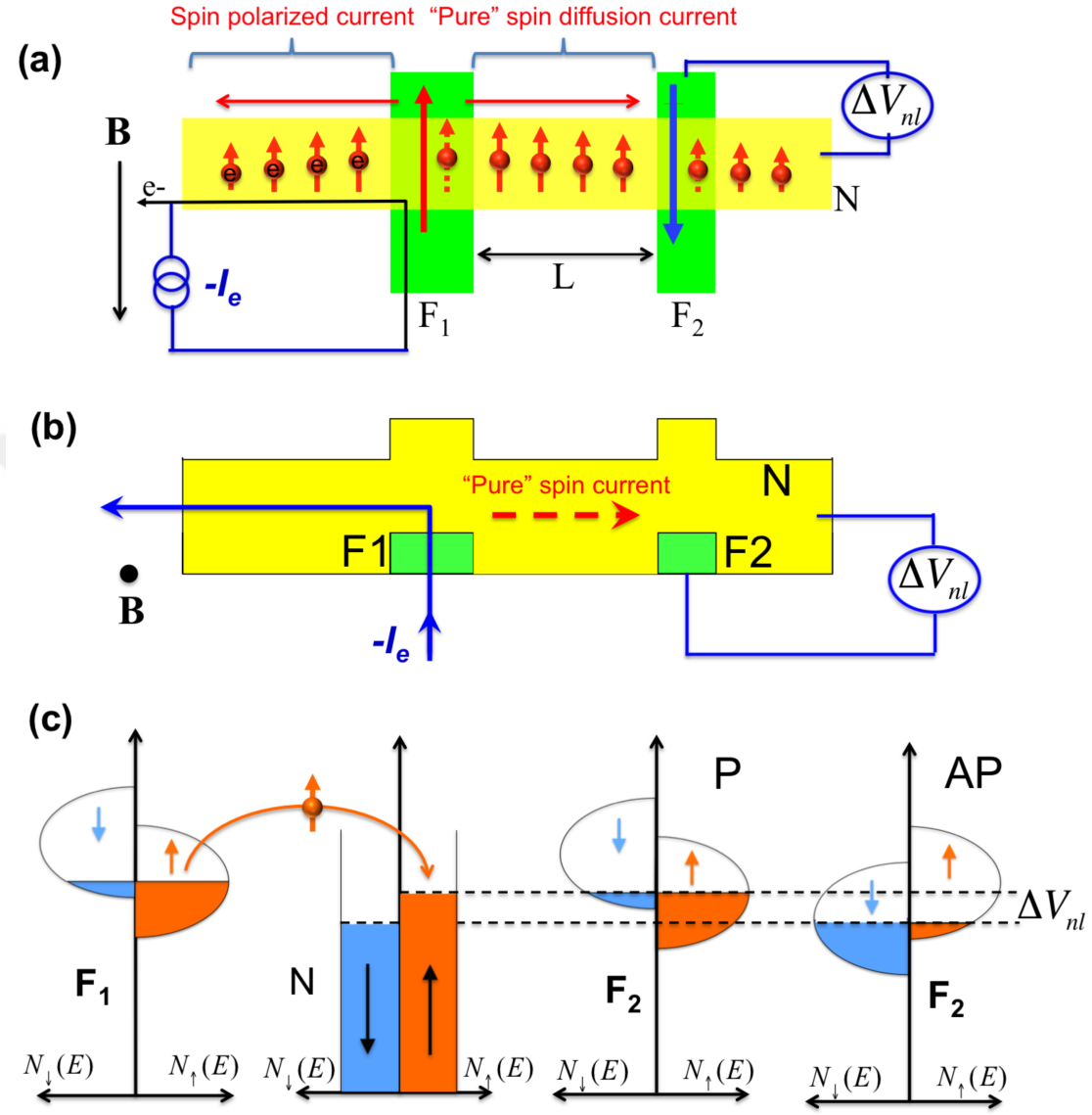

Figure 2.9: Concept of the non-local spin valve. (a) Top view. (b) Side view. A schematic diagram of a non-local spin valve device. The charge current is injected from F_1 through the left end of the NM channel. The nonlocal voltage is detected between F_2 and the right end of the NM channel. (c) Schematic representation of densities of states for spin-up and spin down bands in F_1, N and F_2 in the NLSV geometry. Nonlocal spin resistance ΔR_s is determined by dividing the nonlocal voltage ΔV_{nl} by the injected current I_e.

junctions and decays exponentially with the distance from the spin injection point within the characteristic spin diffusion length λ of the NM channel. This spin accumulation could be detected by the F_2 electrode by measuring the voltage between the F_2 and the right side of the N channel. The spin accumulation give rise to an electrochemical potential difference and results in a splitting of the Fermi energy levels for spin-up and spin-down electrons in the NM channel as shown in **Figure 2.9(c)**. In the non-local geometry, electric current is flowing in one direction, to the left side of the FM injector; by contrast, injected spin current diffuses away in both directions according to the spin dependent diffusion equation [43],

$$\frac{\partial^2(\mu_\uparrow - \mu_\downarrow)}{\partial x^2} = \frac{(\mu_\uparrow - \mu_\downarrow)}{\lambda_s^2} \tag{2.4}$$

This leads to a pure spin current diffusing to the right side of F_1 injector. Due to the separation of injection and detection circuit in the non-local measurement technique, there is no charge background in detection circuit, which eliminates spurious effects, such as anisotropic magnetoresistance (AMR) and makes it very sensitive method of detecting spin accumulation. With the help of non-local measurement technique, pure spin current can be generated and transported over a distance of micrometers and still remains detectable.

The spin accumulation in the NM channel produces spin-dependent electrochemical potentials, which can be detected by using F_2 electrode. Depending on the magnetization of F_2, Fermi level in F_2 aligns with the spin-up or spin-down Fermi level of NM material. If the magnetization of F_2 electrode is parallel with the spin direction of the pure spin current, its Fermi level should be aligned with the higher Fermi level in the NM channel. Otherwise, its Fermi level should be aligned with the

lower Fermi level in the NM channel as shown in **Figure 2.9(c)**. Therefore, as a function of magnetic field parallel to the ferromagnetic electrodes, clear voltage change is observed when the magnetizations of F_1 and F_2 switch between parallel and antiparallel alignments. The magnitude of the voltage change $\Delta V_{nl} = V_P - V_{AP}$ normalized by the injection current I is known as non-local spin signal, $\Delta R_s = \Delta V_{nl}/I$, and it is used to quantify the spin injection and transport characteristics of non-local spin valves.

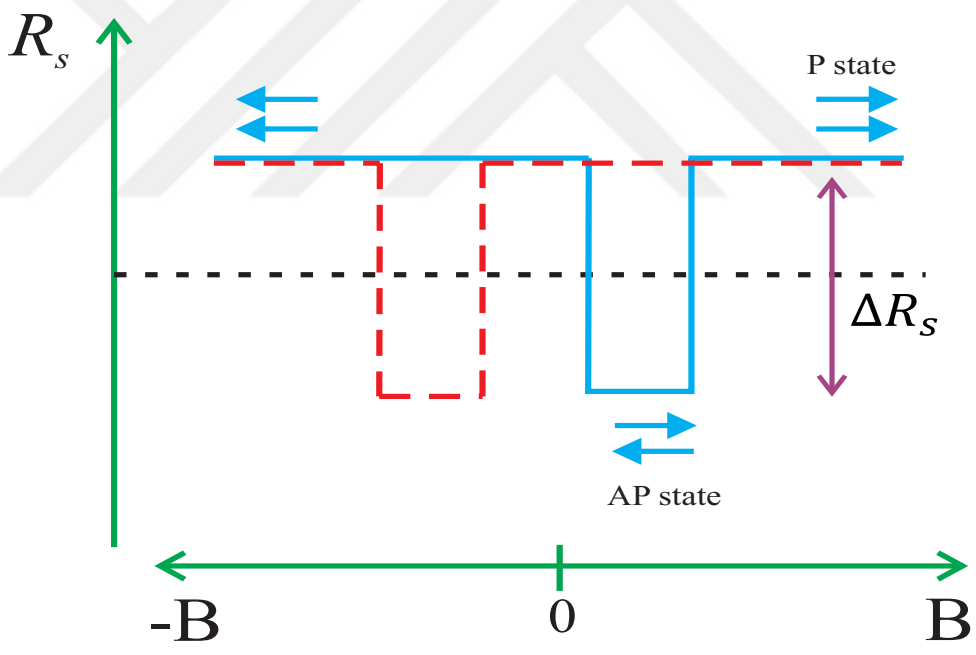

Figure 2.10: Illustration of non-local spin signal within the magnetic field along the FM electrodes. The pairs of green arrows indicate magnetization states of F_1 and F_2. Blue solid line shows the spin resistance as a function of magnetic field, swept from the negative to positive field values. Red line corresponds to the swept magnetic field in the opposite direction.

For the non-local spin signal measurements, a magnetic field B is first applied along the easy axis of FM electrodes to align the magnetizations of the FM contacts. Then the magnetic field is swept toward the opposite direction. Since the geometric dimensions of the FM electrodes are chosen to be different sizes, magnetization of these electrodes reverses independently at different reversal fields. **Figure 2.10** shows the measured spin signal from a non-local spin valve. It can be seen that spin resistance, R_s, value of an NLSV device changes depending on the parallel and anti-parallel alignments of the electrodes. The difference of the spin resistance, R_s, between the parallel and antiparallel states gives spin signal of the NLSVs. The observed non-local spin signal, ΔR_s, can be derived by solving the spin diffusion equation (2.5). When both junctions are tunnel junctions, the spin signal is given by [35,37,44,45]

$$\Delta R_s = \frac{P_1 P_2 \lambda_s \rho}{A} e^{-L/\lambda} \tag{2.5}$$

where P_1 and P_2 are the spin polarizations at the F_1/N and N/F_2 interfaces, respectively, λ_s is the spin diffusion length in the NM channel N, ρ is the resistivity of the N, A is the cross-sectional area of the channel N, and L is the center to center distance between the two electrodes F_1 and F_2.

In the experiments, to determine the average interface spin polarization $\sqrt{P_1 P_2}$ and the spin diffusion length λ_s, a series of samples are fabricated with same structures but varying separation L between injector and detector electrodes. These two parameters, $\sqrt{P_1 P_2}$ and λ_s, are obtained by fitting the spin resistance difference, ΔR_s, versus separation of Ferromagnetic electrodes, L, curve using the equation 2.5 above.

2.3 Spin Relaxation Mechanisms

In non-magnetic materials, the distance the spin current could propagate without losing its polarization is limited by spin relaxation. Hence, the control of spin relaxation has great importance for spintronics and attracts more research attention recently. The spin relaxation happens through various processes and can be described with the spin lifetime τ_s, characteristic time scale for spin relaxation. Once spin polarized electrons injected into a nonmagnetic material, electrons do not conserve their initial spin orientations and spin relaxation causes the electrons to lose their initial spins after the characteristic time scale τ_s, leading to the spin equilibrium in the system. Since the non-equilibrium spin accumulation that is used to carry information encoded in their spin states will equilibrate over time, the spin-relaxation time is crucial for transfer of information in macroscopic distances. The determination of the spin-relaxation time and length is very important for applications in the field of spintronics.

There are mainly four types of mechanisms responsible for the spin relaxation of conduction electrons in nonmagnetic electronic systems: Elliot-Yafet [46] , Dyakonov-Perel' [47], Bir-Aronov-Pikus [48], and hyperfine-interaction processes [49]. The relative strengths of these spin relaxation mechanisms can vary depending on the materials and temperature. Hence, it is very crucial to determine which spin relaxation mechanism is dominant so that the effective spintronic devices can be designed. In the following sections the first two of the spin relaxation mechanisms, Elliot-Yafet and Dyakonov-Perel', two major spin relaxation mechanisms for conduction electrons in metals, will be discussed.

2.3.1 Elliot-Yafet Spin Relaxation Mechanism

The way that the electron spin can be flipped infers that there should be a mechanism, which permits the interaction of electron spins with its environment. The intrinsic spin-orbit coupling is known as the origin of the EY mechanism [46,50]. It is based on the fact that electron states of opposite spins are coupled due to the spin-orbit interaction [18]. The spin-orbit potential is given by

$$V_{SO} = \frac{\hbar}{4m^2c^2}\nabla V \times \hat{p}.\hat{\sigma} \tag{2.6}$$

where V is the scalar spin independent periodic lattice potential, m is the free electron mass, $\hat{p} = -i\hbar\nabla$ is the linear momentum operator, $\hat{\sigma}$ is the Pauli matrices and c is the speed of the light. Hence, Bloch wave functions have no more pure spin states but should be written as linear combinations of the Pauli spin up $|\uparrow\rangle$ and spin down $|\downarrow\rangle$ states. These degenerate Bloch states with the lattice wave vector $\boldsymbol{k}$ can be expressed as [46].

$$\begin{aligned}\psi_{k,n}^{\uparrow} &= [a_{k,n}(r)\left|\uparrow\right\rangle + b_{k,n}(r)\left|\downarrow\right\rangle]e^{ik.r} \\ \psi_{k,n}^{\downarrow} &= [a_{k,n}(r)\left|\downarrow\right\rangle + b_{k,n}(r)\left|\uparrow\right\rangle]e^{ik.r}\end{aligned} \tag{2.7}$$

where r is the radius vector and n is the band index. The two Bloch wave functions are degenerate because of the coexistence of space inversion and time reversal symmetry.

In this mechanism spin-orbit coupling causes the conduction electron spins to flip with a certain probability during momentum scatterings due to impurities, boundaries, interfaces or phonons. Spin relaxation does not occur only due to spin-orbit coupling, but the combination of the spin-orbit coupling with momentum scattering leads to spin relaxation.

When the spin-orbit coupling is weak, the typical values for amplitude $|b|$ is much smaller than $|a|$, $|b| \ll |a|$, and therefore Bloch states have nearly pure spin

states. In this case, since the separation between the bands is much larger than the spin-orbit interaction, first order perturbation theory regarding the spin-orbit coupling as a perturbation gives

$$|b| \approx \frac{\lambda_{SO}}{\Delta E} << 1 \tag{2.8}$$

where λ_{SO} is the amplitude of spin-orbit coupling matrix element between the considered band states and the nearest band state with the same momentum, and ΔE is the difference of average energy between these adjacent band states.

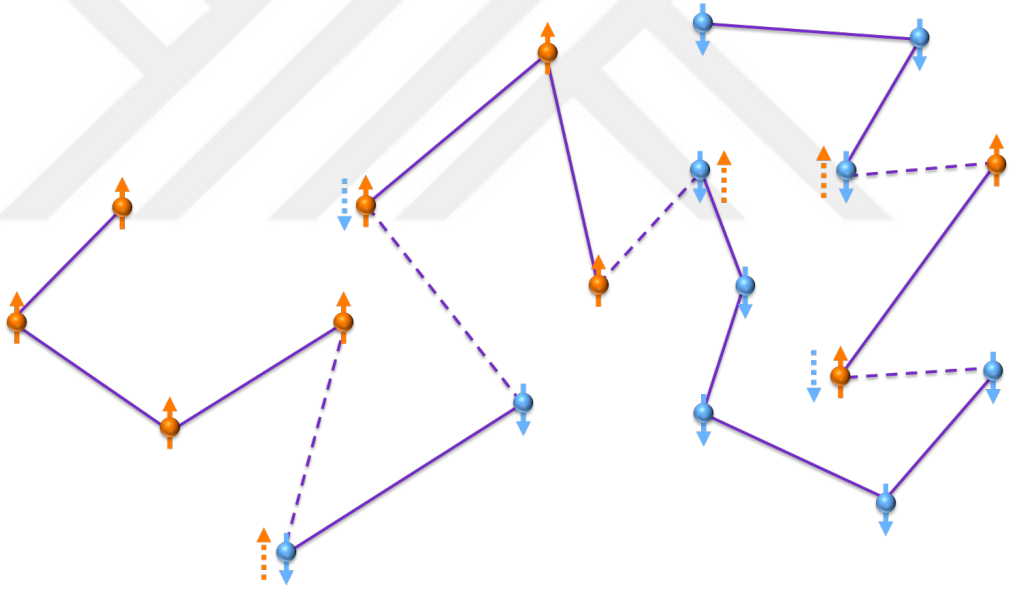

Figure 2.11: Illustration of Elliot-Yafet spin relaxation mechanism. When the spins of electrons scatter through the Elliot-Yafet mechanism, spin-relaxation rate is directly proportional to the momentum scattering rate.

Elliot used first order perturbation theory and showed that spin-flipping probability of an electron spin at an ordinary momentum scattering event is

$$\left\langle b^2 \right\rangle \approx \frac{\lambda_{SO}^2}{\Delta E^2} \tag{2.9}$$

As a result, the spin-relaxation rate due to Elliot-Yafet spin relaxation mechanism is given by

$$\frac{1}{\tau_s} \approx \left\langle b^2 \right\rangle \frac{1}{\tau} \tag{2.10}$$

where τ_s is the spin-relaxation time, τ is the momentum scattering time, and $\langle b^2 \rangle$ is the spin-flip probability. It is observed that spin-relaxation time τ_s is directly proportional to the momentum relaxation time τ when the spin of the electrons relaxes through the Elliot-Yafet mechanism. This property is expected because spin relaxation in the Elliot-Yafet mechanism occurs only during collisions. A schematic illustration of Elliot-Yafet mechanism is depicted in **Figure 2.11.** Jedema et al. [51] researched spin-relaxation times in Al and Cu thin films. In this research, impurity spin-relaxation ratio, τ^{imp}/τ_s^{imp}, and electron-phonon spin-relaxation ratio, τ^{ph}/τ_s^{ph}, are compared using Py/Cu/Py and Py/Al/Py non-local spin valves. Here τ^{imp} and τ^{ph} are momentum relaxation times for scattering of electrons from impurities and phonons, respectively.

G. Mihajlovic et al. [52] studied the probability of spin-flip scatterings of electrons in Ag channel on Py/Ag lateral spin valves. He presented a model based on Elliot-Yafet spin relaxation mechanism in order to separately determine these spin-flip probabilities due to impurities, phonons and surface scatterings.

2.3.2 D'yakonov-Perel' Spin Relaxation Mechanism

The Elliot-Yafet spin relaxation theory is valid for metals with inversion symmetry, D'yakanov-Perel mechanism [47], in contrast, present in the systems without inversion symmetry. In this case, the spins of electrons precess around the

effective magnetic field of spin-orbit coupling, resulting from the lack of inversion symmetry. The interaction between the electron spin and momentum-dependent intrinsic effective magnetic field causes spin dephasing.

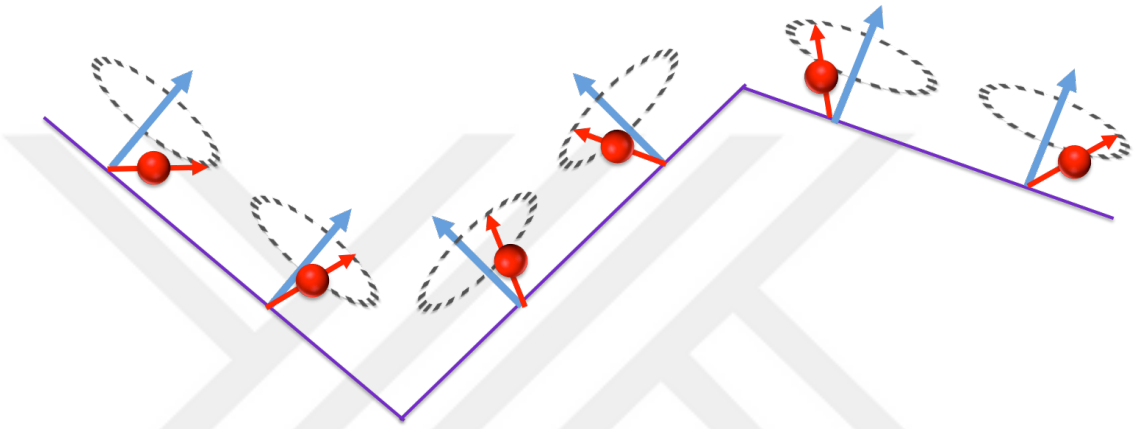

Figure 2.12: Illustration of D'yakanov-Perel spin relaxation mechanism. when the spins of electrons scatter through the D'yakanov-Perel mechanism, spin-relaxation rate is inversely proportional to the momentum scattering rate.

Unlike Elliot-Yafet mechanism where spin relaxation occurs during the momentum scattering events, D'yakanov-Perel mechanism causes dephasing of spins in between the scattering events and leads to the opposite effect; a higher rate of momentum scattering results in a lower rate of spin relaxation. Because, when momentum scattering is frequent, the electrons mostly do not have enough time for their spins to precess sufficiently to flip their spins, therefore spin-relaxation time increase by DP mechanism. A schematic illustration of D'yakanov-Perel mechanism is depicted in **Figure 2.12.**

Spin-relaxation rate from from D'yakanov-Perel mechanism is expressed as [53],

$$\frac{1}{\tau_s} \approx \Omega^2 \tau \tag{2.11}$$

where Ω is precession frequency of electron spins. It is seen that spin-relaxation time τ_s is inversely proportional to momentum relaxation time τ.

As a consequence, it is important to note that stronger momentum scattering increases spin-relaxation rates under Elliot-Yafet mechanism, but decreases spin-relaxation rates under D'yakanov-Perel mechanism.

2.4 Spin-Orbit Coupling

An orbital motion of an electron in the electric field of nucleus generates an effective magnetic field, $\vec{B}_{eff} \sim \vec{E} \times \vec{p}/mc^2$, in electron's frame of motion, the magnetic field depends on the electron's speed and travel direction. Interaction of this generated magnetic field with spin magnetic moment of the electron is known as spin-orbit coupling. Such interaction leads to the splitting of electron energy levels in atoms or molecules. Spin-orbit coupling is described by spin-orbit Hamiltonian:

$$\hat{H}_{SO} = \frac{1}{2m_e c^2} \frac{1}{r} \left(\frac{\partial V}{\partial r} \right) \hat{L} \cdot \hat{S} \tag{2.12}$$

where V is the electric potential of the electron, c is the speed of the light, m_e is the effective electron mass, $\hat{L}$ is the orbital angular momentum and $\hat{S}$ is the spin angular momentum of the electron.

2.4.1 Rashba Spin-Orbit Coupling

In solids, it's believed that electronic energy bands split in the absence of crystal inversion symmetry. There are two origins for the electric fields causing spin-orbit coupling in a crystal. Dresselhaus effect [54] arises from bulk inversion asymmetry in three-dimensional bulk solids, and Rashba effect was first described by Rashba [55] in 1959, and arises from structural inversion asymmetry, where $V(r) \neq V(-r)$, in two-dimensional quantum wells. Rashba spin-orbit coupling Hamiltonian [56] at the surface, lying in the x-y plane is described by

$$H_R = \frac{\alpha_R}{\hbar}\sigma \cdot (\hat{z} \times p) = \frac{\alpha_R}{\hbar}(p_x\sigma_y - p_y\sigma_x)$$
$$H_R = \frac{\alpha_R}{\hbar}\begin{pmatrix} 0 & -ip_x - p_y \\ ip_x - p_y & 0 \end{pmatrix} \tag{2.13}$$

where , α_R is the Rashba spin-orbit coupling strength which can be modulated via external gate voltage [57,58], $\sigma = \sigma_x, \sigma_y, \sigma_z$ is the Pauli spin matrix vector, $\boldsymbol{p}$ is the momentum vector and $\hat{z}$ is the unit vector perpendicular to the surface. This type of spin-orbit interaction was derived by Rashba and Sheka [59] for wurtzite-type crystals, and the by Vasko [60] for two dimensional electron gas.

Figure 2.13 (a) shows a model of two dimensional free electron gas [61], where the spatial inversion symmetry is broken across the surface lying in *x-y* plane. When an electron moves in the x direction with momentum (*p*), a Rashba effective magnetic field (B_{eff}) arises in the direction perpendicular to the direction of the electron's momentum. As a result the effective magnetic field tend to align electron spin with the direction of the field, which is perpendicular to spin momenta in the surface plane.

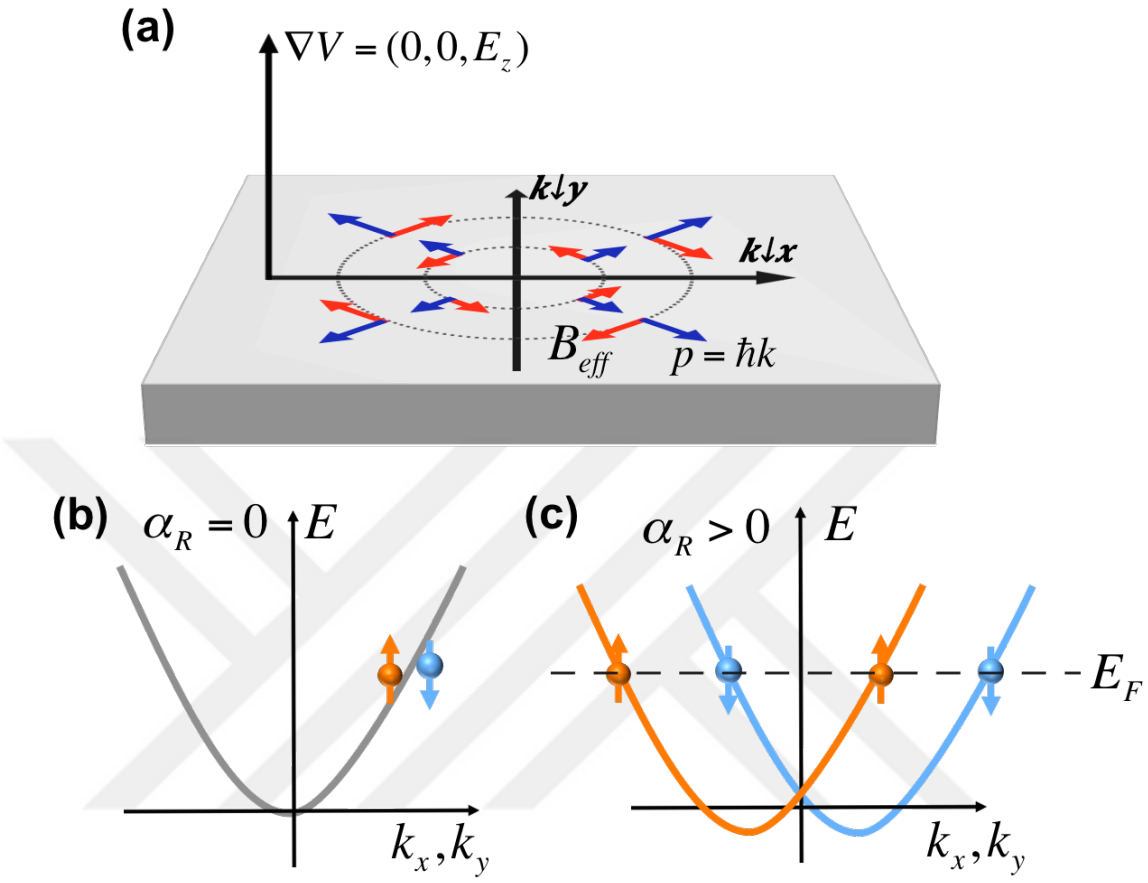

Figure 2.13: Schematic representations of the electronic band structure (a) Sketch of the Rashba spin-orbit effective magnetic fields and momentum directions at the surface. The effective magnetic field tends to align electron spins (red arrows) with the direction of the field, which is perpendicular to the electron's momentum (blue arrows). (b), (c) A schematic representation of the energy dispersion in 2D free electron gas model (b) in the absence of Rashba spin-orbit coupling, electrons with up spin and down spin are degenerate. (c) in the presence of Rashba spin-orbit coupling. Spin degeneracy is lifted because of the spin-orbit coupling the two bands carry opposite spins, shown by the orange and light blue arrows. Circular dots in (a) shows Fermi surface of this two-dimensional free electron gas with Rashba effect.

The energy of a free electron is shifted by $\pm\alpha_R k$ due to Rashba Hamiltonian, which can be expressed as,

$$E(k) = \frac{\hbar^2}{2m}k^2 \pm \alpha_R k \tag{2.14}$$

where α_R is the Rashba parameter. As shown in **Figure 2.13 (b)** in the absence of Rashba spin-orbit interaction spin-up and spin-down states are degenerate. **Figure 2.13 (c)** shows band dispersion of this two dimensional free electron gas model. Spin degeneracy is lifted in the 2D state due to strong spin-orbit coupling resulting from the broken space inversion symmetry. Spin splitting size is given by the Rashba parameter α_R.

Tunability of Rashba coupling by external electric field attracts a great interest by scientists because of promising applications in quantum computing and spintronic devices where the spin currents can be controlled via electrostatic gating. Controlling spin states with electric fields rather than magnetic fields is far more advantageous, because electric fields can be applied at nanometer length scales and power consumption is reduced by using electric fields. A most remarkable new generation of spintronic device, spin field effect transistor (spin-FET), have been proposed by Datta and Das [62] in 1990. The mechanism behind this transistor is Rashba spin-orbit coupling, where the channel resistivity can be modulated via control of spin current by applying electric field.

Spin-orbit coupling could also give rise to anisotropic spin relaxation. The theories on crystalline semiconductor and 2-D materials are studied by Averkiev et al [63], Fabian et al. [64], and Huertas-Hernando et al. [65]. They theoretically showed spin relaxation anisotropy in 2-D materials. This dissertation will show that anisotropic spin relaxation is also observed surprisingly in mesoscopic polycrystalline

copper channels using nonlocal spin valves [66]. Rashba spin-orbital coupling on the surfaces of the Cu channels gives rise to different spin-flip probabilities for different spin orientations relative to the crystal axes. The details of this research will be discussed in chapter 4. This finding suggests novel tunability of spin current, not only by its polarization direction but also by electrostatic gating. Electrical modulation of spin current is highly desired functionality since the inception of spintronics.

REFERENCES

[1] W. Thomson, Proc. R. Soc. London **8**, 546 (1857).

[2] T. R. Mcguire and R. I. Potter, IEEE Trans. Magn. **11**, 1018 (1975).

[3] R. C. O'Handley, *Modern Magnetic Materials: Principle and Applications* (Wiley, 1991).

[4] R. L. White, IEEE Trans. Magn. **28**, 2482 (1992).

[5] M. N. Baibich, J. M. Broto, A. Fert, F. N. Van Dau, F. Petroff, P. Eitenne, G. Creuzet, A. Friederich, and J. Chazelas, Phys. Rev. Lett. **61**, 2472 (1988).

[6] G. Binasch, P. Grünberg, F. Saurenbach, and W. Zinn, Phys. Rev. B **39**, 4828 (1989).

[7] S. Blundell, *Magnetism in Condensed Matter* (Oxford University Press Inc., New York., 2001).

[8] S. S. P. Parkin, N. More, and K. P. Roche, Phys. Rev. Lett. **64**, 2304 (1990).

[9] S. S. P. Parkin and D. Mauri, Phys. Rev. B **44**, 7131 (1991).

[10] J. M. Daughton, **216**, 162 (1992).

[11] J. S. Moodera, L. R. Kinder, T. M. Wong, and R. Meservey, Phys. Rev. Lett. **74**, 3273 (1995).

[12] B. Dieny, V. S. Speriosu, S. Metin, S. S. P. Parkin, B. A. Gurney, P. Baumgart, and D. R. Wilhoit, J. Appl. Phys. **69**, 4774 (1991).

[13] S. S. P. Parkin, Annu. Rev. Mater. Sci. **25**, 357 (1995).

[14] U. Hartmann, *Magnetic Multilayers and Giant Magnetoresistance—Fundamentals and Industrial Applications* (Springer: Verlag/Berlin, Germany, 2000).

[15] C. Chappert, A. Fert, and F. N. Van Dau, Nat. Mater. **6**, 813 (2007).

[16] E. Y. Tsymbal and I. Zutic, *Handbook of Spin Transport and Magnetism* (CRC Press, Boca Raton FL, 2012).

[17] J. M. Daughton, J. Magn. Magn. Mater. **192**, 334 (1999).

[18] I. Zutic, J. Fabian, and S. Das Sarma, Rev. Mod. Phys. **76**, 323 (2004).

[19] Z. Shufeng and P. M. Levy, J. Appl. Phys. **69**, 4786 (1991).

[20] E. Y. Tsymbal and D. G. Pettifor, Solid State Phys. **56**, 113 (2001).

[21] T. Jungwirth, J. Wunderlich, and K. Olejnik, Nat. Mater. **11**, 382 (2012).

[22] T. Miyazaki and N. Tezuka, J. Magn. Magn. Mater. **139**, 231 (1995).

[23] S. Ikeda, J. Hayakawa, Y. Ashizawa, Y. M. Lee, K. Miura, H. Hasegawa, M. Tsunoda, F. Matsukura, and H. Ohno, Appl. Phys. Lett. **93**, 82508 (2008).

[24] L. Chua, Appl. Phys. A Mater. Sci. Process. **102**, 765 (2011).

[25] J. Åkerman, Science **308**, 508 (2005).

[26] N. F. Mott, Proceeding R. Soc. A **153**, 699 (1936).

[27] N. F. Mott, Adv. Phys. **13**, 325 (1964).

[28] M. Julliere, Phys. Lett. A **54**, 225 (1975).

[29] Y. Kajiwara, K. Harii, S. Takahashi, J. Ohe, K. Uchida, M. Mizuguchi, H. Umezawa, H. Kawai, K. Ando, K. Takanashi, S. Maekawa, and E. Saitoh, Nature **464**, 262 (2010).

[30] K. Uchida, S. Takahashi, K. Harii, J. Ieda, W. Koshibae, K. Ando, S. Maekawa, and E. Saitoh, Nature **455**, 778 (2008).

[31] F.-J. Chang, J. G. Lin, and S.-Y. Huang, Phys. Rev. Mater. **1**, 31401 (2017).

[32] J. E. Hirsch, Phys. Rev. Lett. **83**, 1834 (1999).

[33] M. Johnson and R. H. Silsbee, Phys. Rev. Lett. **55**, 1790 (1985).

[34] F. J. Jedema, A. T. Filip, and B. J. Van Wees, Nature **410**, 345 (2001).

[35] F. J. Jedema, H. B. Heersche, A. T. Filip, J. J. A. Baselmans, and B. J. van Wees, Nature **416**, 713 (2002).

[36] T. Kimura, J. Hamrle, Y. Otani, K. Tsukagoshi, and Y. Aoyagi, Appl. Phys. Lett. **85**, 3501 (2004).

[37] S. O. Valenzuela and M. Tinkham, Appl. Phys. Lett. **85**, 5914 (2004).

[38] Y. Ji, A. Hoffmann, J. S. Jiang, and S. D. Bader, Appl. Phys. Lett. **85**, 6218 (2004).

[39] S. Garzon, I. Zutic, and R. A. Webb, Phys. Rev. Lett. **94**, 176601 (2005).

[40] S. O. Valenzuela and M. Tinkham, Nature **442**, 176 (2006).

[41] X. Lou, C. Adelmann, S. A. Crooker, E. S. Garlid, J. Zhang, K. S. M. Reddy, S. D. Flexner, C. J. Palmstrøm, and P. A. Crowell, Nat. Phys. **3**, 197 (2007).

[42] Y. Ji, A. Hoffmann, J. S. Jiang, J. E. Pearson, and S. D. Bader, J. Phys. D. Appl. Phys. **40**, 1280 (2007).

[43] P. C. Van Son, H. Van Kempen, and P. Wyder, Phys. Rev. Lett. **58**, 2271 (1987).

[44] Y. Cai, Y. Luo, C. Zhou, C. Qin, S. Chen, Y. Wu, and Y. Ji, J. Phys. D. Appl. Phys. **49**, 185003 (2016).

[45] M. Johnson, Phys. Rev. Lett. **70**, 2142 (1993).

[46] R. J. Elliott, Phys. Rev. **96**, 266 (1954).

[47] M. I. D'yakonov and V. I. Perel', Sov. Phys. Solid State **13**, 3023 (1972).

[48] G. L. Bir, A. G. Aronov, and G. E. Pikus, Zh. Éksp. Teor. Fiz. **69**, 1382 (1975).

[49] R. Hanson, L. P. Kouwenhoven, J. R. Petta, S. Tarucha, and L. M. K. Vandersypen, Rev. Mod. Phys. **79**, 1217 (2007).

[50] Y. Yafet, in *Solid State Phys. Vol. 14* (1963), pp. 1–98.

[51] F. J. Jedema, M. S. Nijboer, A. T. Filip, and B. J. van Wees, Phys. Rev. B **67**, 85319 (2003).

[52] G. Mihajlovi, J. E. Pearson, S. D. Bader, and A. Hoffmann, Phys. Rev. Lett. **104**, 237202 (2010).

[53] M. I. Dyakonov, in *Spin Phys. Semicond.* (2008), pp. 1–28.

[54] G. Dresselhaus, Phys.Rev. **100**, 580 (1955).

[55] E. I. Rashba, Sov. Phys. Solid State **2**, 1109 (1960).

[56] Y. A. Bychkov and E. I. Rashba, JETP Lett. **39**, 66 (1984).

[57] J. Nitta, T. Akazaki, H. Takayanagi, and T. Enoki, Phys. Rev. Lett. **78**, 1335 (1997).

[58] T. Schäpers, G. Engels, J. Lange, T. Klocke, M. Hollfelder, and H. Lüth, J. Appl. Phys. **83**, 4324 (1998).

[59] V. I. Rashba, E.I. and Sheka, Sov. Phys. Solid State **1**, 143 (1959).

[60] F. T. Vasko, JETP Lett. **30**, 541 (1979).

[61] A. Takayama, *Anomalous Rashba Effect of Bi Thin Film Studied by Spin-Resolved ARPES* (Intech, 2017).

[62] S. Datta and B. Das, Appl. Phys. Lett. **56**, 665 (1990).

[63] N. S. Averkiev, L. E. Golub, and M. Willander, J. Phys. Condens. Matter **14**, R271 (2002).

[64] J. Fabian, A. Matos-Abiague, C. Ertler, P. Stano, and I. Zutic, Acta Phys. Slovaca **57**, 565 (2007).

[65] D. Huertas-Hernando, F. Guinea, and A. Brataas, Phys. Rev. Lett. **103**, 146801 (2009).

[66] C. Zhou, F. Kandaz, Y. Cai, C. Qin, M. Jia, Z. Yuan, Y. Wu, and Y. Ji, Phys. Rev. B **96**, 94413 (2017).

Chapter 3

DEVICE FABRICATION AND MEASUREMENT TECHNIQUES

In this chapter, I will briefly introduce the experimental techniques that are used in our studies, including the fabrication of lateral nonlocal spin valve devices, and measurement setup for nonlocal spin transport measurements.

3.1 Fabrication and Measurement Steps

Figure 3.1 shows a flow chart of the process for the experimental procedures starting from sample fabrication steps through electrical measurement. First, photolithography is used to pattern gold electrical contact pads on the substrate. Subsequently, electron beam lithography is used to fabricate nonlocal spin valve devices. After the deposition of the metals and subsequent lift of process, the electrical measurements in our devices were carried out with the alternating current (AC) lock-in method [1].

3.2 Lithoghraphy

Lithography is a principal micro- and nano-fabrication technique. In this process, a defined pattern is direct-written or transferred from a mask to a smooth surface. We used two different lithography techniques in our work: Photolithography and Electron beam lithography. Contact pads are formed using the photolithography process, and nanoscale nonlocal spin valve (NLSV) devices are fabricated using the electron beam lithography process.

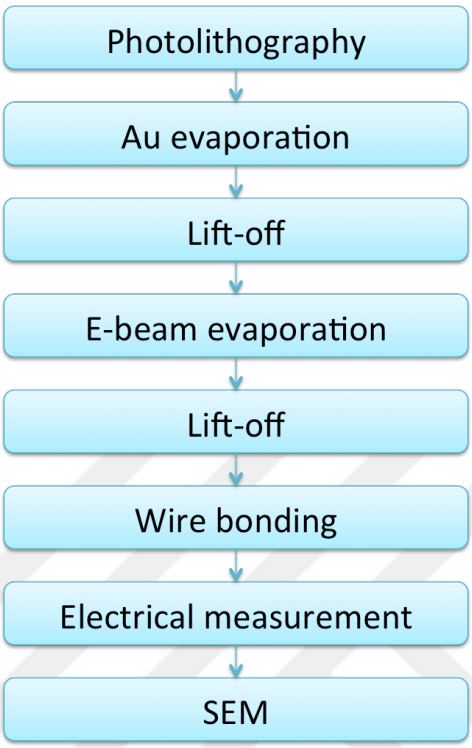

Figure 3.1: Flowchart shows the steps of sample fabrication.

3.2.1 Photolithography

Photolithography technique is used in our work to fabricate alignment marks for the next step e-beam lithography and for electrical contact pads (scaled from 200 by 200 nm to 400 by 400 nm), which enable connection between the NLSV devices and the chip carrier. In a photolithography process, UV light is used to transfer a defined pattern on the photo-mask onto a thin layer of a photoresist (light sensitive material) on the substrate. This is a relatively quick method where the whole pattern on the photo-mask can be transferred onto the substrate at the same time.

In this study, the photolithography process is carried out using Oai Hybralign Series 200 model Mask aligner and UV Exposure System. In **Figure 3.2**, the schematic diagram shows the major steps involved in the process of photolithography.

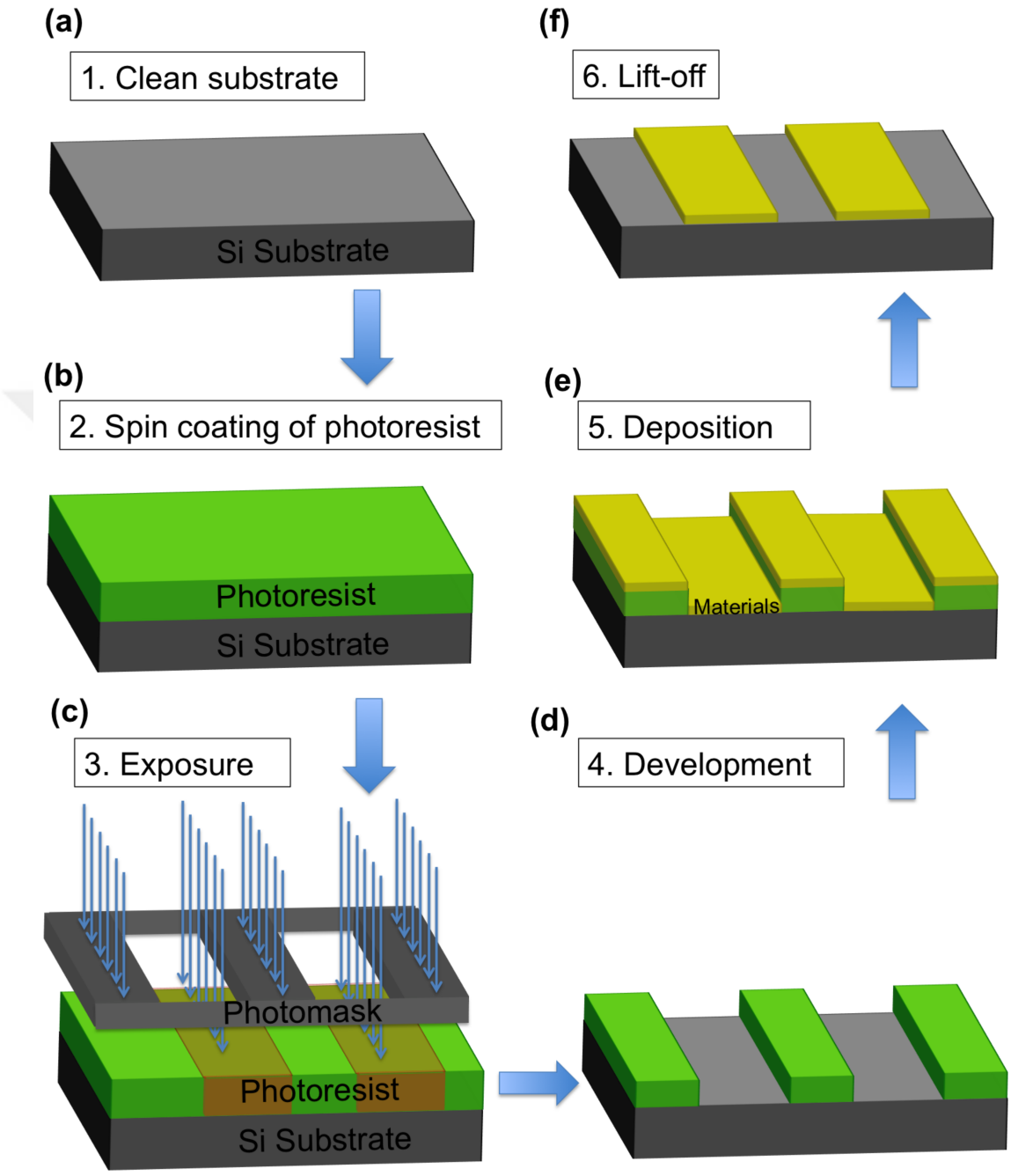

Figure 3.2: Flowchart of a positive photolithography process (a) Si Substrate; (b) A positive photoresist is spun onto Si substrate; (c) The photoresist is exposed to UV light through a photomask; (d) After the development of photoresist; (e) desired material is deposited onto the substrate; (f) the material on the remaining resist are removed by lift-off of the resist.

These steps are cleaning the surface, spin coating of the photoresist, UV light exposure, development for exposed photoresist, thin film deposition, and lift off.

3.2.1.1 Cleaning of the Wafer

Silicon wafers covered with 300-nm thick insulating silicon nitride (SiN) are used as the substrates in these experiments. Cleaning of the substrate is needed to remove any dust particles and chemical contaminants from the surface of it, and it is done usually in three steps. First, the silicon wafer is cleaned with the acetone and ethanol solutions sequentially by an ultrasonic agitation for 15 minutes each. Second the wafer is transferred into deionized water and ultrasonic agitation is used again for 15 minutes. Third, the wafer is dried by blowing nitrogen (N_2) gas. The photomask that we are going to use in the photolithography process is also cleaned by acetone, ethanol, and DI water followed by blowing dry with nitrogen gas.

3.2.1.2 Spin Coating

Spin coating is done usually in 2 steps. First, spin coating is used to produce a thick layer of photoresist, which is sensitive to UV lights, on the substrate. The liquid photoresist (AZ 1512) is dispensed onto the center of the wafer, which is secured tightly in the spinner. Then the wafer is spun at 4000 RPM for 60 seconds to spread the photoresist uniformly on the surface of it. The second step is soft-baking it at 115 °C on a hot plate for 60 seconds. Soft-bake is employed to evaporate the solvent from the photoresist and to improve the resist adhesion on the substrate. The thickness of the photoresist depends on the spinning speed, time of the spinning, and viscosity of the photoresist liquid. In our work the resulting photoresist thickness is around 1.4 μm **[Fig. 3.2(b)]**.

3.2.1.3 Light Exposure

After spin coating, the wafer is placed on the mask aligner (OAI HYBRALIGN SERIES 200) and using the microscope the photomask is aligned with the wafer and the wafer stage is moved toward the photomask until the surface of the resist will be in direct contact with the mask. After that the light sensitive photoresist covered on the wafer is exposed to ultraviolet light for 6 seconds through a photomask, which defines the pattern to be created in the photoresist layer **[Fig. 3.2(c)]**. Depending on the photoresist type, the light exposed areas of the photoresist become soluble (positive photoresist) or insoluble (negative photoresist) in the developer solvents.

3.2.1.4 Development

Following light exposure, the wafer is immersed in a developer solvent (Rohm Haas MF319) around 15 seconds in order to remove the defined areas of the photoresist on the surface of the wafer. In our work, since positive photoresist is used on the substrate, the light exposed areas of the resist will be removed in the developer solvent. As a result, the remaining photoresist on the wafer will have the same pattern with the fabricated photomask **[Fig. 3.2(d)]**.

3.2.1.5 Deposition and Lift-off

After the development process, a 100 nm-thick gold film is deposited on the wafer through a thin film deposition method **[Fig. 3.2(e)]**. After the evaporation is done, lift-off is the last step. The wafer is immersed into acetone around one hour to remove the unwanted resist residues left on the wafer after the development process. Hence, after the lift-off process only the deposited gold film remains on the wafer.

These remaining gold film pads on the wafer are used as the contact pads in the nonlocal spin valve devices **[Fig. 3.2(f)]**.

3.2.2 Electron Beam Lithography

Electron-beam lithography (e-beam lithography) is a fundamental technique of the fabrication of devices at the nanometer scale. With this technique, an accelerated beam of electrons is used in order to write nanoscale patterns directly (without using a mask) onto the substrate that has been covered with charge sensitive resist. The desired pattern can be generated using a computer program like AutoCAD etc. The main advantages of this method over the conventional photolithography method include higher resolution, down to 10 nm, and greater flexibility and compatibility. But the time required to write the pattern is long due to the scanning process.

3.2.2.1 Double Layer Shadow Mask

In this work, e-beam lithography is used to fabricate nonlocal spin valve devices. To be able to fabricate these devices without breaking vacuum (in-situ), double layer resists, which have different sensitivities to the electron beams, are formed on the wafer and suspended shadow mask is created from these two layers. The major steps for the electron beam lithography process are schematically shown in **Figure 3.3**. PMGI (polydimethylglutarimide) and PMMA (polymethyl methacrylate), positive e-beam resists, are used as bottom and top layers, respectively. After the deposition of gold contact pads on the substrate, first, PMGI, the bottom layer, is spin

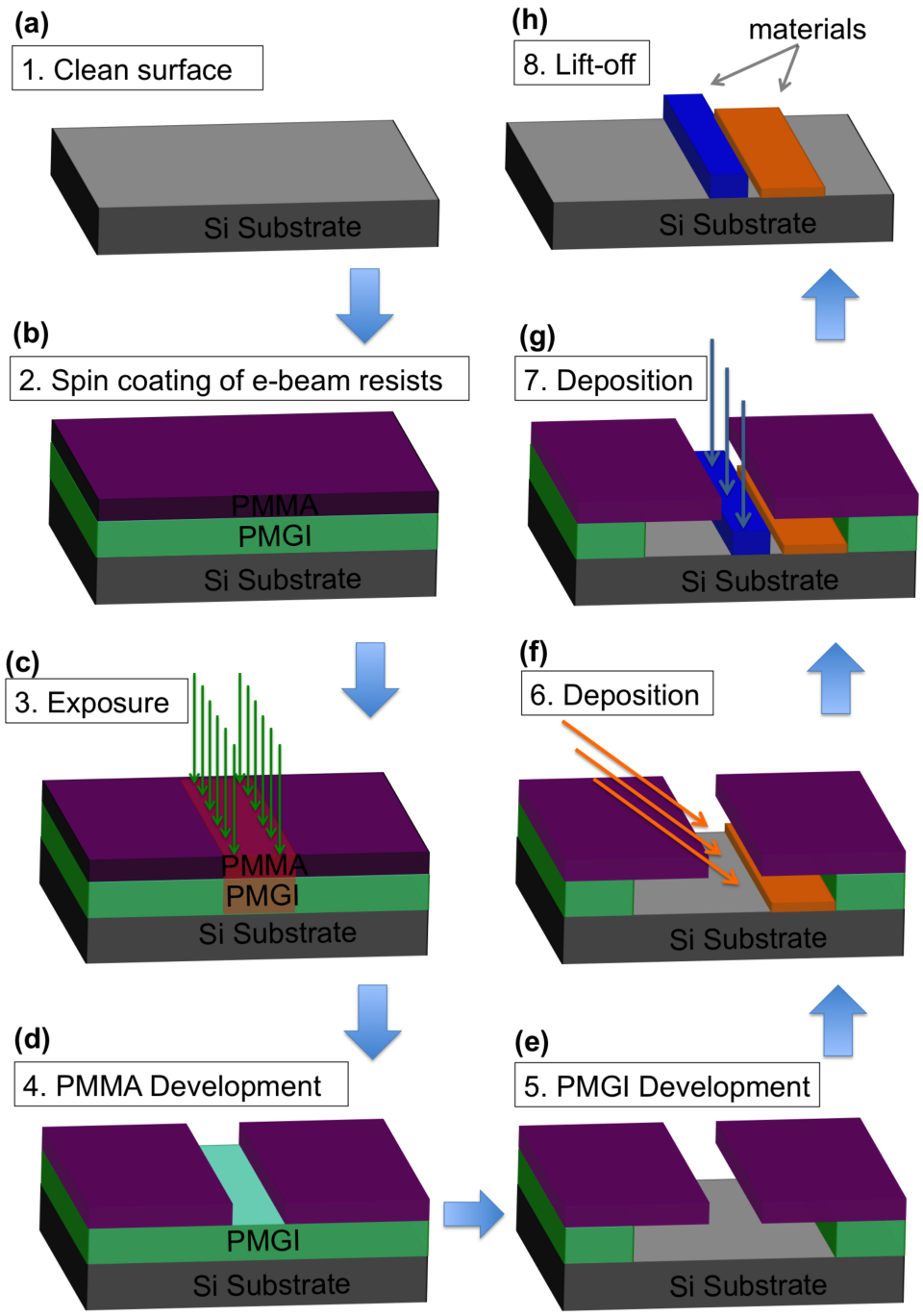

Figure 3.3: (a-e) Electron beam lithography for fabrication of double layer shadow mask; (f) & (g) two different structures can be separated on the substrate by angle evaporation of the materials through a shadow mask; (h) after lift-off of remaining resists, desired patterns are left on the substrate.

coated on the gold film at a speed of 3000 rpm for 60 seconds and then post baked at 210 C for 3 minutes. Second, PMMA, the top layer, is spin coated on the PMGI resist at 5000 rpm for 60 seconds then post baked at 190 C for 4 minutes.

After the spin coating of both layers, a predesigned pattern by a computer software are written on the wafer using electron beam lithography with the high energy electron beam generated by the Raith e-LINE system located at the Maryland Nano Center. After the exposure, e-beam changes the chemical properties of the exposed areas of the resists; the polymer chains of these areas are broken and become soluble in the developer. The electron beam parameters typically used in this study were a voltage of 20 kV and aperture of 30 μm, and write fields of 100x100 μm^2 were used for our wafers. The area dose was 245-$\mu C/cm^2$ and line dose was 4000-pC/cm for the e-beam writing.

Following e-beam exposure, the resists of top and bottom layers are developed separately. First, the wafer is immersed in MIBK:IPA 1:3 developer for 90 seconds and then in IPA for 30 seconds to develop for the top layer PMMA resist followed by rinsed in deionized water for 60 seconds. The optical picture of the substrate after the development of the PMMA layer is shown in **Figure 3.4(a)**. Second, the bottom layer PMGI resist is developed by dipping it in the XP101A developer for around 5 to 6 minutes. Here we used weaker solvent for the top layer to prevent intermixing of the top and bottom layers during the application of the second step development. The optical picture of the substrate after the development of PMGI is shown in **Figure 3.4(c)**. Since the bottom layer PMGI resist has higher sensitivity to electron beams and the development period is long, the top layer PMMA resist is suspended on the bottom

layer PMGI resist, and forms a structure similar to the two layer suspended shadow mask as illustrated in **Figure 3.4(d)**.

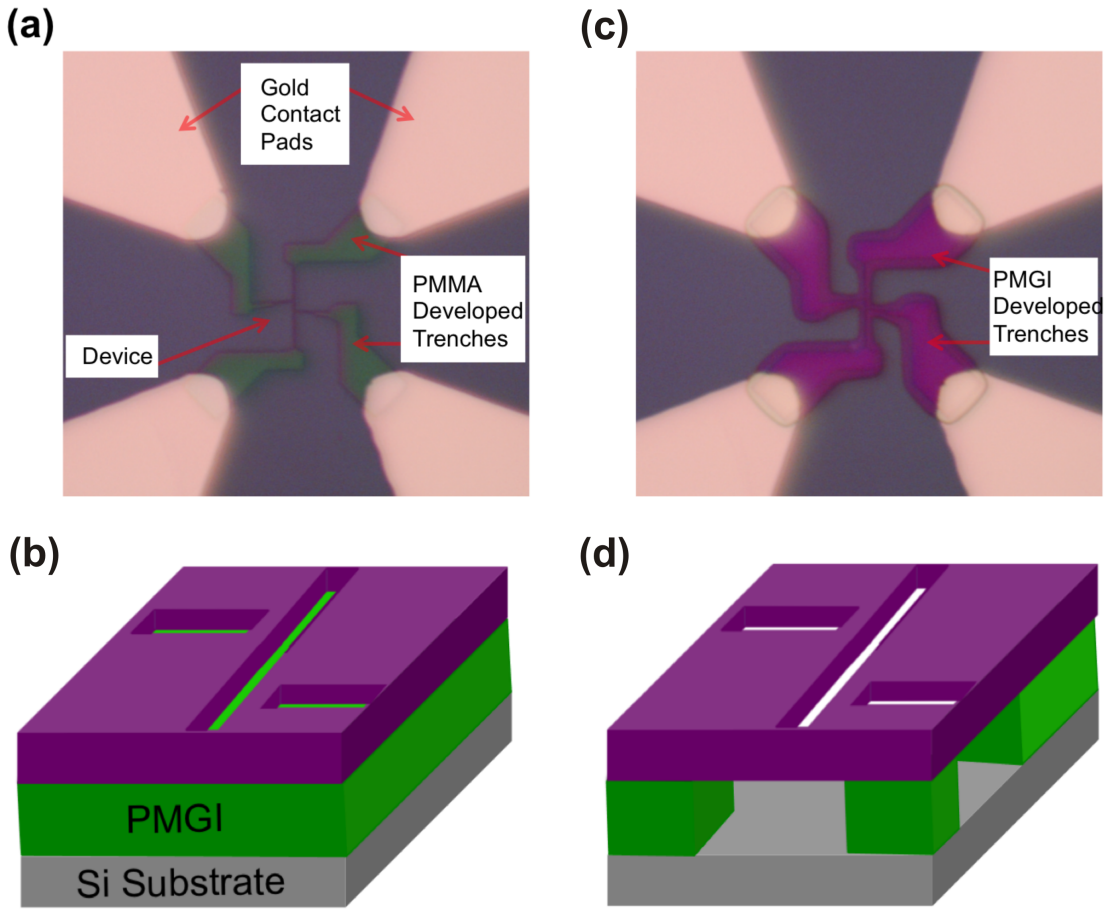

Figure 3.4: (a) & (b) Optical microscope image and an illustration of the structure after the development of the top layer (PMMA); (c) & (d) Optical microscope image and an illustration of the shadow mask after the development of the bottom layer (PMGI).

3.3 Electron Beam Evaporation

3.3.1 Principles

In this study, we used electron beam evaporation performed in an ultrahigh vacuum system. Electron beam evaporation technique has many advantages for different types of applications. This deposition system has the ability to evaporate not only metals and alloys but also compounds such as oxides, especially materials with high melting points. The other advantage is that it can produce significantly higher evaporation rates due to a large amount of heat that is concentrated only on the source material. Since the evaporated molecules in the high vacuum chamber travel in straight lines without scattering, this deposition system enables the deposition process called shadow evaporation. This section reviews the electron beam evaporation deposition process along with the principles, equipment for the electron beam evaporation system and its applications.

3.3.2 Electron Beam Evaporation Process

Electron beam evaporation is a deposition process in which high energy electron beams generated from a charged tungsten filament are sent through the target material placed on the bottom of the vacuum chamber to evaporate and transform it to the gaseous phase for deposition on the substrate. **Figure 3.5** shows a schematic diagram for a typical electron beam evaporation system. To generate the electron beam from the tungsten filament, an electric current is sent through the filament and this gives rise to thermionic emission of electrons. These thermionically emitted electrons from the tungsten filament are then focused by external confocal magnetic fields to form a beam of high-energy electrons and then directed towards the target material. When the electron beam hits the source material, the kinetic energy of

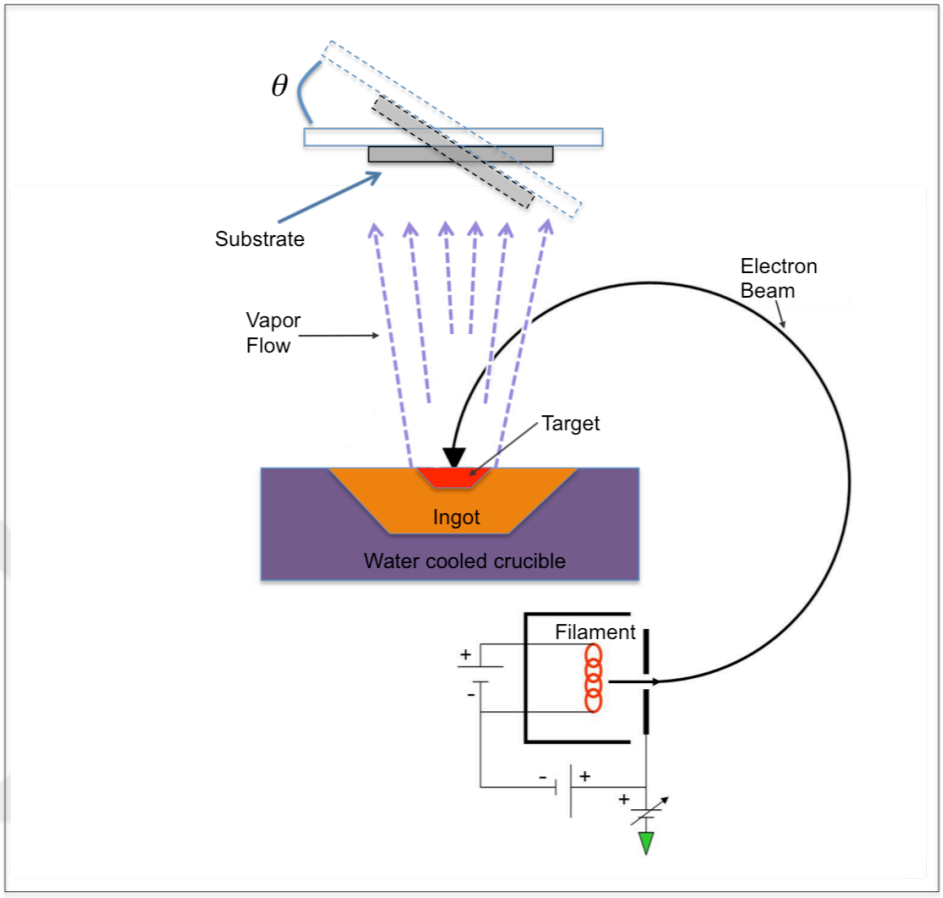

Figure 3.5: A schematic diagram of electron beam evaporation process. Figure is adapted from [2].

the electron beam is transferred to the target material as thermal energy and gives rise to heating and evaporation of the material. When the desired evaporation rate is reached, the sample holder, which is positioned on the top of the chamber, is rotated to face down as it is seen in **Figure 3.5**. Since the evaporation in the vacuum is highly anisotropic, this resulting vapor of source material from the crucible condenses on the walls of the chamber and on the substrate that is mounted surface down at the top of the chamber. The rate of the deposition is controlled by changing the current on the

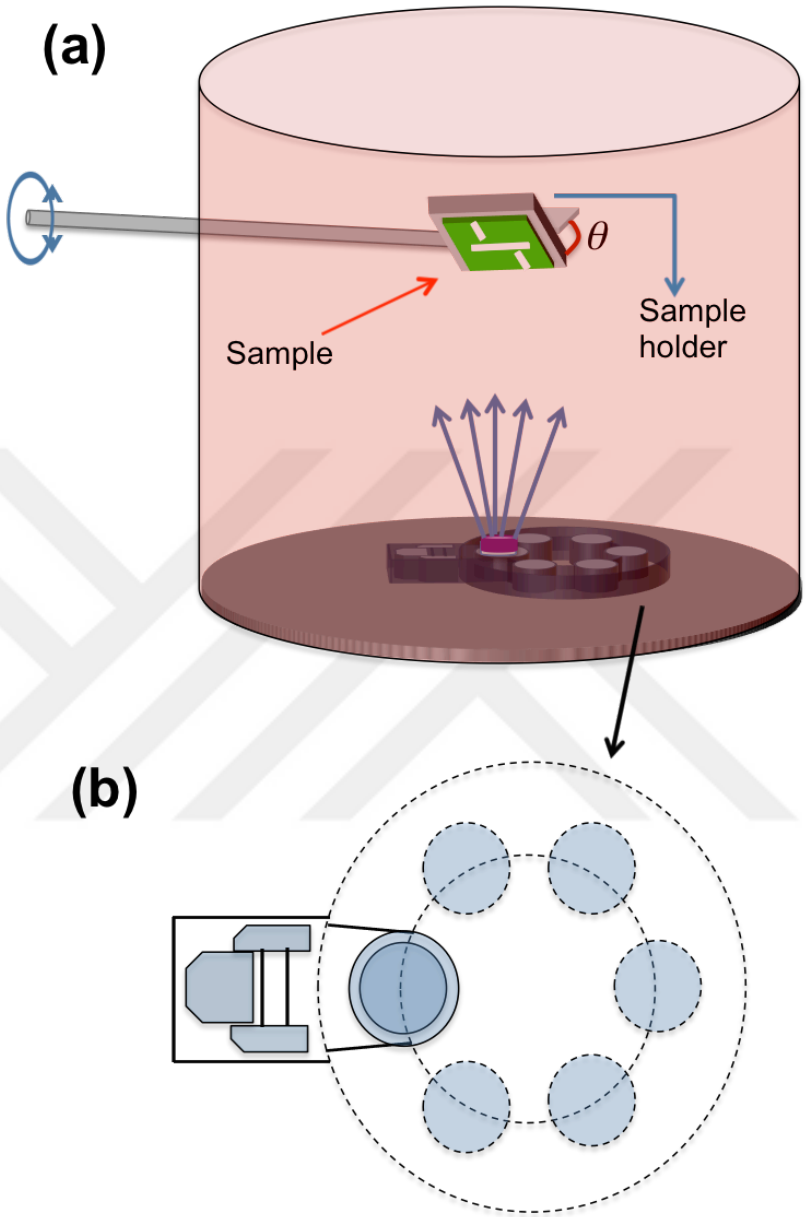

Figure 3.6: (a) A schematic diagram for a high vacuum deposition chamber. The three slits on the sample represent the magnified designed pattern for e-beam lithography. The materials are evaporated through those openings from different angles θ; b) Schematic representation of the six crucibles; only one of these target materials are deposited at a time, the other five are under the self-seal protector.

target material. A crystal monitor in the chamber is used to measure the thickness of the thin film during the deposition and when the desired thickness has been achieved, the sample holder is quickly rotated face up; this will prevent more deposition on the substrate. A rotatable source of crucibles is present on the bottom of the chamber containing six different source materials **[Figures 3.6(a) and (b)]**. So when the deposition of the first layer is done, subsequent thin films are evaporated in a similar process without breaking the vacuum.

3.3.3 Shadow Evaporation Method

Here, the fabrication of nonlocal spin valve devices by angle evaporation is going to be discussed. In our study we used the angle shadow evaporation method to fabricate the nonlocal spin valve devices. This deposition method is capable of doing all depositions in a single vacuum step by evaporating the different materials from different angles through the mesoscopic suspended shadow mask, so that the clean interfaces between the materials are provided. As we discussed in the section 3.2.3, a shadow mask is created by using double layer resists, which have different sensitivities to electron beams.

The sample holder on the top of the vacuum chamber is connected to the end of a rotary feedthrough. Since it can be rotated freely 360-degree about its long axis as shown in **Figure 3.6(a)**, the sample, mounted to the holder, can be tilted, so that the magnetic and nonmagnetic materials can be deposited through the stencil mask at different angles θ. Here θ is defined as the angle between the evaporation direction and the line, which is normal to the surface of the substrate on the sample holder. In this case, the specific location of deposited materials on the substrate can be controlled by adjusting the angle θ between the evaporation direction and the plane of the

sample, so that a nanobridge of a nonmagnetic metal can be formed between the two ferromagnetic metals.

Figure 3.4(d) illustrates the suspended shadow mask, where the top layer is the PMMA, and the bottom green layer is the PMGI. The higher sensitivity of the PMGI layer than PMMA layer to the electron beam causes larger empty areas under the openings in the top PMMA layer after the development. Then the electron beam depositions of ferromagnetic and nonmagnetic metals are done through these openings from different angles as shown in **Figure 3.7**. The depositions are performed in a chamber with a base pressure in the order of 10^{-8} Torr. First, Py was deposited through one of the horizontal openings at an angle of 70^{o} from the substrate normal, and then through the other horizontal opening at the same angle but from the opposite side. As a result two laterally displaced Py electrodes are formed on the substrate as shown in **Figure 3.7(b)**. During these depositions, since the width of the vertical opening is very narrow, only about 150 nm, the atomic flux of Py hits the side wall of the PMMA resist and there will be no deposited Py atoms in the vertical opening. After the deposition of the Py magnetic materials as ferromagnetic electrodes from both sides, AlO_x as a barrier and Cu as a nonmagnetic material is evaporated through normal direction to the substrate, forming two Py/AlO_x/Py junctions as shown in **Figures 3.7(c)** and **(d)**. The main purpose of the AlO_x layer is to mitigate the mismatch of spin resistance between Cu and Py to maintain a substantial spin polarization.

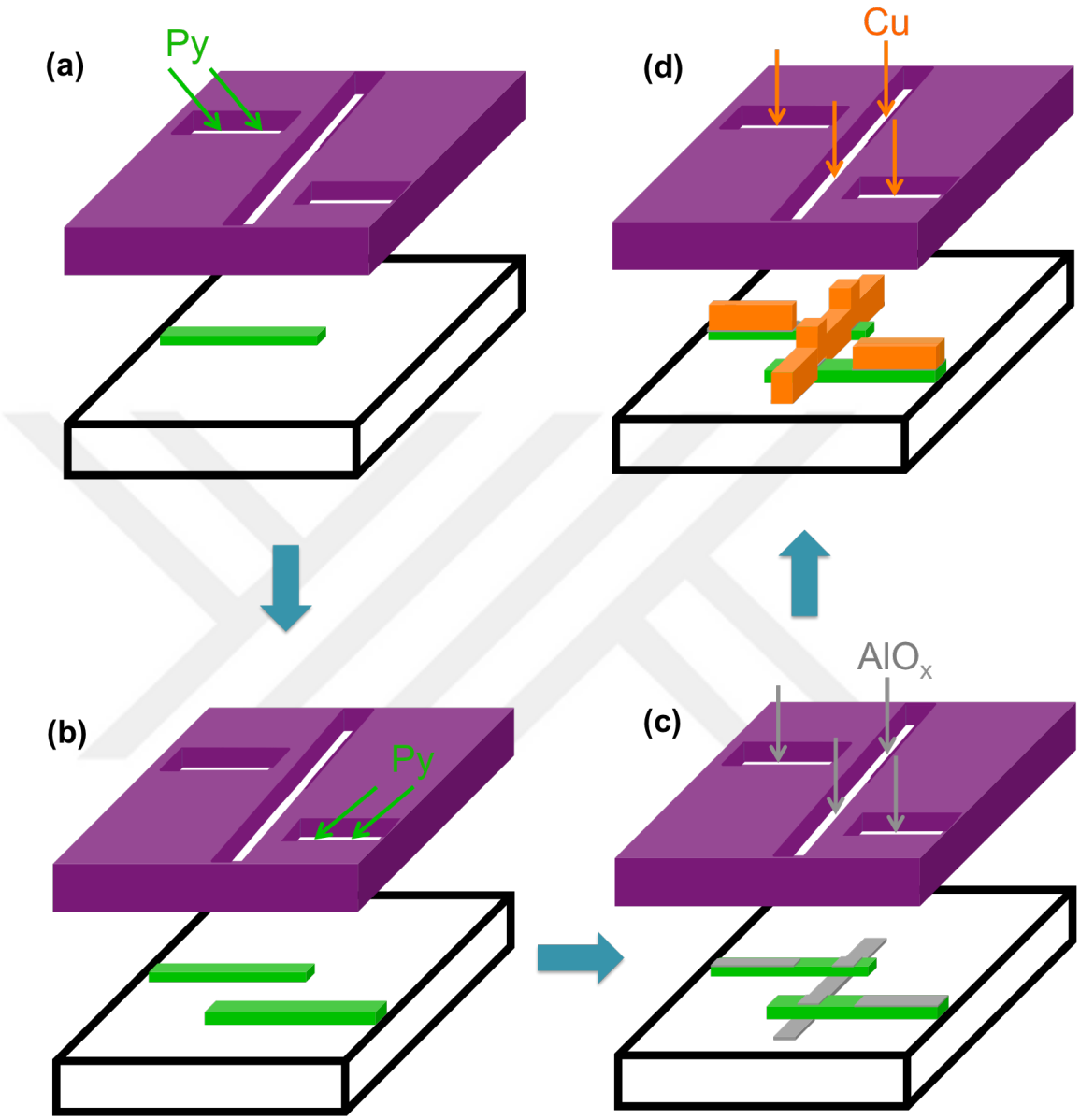

Figure 3.7: Schematic representation of the multi angle shadow evaporation technique in the fabrication of nonlocal spin valve structures; (a) & (b) Shadow evaporation of Py electrodes from two orientations at an angle θ to the substrate normal (c) & (d) Evaporation of AlO_x and Cu through normal direction so that the materials overlap to create a lateral spin valve device. Figure is adapted from [3].

After the deposition of the materials on the substrate, the remaining resists are lifted-off in a more strong solvent to remove unexposed areas of the resists. First the substrate is immersed in the PG remover for 15 minutes, followed by immersion in acetone for 45 minutes. Then it is flushed with acetone, ethanol and deionized water, respectively. Thus, only the evaporated materials remain on the substrate. After lift-off, the final pattern is examined using the optical and SEM microscope. Real parameters of the devices, such as widths of FM electrodes, the center-to-center distance between them, and the width of the NM channel for each device are measured by SEM microscope. The Scanning electron microscopy (SEM) picture of a real NLSV device fabricated in our lab is shown in **Figure 3.8**.

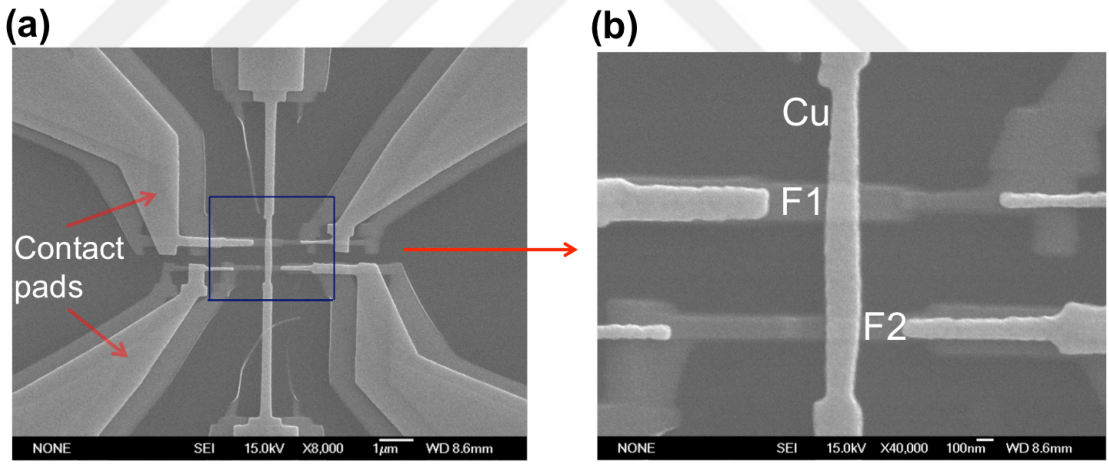

Figure 3.8: Scanning Electron Microscopy (SEM) images of a fabricated lateral spin valve device.

3.4 Experimental Setup for Spin transport Measurements

3.4.1 Wire Bonding

Following the electron beam lithography process, 2 inch silicon wafers are cut into nine 1 cm by 1 cm chips. Typically, many devices (25 to 200) resided on each substrate, **[Fig. 3.9]**. After the fabrication of the devices, the substrate was mounted onto 16 pin gold chip carriers using a thin coat of grass and double sided tape, and then three or four devices were wire bonded each time to make connections between the gold contact pads of the devices on the substrate and the contact pads on the chip

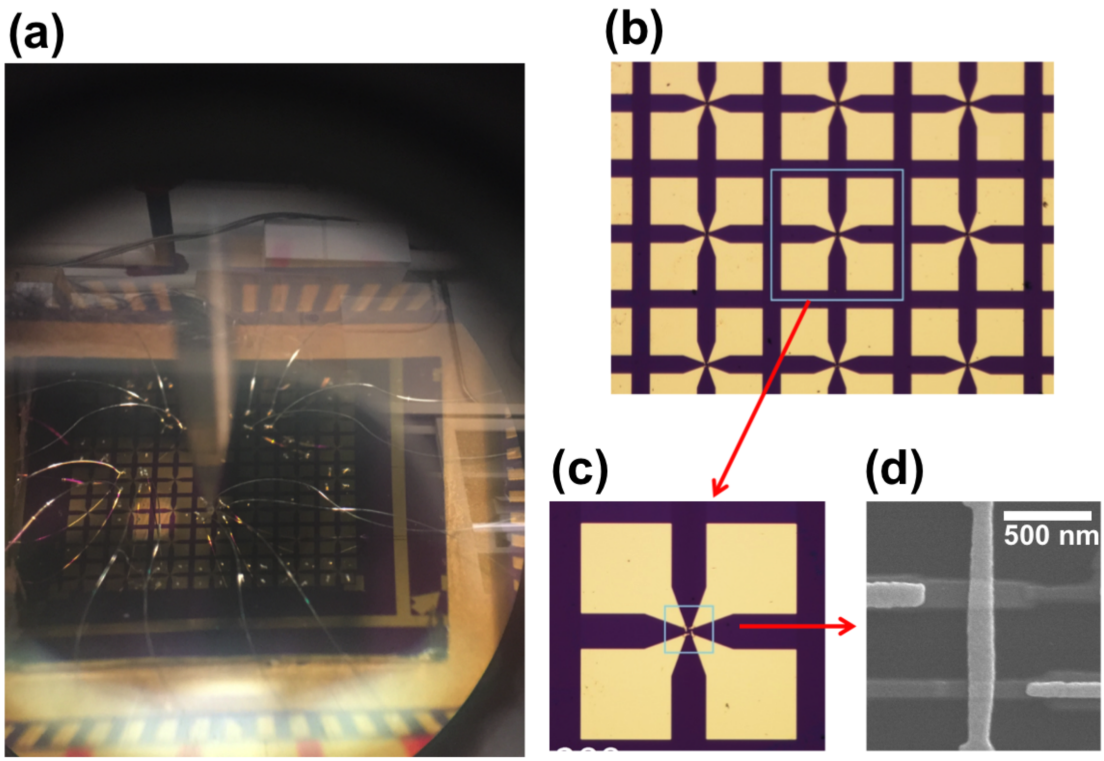

Figure 3.9: (a) A typical wire bonded substrate, contact pads of the devices is connected to the chip carrier with Al wires; (b), (c) & (d) the nonlocal spin valve devices on the substrate, (d) the image of an NLSV device from SEM microscopy.

carrier using K&S model 4522 Al-wire bonder. A typical wire bonded substrate containing nonlocal spin valve devices is shown in **Figure 3.9(a)**.

3.4.2 Electrical Measurements

Main work in this dissertation was done by measuring the response of the electrical transport properties of the nonlocal spin valve devices to the changing magnetic field using standard four-probe measurement method. The diagram of the measurement setup is illustrated in **Figure 3.10**. The charge injection current I_e is directed between F_1 (I+) and the right end of the Cu channel (I-). The nonlocal voltage V_{nl} is detected between F_2 (V+) and the left end of the Cu channel (V-). The nonlocal signal R_s, defined as $R_s = V_{nl}/I_e$, is recorded as a function of magnetic field B. Resistance of Cu channel is measured by applying current through Cu channel and voltage is detected between F_1 and F_2 electrodes.

SR830 DSP Lock-in Amplifier or the Keithley 6221 Precision DC/AC Current Source models were used to apply the AC current and the SR830 DSP Lock-in Amplifier is also used to detect the AC voltage signal. A 10 kΩ large resistor is connected in series with the AC output on the lock-in amplifier to convert the output voltage into output current. The advantage of the lock-in technique, which filters out all the frequency of the measured AC voltage other than the frequency of the injected AC current, is that the signal could be detected even in a noisy background. Keithley 6220 Precision DC Current Source and Keithley 2182A Nanovoltmeter instruments were used for DC current source and DC voltmeter, respectively.

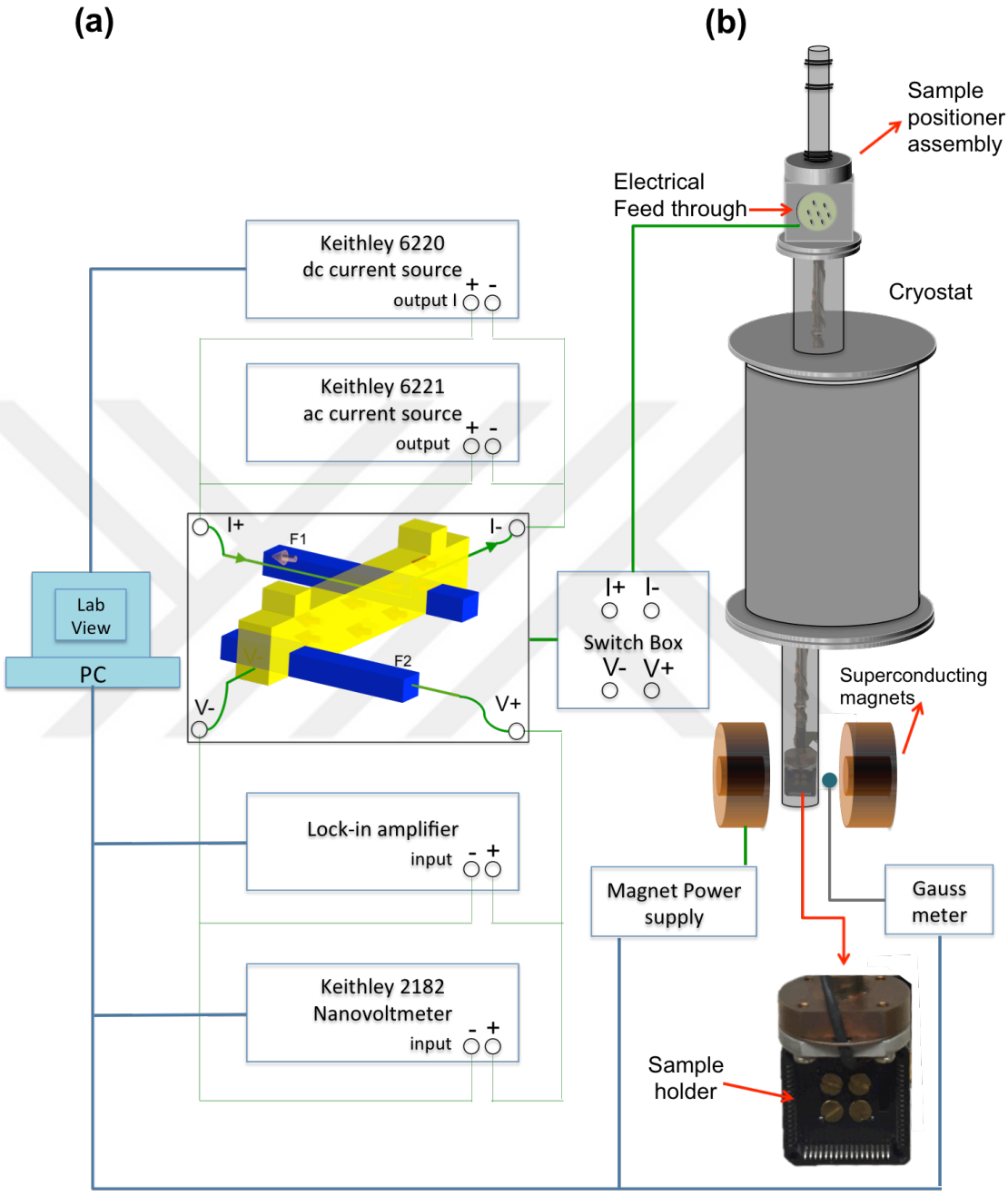

Figure 3.10: Block diagram of the measurement setup performed in this work. Green lines indicate electric signals and blue lines indicate GPIB signals; (b) Schematic diagram of a cryogenic system for the low temperature measurement, the wire bonded substrate is mounted on the sample holder.

We did three different types of measurements in this study. First type is the measurement of the spin resistance R_s as a function of the applied magnetic field. The difference of the spin resistances corresponding to the parallel and antiparallel states of the FM layers gives nonlocal spin signal. Using this technique we also measured anisotropic spin signal of the devices using specially designed nonlocal spin valve devices, this will be discussed in detail on chapter 4. Second type is anisotropic spin signal measurement where the magnetic field is fixed and R_s values are measured by rotating the sample back and forth by 90-degree angles. Third type is another anisotropic spin signal measurement where the sample is fixed and R_s values are measured under the periodically rotating magnetic field between the direction along the ferromagnetic electrodes and along the Cu channel. In this method, the rotational field is accomplished by a fixed 0.03-T bias field in one direction while sweeping much larger magnetic field in the other direction.

Nonlocal spin signal measurements were done either in a variable temperature probe station or in a Helium (He) cryogenic system, which allows control of the temperature in the range from 5K to room temperature. During the measurement in the Helium (He) cryogenic system, the temperature of the sample can be adjusted to the desired value by the Lakeshore 322 temperature controller. In this study, the cryogenic system that we used is the Janis Research PTSHI-950 Refrigerator System [4]. A schematic diagram of the cryogenic system is shown in **Figure 3.10(b)**. After wire bonding, the prepared chip carrier with the sample on it was loaded into the pulse tube in the cryogenic system, via a long rod, which has 16 contacts. They enable the connection of the sample to a switch box through 16 BNC connectors. After the long rod is inserted into the pulse tube, the preferred device could be measured by

connecting corresponding terminals of the device on the switch box to the measurement meters by BNC cables.

In the method of the anisotropic signal measurement by rotating the sample back and forth, the chip carrier is placed onto a rotatable stage as shown in **Figure 3.11**, and then this stage is placed between two magnetic poles. In this case, even if the magnetic field is applied continuously in the same direction, the rotating system allows to vary the direction of the magnetic field respect to the nonlocal spin valve device.

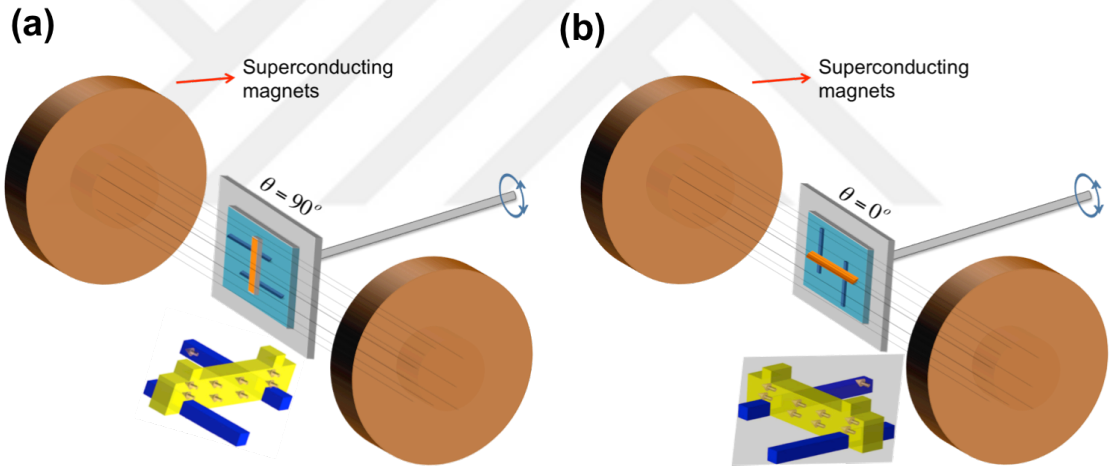

Figure 3.11: Schematic diagram for the anisotropic spin signal measurement under the fixed magnetic field as the NLSV device is rotated between (a) 0^{o} position and (b) 90^{o} position periodically to alternate the aligned spins between the directions perpendicular to Cu channel and parallel to Cu channel, respectively. The 3-D diagrams at the bottom show the directions of the spins in the nonlocal spin valve devices for each case. The spins are directed along the direction of the applied magnetic field.

In this work, the external magnetic field was generated by a combination of two large coils and water-cooled electromagnets by GMW Model 5403 with Kepco Bipolar Power Supply. The magnitude of the magnetic field can be reached to several Tesla and controlled by changing the output current of the power supply. In a regular measurement procedure, an AC current of 100 μA is injected through the specified terminals and the AC voltage is detected between other terminals under the applied magnetic field . And during the measurement, the experimental setup can be automatically controlled and recorded through LabView programs from National Instruments. When all measurements are done on an NLSV, the actual lateral geometry of the nanowires was determined by scanning electron microscopy (SEM).

REFERENCES

[1] A. Daire, W. Goeke, and M. A. Tupta, *New Instruments Can Lock Out Lock-Ins* (2005).

[2] https://en.wikipedia.org/wiki/Electron-Beam_physical_vapor_deposition, n.d.

[3] S. Chen, 'Dissertation for PhD degree at the University of Delaware,' 2014.

[4] "Operating Instructions for the Janis Research PTSHI-950 Refrigerator System.,"

Chapter 4

ANISOTROPIC SPIN RELAXATION IN MESOSCOPIC NONMAGNETIC CHANNELS INDUCED BY SURFACE SPIN-ORBIT EFFECTS

4.1 Introduction

Spintronics is a new field of electronics, which is based on spin control of electrons and promises for future logic and memory applications due to energy efficiency, nonvolatility, scalability, and higher speed. Spin-orbit (SO) effects enrich the spintronics tool set by generating spin currents [1,2], spin torques [3,4], and complex spin textures [5–8]. Furthermore, SO effects allow for effective modulation of spin currents and spin accumulation using an electrostatic gate [9–12]. Materials with heavy elements have been assumed to be essential for SO effects, but their spin-relaxation lengths are typically short because of the higher rates of spin relaxation. A long spin-relaxation length is highly desirable since it enables long-distance transport of spin current. However, the elusive coexistence of long spin-relaxation length and spin-orbital effects is not common in the same material. Simple metals such as Cu and Al have substantial spin-relaxation lengths and can transport large spin currents, but SO effects were not previously expected.

Spin current, which is essential to spintronics technology, is a tensorlike quantity describing a flow of spin angular momenta with a polarization direction [13]. Tunability of spin current has been a desired functionality since the inception of spintronics [9], but it remains a major challenge despite some promising progress [10]. Unlike an electrical current, a spin current decays as it propagates through a material

because of the ubiquitous spin relaxation. Spin-relaxation length, which characterizes the effective transport distance of a spin current, is a crucial quantity for describing many emergent phenomena, such as spin-Hall magnetoresistance [14–16], spin Seebeck effect [17] and spin pumping [18]. If spin-relaxation length depends on the polarization direction, as the tensorlike nature of spin current would suggest, then the intriguing technological prospect arises that spin current could be tuned by polarization direction through the seemingly undesirable process of spin relaxation.

According to theories, such anisotropic spin relaxation could arise from various types of spin-orbit (SO) effects in semiconductors [19,20], graphene [21,22], or crystalline metals [23] and is relevant to the fundamental question of whether the spin relaxation is of the Elliot-Yafet [24,25] or Dyakonov-Perel type [26]. The anisotropic spin-relaxation time was observed experimentally in low-dimensional semiconductor systems [27–29] and attributed to the interplay of various SO contributions [30–33]. Using transport measurements in graphene-based nonlocal spin valves (NLSVs), Tombros *et al.* [34] claimed anisotropic spin signals in graphene for in-plane and out-of-plane polarization directions, but their claim was disputed and the result is attributed instead to the magnetoresistance effect in graphene with low carrier density under a strong out-of-plane magnetic field. [35]. Therefore, anisotropic spin relaxation in spin-transport processes is still an open question, and its unambiguous demonstration is desirable for the application of spin current in spintronic devices. Furthermore, polycrystalline metals such as Cu have not been considered for the study of anisotropic spin relaxation because of the lack of SO coupling and crystalline anisotropy. However, spin-orbital effects on the surfaces of the mesoscopic Cu channel could result in anisotropic spin relaxation.

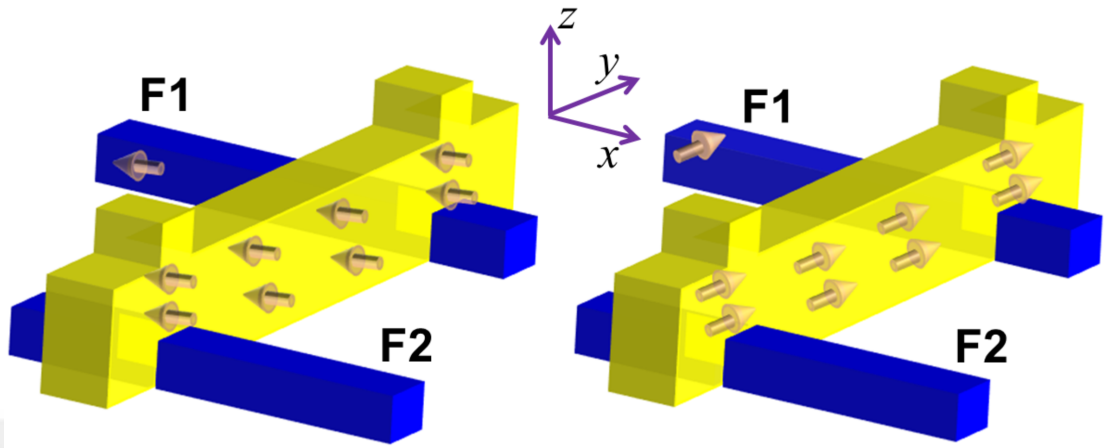

Figure 4.1: Illustration of anisotropic spin transport. On the left NLSV, the spins are aligned in the x direction, which is perpendicular to the direction of spin current. On the right NLSV, the spins are aligned in the y direction, which is parallel to the direction of spin current.

In this work, anisotropic spin relaxation is demonstrated in mesoscopic polycrystalline Cu channels using NLSV [36–46], which is an ideal system for exploring spin relaxation. Figures 4.1(a) and (b) shows schematics of two nonlocal spin valve devices to illustrate anisotropic spin transport. The propagation of a pure spin current along a mesoscopic channel is well separated from the spin injection and detection processes. The exceptional signal-to-noise ratio of the nonlocal method allows a robust investigation of the spin relaxation over a broad range of spin-transport distances. Anisotropic spin relaxation in Cu is identified by exploring the dependence of the anisotropic signals on the spin-transport distance of the Cu channels, and it can be attributed to the SO effects of the Rashba-Sheka-Vasko type [31,32,47] on the surfaces of the Cu channels. The anisotropic differences in spin-relaxation lengths at 10 K are estimated to be as great as 9%. Because of the tunability of the surface SO

effect by an electric field perpendicular to the surface [48,49], our finding introduces the attractive prospect of modulating spin currents via an electrostatic gate, as was originally proposed by Datta and Das for the pioneering spin transistors [9].

4.2 Sample Fabrication and Measurement Setup

The NLSVs are fabricated on silicon substrates covered with 300 nm thick insulating SiN. Photolithography is used to pattern 100 nm thick gold electrical contact pads on the substrate. Subsequently electron beam lithography is used to create suspended shadow masks from two layers of electron-beam resists. The bottom layer PMGI (polydimethylglutarimide) has higher sensitivity to electron-beam dosage than the top layer PMMA (polymethyl methacrylate). While the top layer maintains the fine structures defined by lithography, the bottom layer develops large undercut in the vicinity of the structures. As a result, the top layer structures are suspended above the substrate by the over-developed bottom layer, thereby forming a shadow mask. The evaporation of materials is made from different directions through the shadow mask [38,50–53] in an electron-beam evaporation chamber with a rotatable sample stage and a base pressure better than 5×10^{-8} Torr. Py is first evaporated from a direction that is ~70° from the normal direction of the substrate. Then the AlO_x and Cu are evaporated in the normal direction of the substrate. The evaporation of AlO_x is achieved by direct electron-beam heating of Al_2O_3 pellets in a crucible. The entire evaporation procedure is carried out without breaking vacuum and forms non-local spin valve devices as illustrated in Figure 4.2(b). Therefore, the Py/AlO_x/Cu interface is pristine and the spin injection and detection through the interfaces are efficient. More details of the shadow mask and angle deposition method is discussed in the chapter 3. By using four-probe method on cross-junctions, the resistance-area (*RA*)

product of the Py/AlO_x/Cu is measured to be in the range of 0.01 $\Omega \cdot \mu m^2 < RA < 0.1$ $\Omega \cdot \mu m^2$.

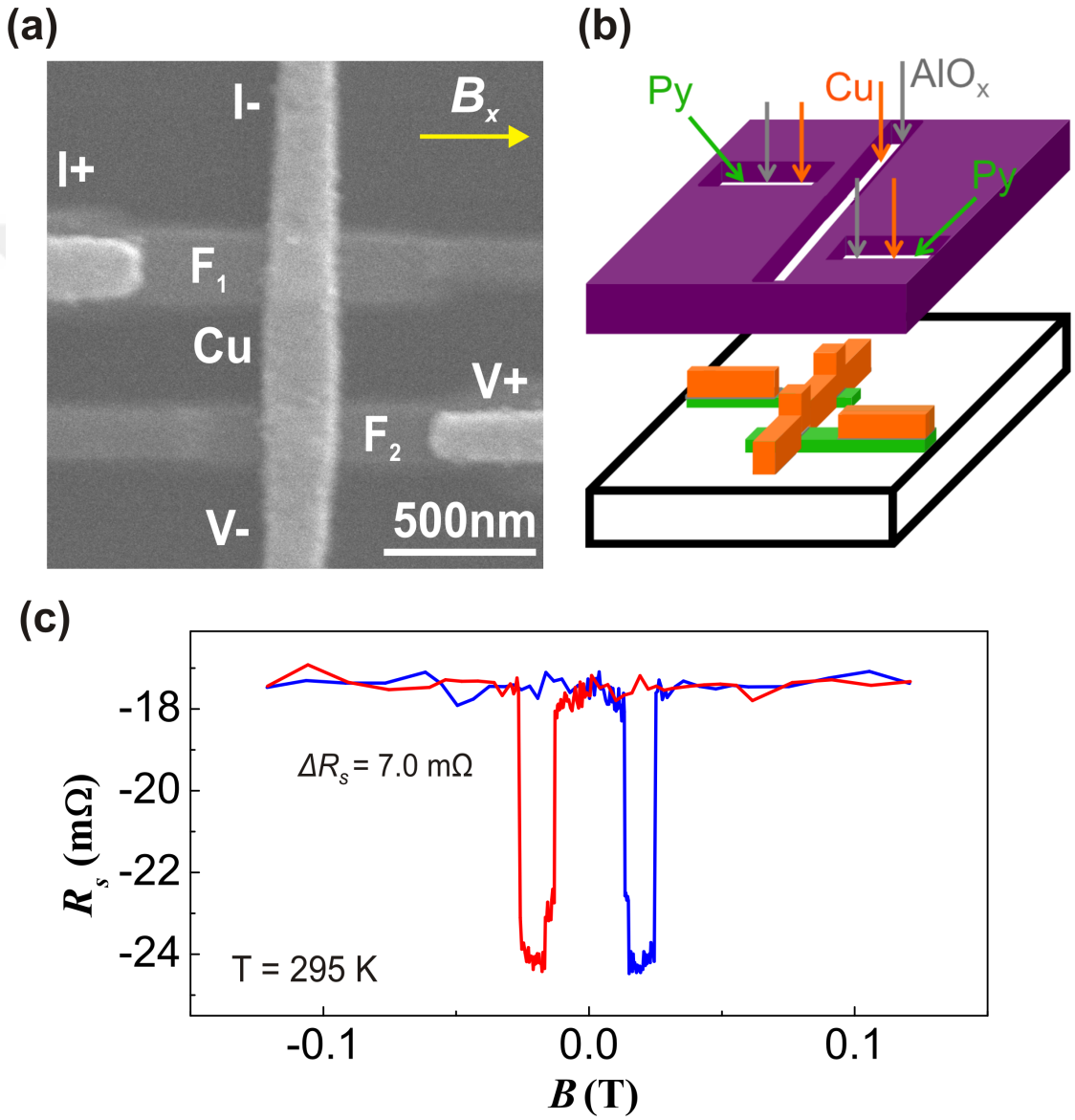

Figure 4.2: (a) SEM image of an NLSV with L=470 nm. (b) Angle evaporation of NLSV structure through a mesescopic shadow mask. Adapted from [53]. (c) The R_s versus B curve at 295 K.

An alternating current (*a.c.*) of I_e = 0.1 mA at low frequency (< 1000 Hz) is used as the charge injection current for the NLSVs. The *a.c.* nonlocal voltage V_{nl} is detected by a lock-in detector. The initial evidence of anisotropic spin signals, shown in Figures 4.5 and 4.6 is obtained at 295 K with a rotatable sample stage in an electromagnet. The more systematic measurements of anisotropic signals on substrates A and B are carried out at 10 K in a Lakeshore variable temperature probe station (LakesShore EMPX-HF) with an electromagnet. A permanent magnet is mounted on the sample stage to provide a 0.03-T bias magnetic field that is always in the +*x* direction of the sample coordinate. A variable applied magnetic field is provided by the electromagnet. The sample stage can be orientated so that the applied field can be in either the *x* direction or the *y* direction of the sample coordinate.

4.3 Experiments

Figure 4.2(a) shows a scanning electron microscope (SEM) image of an NLSV that consists of a spin injector (F_1) and a spin detector (F_2) orientated in the *x* direction and a Cu channel in the *y* direction of the sample coordinate. F_1 and F_2 are made of permalloy (Py), an alloy of NiFe, and have widths of ~150 nm and ~130 nm and thicknesses of 18 nm and 12 nm, respectively. The widths of the Cu channel are between 160 and 210 nm, and the center-to-center distance *L* between F_1 and F_2 ranges from 400 to 1050 nm. Two thicknesses of Cu, 200 nm and 110 nm, are used. A layer of 3 nm AlO_x is placed at the interfaces between Py and Cu for efficient spin injection and detection [54]. The precise geometries of all the NLSVs are measured by SEM after transport measurements for data analysis.

A charge current I_e between F_1 (I+) and the upper end of the Cu channel (I–) injects a spin accumulation into the channel. The gradient of the spin accumulation

drives a pure spin current along the channel in the –*y* direction. A nonlocal voltage V_{nl} is measured between F_2 (V+) and the lower end of the Cu channel (V–). The ratio of nonlocal voltage to the injected current, the nonlocal signal $R_s = V_{nl}/I_e$, is recorded as a function of applied magnetic field B. Figure 4.2(c) presents R_s versus *B* curve at 295 K, for the device shown in Figure 4.2(a).

The conventional way to measure a nonlocal spin valve is to sweep the applied magnetic field parallel to the Py stripes (F_1 and F_2), which is the magnetic easy axis of the F_1 and F_2 electrodes. In this thesis "*x* direction" is defined as perpendicular to the Cu channel, and "*y* direction" as parallel to Cu channel. As the magnetic field is swept, the magnetic spins of F_1 and F_2 electrodes align parallel in the *x* direction at a higher field and result in high R_s values. When the magnetic field is gradually decreased to zero and reversed to other direction, one of the F_1 and F_2 electrodes switches magnetization first due to different coercivity of electrodes. This gives rise to an antiparallel state between F_1 and F_2 electrodes and result in lower R_s values. As the field is further decreased, the other electrode also switches and the electrodes go back to the parallel state again. The difference of the R_s values is defined as the spin signal for x-direction spins, which is $\Delta R_s = 7.0\ m\Omega$ at 295 K, as shown in Figure 4.2(c).

The spin signal can be described by: [55]

$$\Delta R_s = \frac{P_1 P_2 \rho \lambda}{A_N} e^{\frac{-L}{\lambda}} \tag{4.1}$$

where P_1 and P_2 are the effective spin polarizations of F_1 and F_2, respectively, ρ is the resistivity of Cu, λ is the Cu spin-relaxation length, A_N is the cross-sectional area of the Cu channel and L is the center to center distance between F_1 and F_2 electrodes. Eq. (4.1) is valid for NLSVs only with resistive tunnel barriers sandwiched between the

NM channel and FM electrodes, F_1 and F_2. This is a special case of more general formula, which is derived for ohmic interfaces and low-resistance barriers [37]. However, the equation (4.1) is still a good approximation if the spin resistance of the Cu (1~ Ω), is comparable or lower than the junction resistance [56], where P_1 and P_2 is defined as effective spin polarizations.

It is a typical method to obtain λ and P by fitting the measured nonlocal spin signals ΔR_s as a function of distance L between the F_1 and F_2 electrodes using the

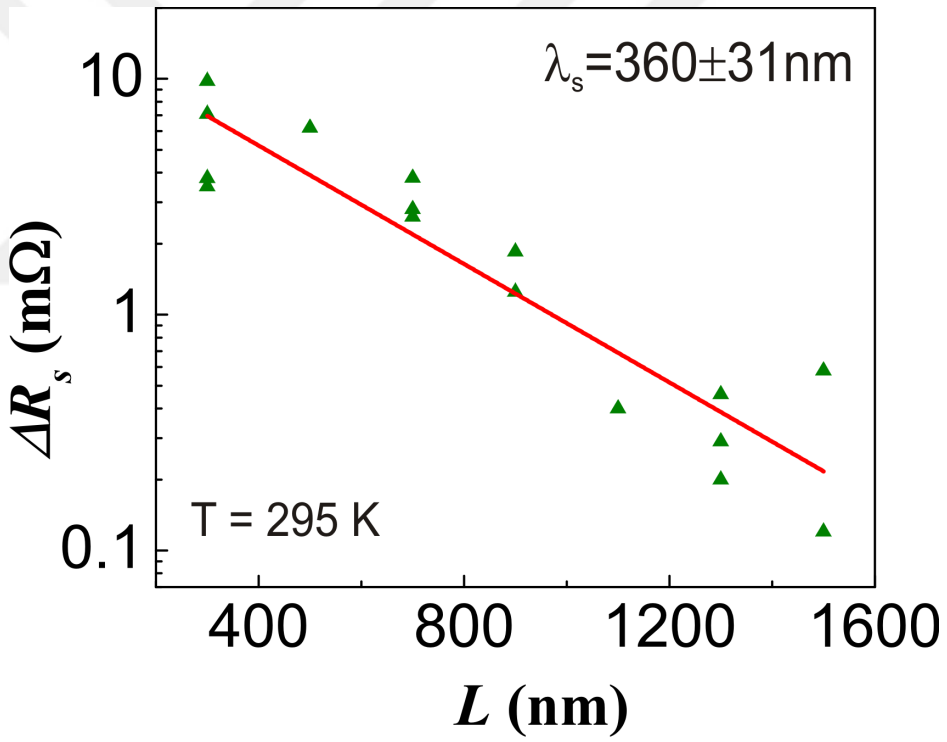

Figure 4.3: Spin signal ΔR_s as a function of channel length L at RT. Solid red line shows the fitting by the equation 4.1.

equation (4.1) above. Figure 4.3 shows ΔR_s versus L curve at 295 K. The all NLSV devices used for this plot were fabricated under the same nominal conditions. Spin-relaxation lengths in Cu channels are estimated as $\lambda = 360$ nm at 295 K by fitting the equation (4.1).

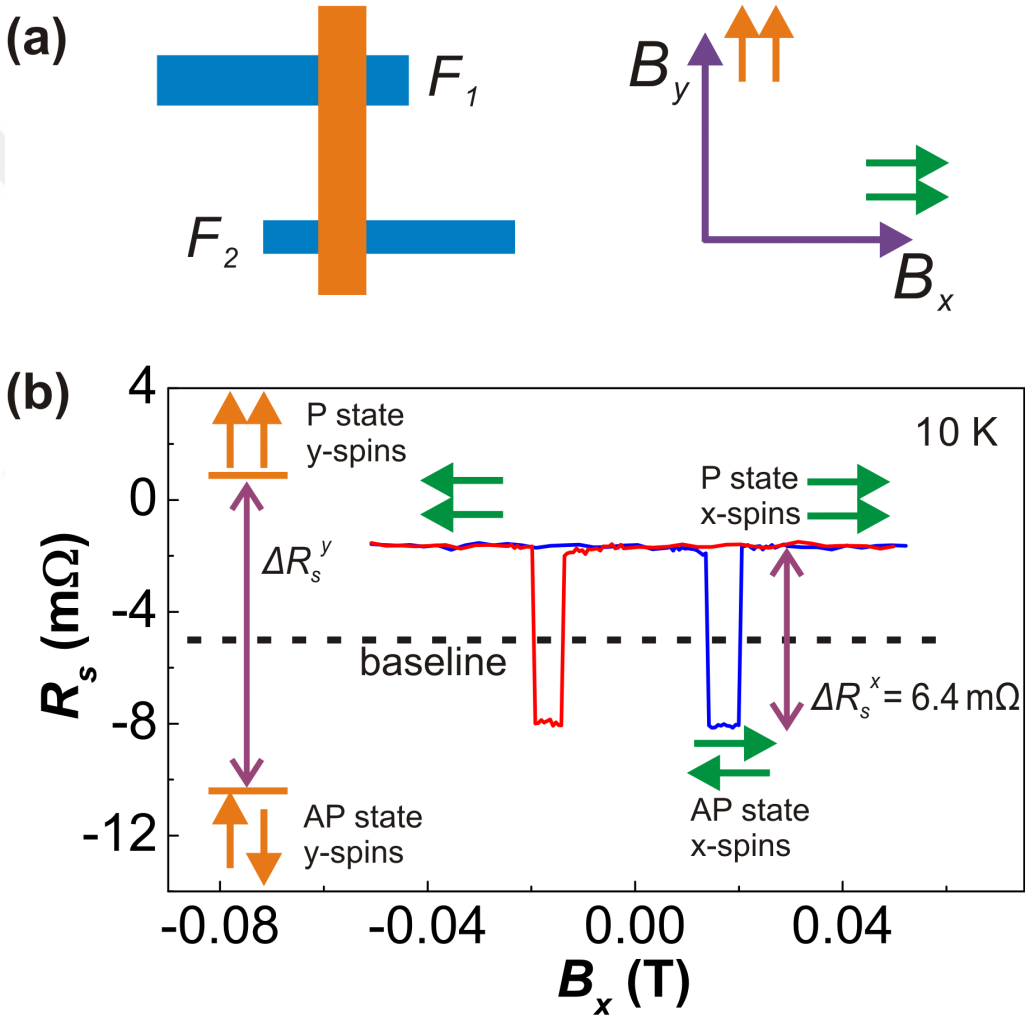

Figure 4.4: (a) Cartoon illustration of x direction and y direction magnetic fields applied to an NLSV (on the left). (b) The R_s versus B_x curve for a typical NLSV at 10 K, and illustration of P and AP states for x spins and y spins. The R_s values of the P state and antiparallel state are symmetrical to the baseline. Copyright 2017 by the American Physical Society.

4.3.1 Anisotropic Spin Signals

The anisotropic spin relaxations in the Cu channel of NLSVs are experimentally proved in this section. The spin signals for NLSVs in which the magnetic spins are aligned parallel to Cu channels (*y*-direction) are lower than the spin signals in which the spins are aligned perpendicular to Cu channels (*x*-direction) [Fig. 4.1(a) and (b)].

Figure 4.4(b) shows the nonlocal signal R_s as a function of applied magnetic field in the x direction for an NLSV and illustrates the parallel and antiparallel states for the signals of *x* spins and *y* spins. The R_s alternates between a high-value state, corresponding to parallel (P) spins of F_1 and F_2, and a low-value antiparallel (AP) state, yielding a spin signal of $\Delta R_S^x = 6.4\ m\Omega$ for the x spins. The average R_s of the P and AP states is the "baseline" and corresponds to a null spin accumulation in the Cu channel. The P state R_s is higher than the baseline by $\Delta R_S^x/2$, and the AP state R_s is lower by the same amount.

When the magnetic field is applied in the *y* direction to polarize the spins of F_1 and F_2, in principle the spin signals for *y* spins can also be detected. The P and AP states for the *y* spins, if both can be reached, should also be symmetrical about the baseline, and the difference between two states is the spin signal ΔR_S^y for *y* spins, as illustrated in Figure 4.4(b). If $\Delta R_S^y \neq \Delta R_S^x$, the spin signals are anisotropic, and we can define the anisotropic signal $(\Delta R_S^y - \Delta R_S^x)$ and the percentage anisotropic signal $(\Delta R_S^y - \Delta R_S^x)/\Delta R_S^x$. When $\Delta R_S^y > \Delta R_S^x$, the P state of the *y* spins is higher than that of the *x* spins by $(\Delta R_S^y - \Delta R_S^x)/2$. In this work, we measure this quantity by directly comparing the P states of *x* spins and *y* spins. Note that it is often not a straightforward matter to access the AP state of *y* spins, because the easy axis of F_1 and F_2 lies in the *x*

direction. The baselines for *x* spins and *y* spins should be identical for the same NLSV, at a fixed temperature, and wired in the same circuit.

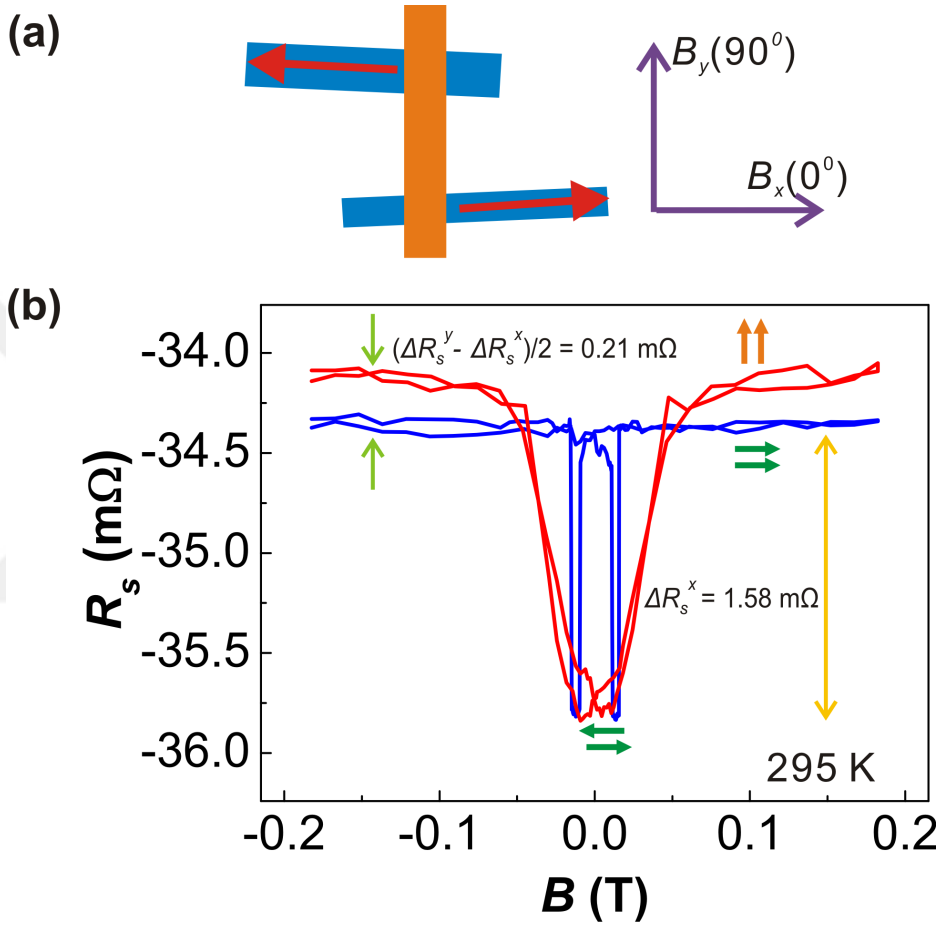

Figure 4.5: (a) The F_1 and F_2 of the NLSV are designed to make small but opposite angles (±3°) with the x direction. (b) The R_s versus B curves for this NLSV at 295 K, with field applied along the *x* direction (blue) and the *y* direction (red). Copyright 2017 by the American Physical Society.

4.3.2 Anisotropic Signal Measurements by Sweeping Magnetic Field

The first evidence of anisotropic signals is obtained at 295 K with a specially designed non local spin valve, in which F_1 and F_2 have opposite small angles (±3°)

with respect to the +x axis, as shown in Figure 4.5(a). With this special design, F_1 and F_2 electrodes can reach a well-defined antiparallel state as the field is scanned in the y direction. Figure 4.5(b) shows the measured R_s as a function of the applied magnetic fields B_y in the y direction (red curve) and B_x in the x direction (blue curve). Obviously the red curve shows greater overall R_s variation than the x-spin signal $\Delta R_s^x = 1.58\ m\Omega$ of the blue curve. When a high magnetic field, $B_y = 0.2$ T, is applied along the +y direction, the magnetic spins of F_1 and F_2 electrodes align parallel to the +y direction, which is the hard magnetic axis. As the field B_y is reduced, the spins gradually rotate toward the easy axis (±x direction). Because of the opposite angle configuration, the F_1 and F_2 spins snap into the –x and +x directions, respectively, when $B_y = 0$, reaching an x-spin AP state. So, the lowest values of both the red and blue curves correspond to the same AP state for x-spins. The highest values of the two curves correspond to the P states for the y and x spins, and the difference gives anisotropic spin signal, $(\Delta R_s^y - \Delta R_s^x)/2 = 0.21\ m\Omega$. This amounts to a percentage increase of the signal of $(\Delta R_s^y - \Delta R_s^x)/\Delta R_s^x = 26\%$ between the y spins and x spins.

4.3.3 Anisotropic signal measurements by Rotating Sample under the Fixed Magnetic Field

It is obvious from Figure 4.5(b) that a field of 0.2 T is sufficient to align the spins into the P state along the hard axis (±y direction). To further confirm the anisotropic signal, we rotate the same NLSV in a 0.2 T magnetic field between 0° and 90° periodically to alternate the field, and thereby the aligned spins, between the x and y directions of the sample coordinate, respectively as it is seen in Figure 4.6(a). A periodic R_s change of 0.17 mΩ is observed, as shown in Figure 4.6(b), with the P state of the y spins (90°) higher than the P state of x spins (0°), confirming the anisotropic

signal. A small baseline change of –0.03 mΩ, shown in Figure 4.6(c), induced by subtle changes of AC coupling in the measurement circuits while the sample rotates, has to be subtracted to obtain an accurate anisotropic signal. The baseline changes of

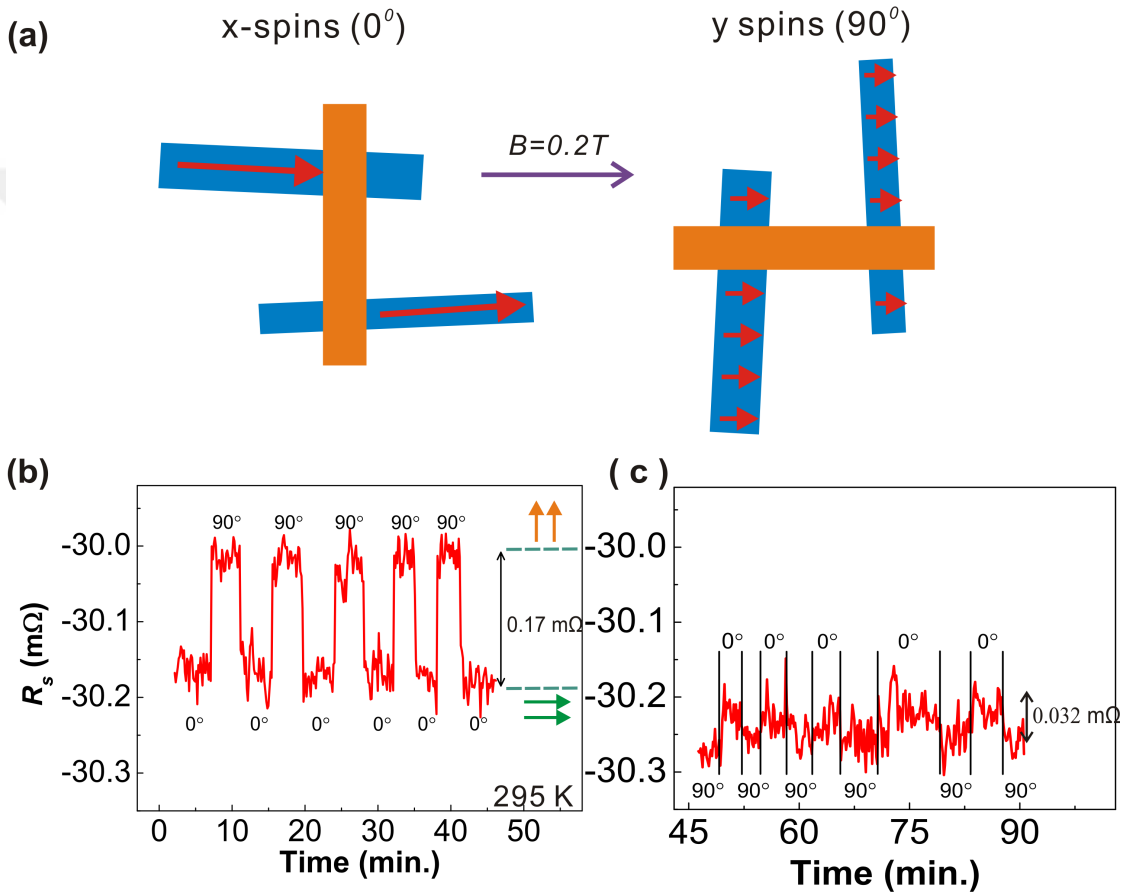

Figure 4.6: (a) Illustrates the rotation of the NLSV relative to the fixed magnetic field, the spins alternate between the +*x* and +*y* directions periodically. (b) The R_s versus time plot at 295 K while the NLSV (the same as in Fig. 4.5) is rotated between 0° and 90° under a 0.2-T magnetic field. Copyright 2017 by the American Physical Society. (c) The R_s versus time plot while the same NLSV is rotated between 0° and 90° under zero magnetic field.

R_s values and implications are going to be discussed in detail in the next section. The calibrated anisotropic signal value, $(\Delta R_s^y - \Delta R_s^x)/2 = [0.17 - (0.03)]\, m\Omega =$ 0.20 mΩ, is consistent with the 0.21 mΩ shown in Figure 4.5(b).

4.3.3.1 Baseline of the R_s versus B Curves and Implications on Measurements

Figure 4.4(b) illustrates that the baseline is the average R_s value for the parallel (P) and antiparallel (AP) states. The baseline arises from a background charge voltage that corresponds to a null spin accumulation in the NLSV. For strictly one-dimensional NLSVs, the baseline value should simply be zero because there is no charge voltage between the F_2 and the Cu channel. However, for realistic three-dimensional NLSV devices, the baseline R_s value is not exactly zero because of the nontrivial current distribution in the mesoscopic structure [57,58].

In addition, the nonlocal measurements are carried out using alternating current (AC) lock-in method, and any variation in AC coupling affects the baseline. For example, a change of AC frequency would alter the effective reactance (capacitance and inductance) values of the measurement circuits and thereby alter the baseline. Measurements carried out in separate circuits for the same NLSV would have different baselines, because the effective reactance values are different between circuits. Similarly, subtle changes in wiring configurations of the measurement circuits could result in variations of baseline values as well.

In this work, the anisotropic signal $(\Delta R_s^y - \Delta R_s^x)/2$ is measured by detecting the difference between the P states for *y* spins and *x* spins, as illustrated in Figures 4.5 and 4.6. The underlying assumption is that the baseline for the NLSV remains unchanged when the spin states are altered between *x* and *y* directions. For an accurate

detection of $(\Delta R_s^y - \Delta R_s^x)/2$, one has to either ensure a truly intact baseline during measurement, or compensate for any change of baseline.

The two R_s versus B curves in Figure 4.5(b) are measured in separate circuits and therefore the baseline values are not guaranteed to be the same. However, the lowest R_s values for both curves are associated with AP state for x spins and it can be used as a common reference point for comparison, as explained before. We shift the two curves on the vertical scale so that the lowest points of both curves are aligned at the same R_s value. Then the anisotropic signal $(\Delta R_s^y - \Delta R_s^x)/2$ can be obtained by comparing the highest values of the two curves in Figure 4.5(b).

For the measurement in Figure 4.6(b), as the sample stage is rotated inside a magnetic field, the NLSV remains in the same measurement circuit. A clear periodic signal change is observed and the apparent value for $(\Delta R_s^y - \Delta R_s^x)/2$ is 0.17 mΩ, with the R_s of 90° (y spins) being higher than that of 0° (x spins). However, the rotation of the sample stage may cause subtle changes of wiring configuration in the circuit thereby changing the R_s baseline value. To compensate for this, the rotational measurement is carried out in zero magnetic field and a small periodic signal of – 0.03 mΩ is observed as shown in Figure 4.6(c). The negative sign indicates that the R_s value of 0° is higher than that of 90°, opposite to the situation in Figure 4.6(b). This observed periodic signal must come from the baseline change associated with the rotation, because the spins in the NLSV do not change relative to the sample coordinate as the sample rotates in the zero magnetic field. Therefore, this signal of – 0.03 mΩ should be subtracted from the apparent signal of 0.17 mΩ in Figure 4.6(b), and the adjusted anisotropic signal is $(\Delta R_s^y - \Delta R_s^x)/2$ = 0.17 mΩ – (–0.03 mΩ) = 0.20 mΩ.

4.3.4 Anisotropic Signal Measurements under the Rotational Magnetic Field

It is challenging to access a stable AP state for *y* spins, given that the easy axis is in the *x* direction. As it is done in the previous section, the P state of the *y* spins can be reached by applying a *y*-direction magnetic field B_y to the NLSV, and its R_s value can be compared to that of the P state for *x* spin to determine the $(\Delta R_s^y - \Delta R_s^x)/2$. Rotating field can be achieved in two ways, rotating the sample stage under the fixed magnetic field, as we did in the previous section, or rotating the magnetic field as the sample stage stays stationary. In the first case, after rotation of the sample stage, the four electrical contacts (probes) to the device would have to be reestablished, which induces a subtle change in the baseline R_s and disturbs the integrity of the measurement. For a reliable measurement of $(\Delta R_s^y - \Delta R_s^x)/2$, we rotate the magnetic field between the *x* direction and *y* direction to keep the NLSV and its measurement circuit intact. This requires the sample stage to stay stationary during the $(\Delta R_s^y - \Delta R_s^x)/2$ measurements. Therefore, the baseline should indeed remain unchanged during the measurement and the detected anisotropic signal, $(\Delta R_s^y - \Delta R_s^x)/2$, is accurate.

Systematic measurements of anisotropic signals for NLSVs of various channel lengths *L* are carried out in a probe station at 10 K. These NLSVs are fabricated on two substrates (samples), A and B, with Cu thicknesses of 200 nm and 110 nm, respectively. Both substrates are Si covered with 300 nm SiN. NLSVs on the same substrate undergo identical processing procedures. We alternate the magnetic field between the *x* and *y* directions to access the P states of the *x*-spins and *y*-spins, respectively. The rotating magnetic field is realized by a bias field B_{bias} ~0.03 T in the *x* direction from a permanent magnet and a variable applied field B_y in the *y* direction from an electromagnet, as shown in Figure 4.7(a). The purpose of the B_{bias} is to align

F_1 and F_2 into a good *x*-spin P state under zero applied field. To verify this, the field B_x is applied in the same direction (+*x*) as the B_{bias}, and the measured R_s versus B_x curve on a typical NLSV is shown in Figure 4.7(b). The bias field shifts the curve along the

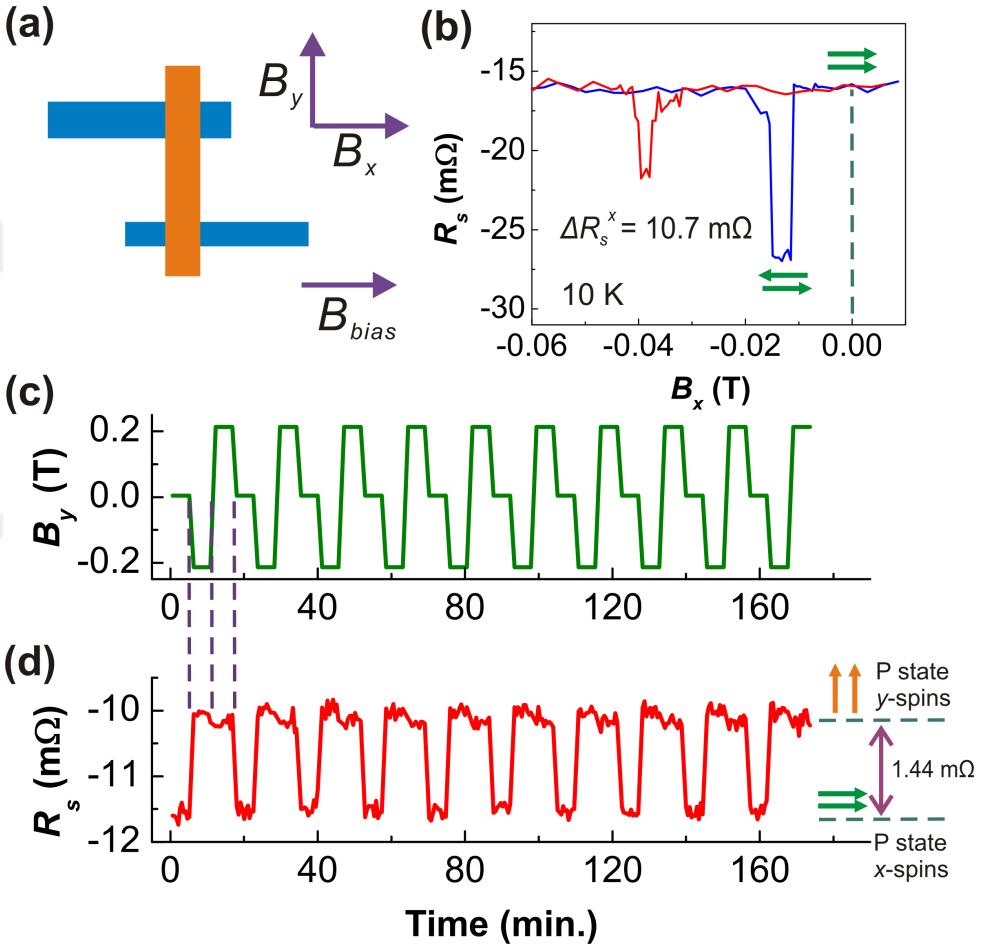

Figure 4.7: (a) Illustration of a fixed bias field B_{bias} in the x direction and an applied field that can be oriented either in the x direction or in the y direction. (b) The R_s versus B_x curve with applied field in the x direction in the presence of the bias field. Due to bias field, the spins are aligned well into a P state even at $B_x = 0$. (c) and (d) are measurements with applied field B_y in the y direction while bias field is still along x direction. (c) The applied field B_y as a function of time (d) The measured signal R_s as a function of time. The measurements in this figure are carried out at 10 K. Copyright 2017 by the American Physical Society.

B_x axis, and the R_s value at B_x = 0 T clearly indicates a good *x*-spin P state. The difference of ΔR_s (the magnitudes of the dips) between the red and blue curves is attributed to the proximity of the F_1 and F_2 switching fields and the resultant mediocre AP state while the field ramps downward. The signal of the upward branch is taken as the full spin signal for *x* spins: ΔR_s^x = 10.7 mΩ.

Figure 4.7(c) illustrates that B_y alternates periodically between 0 T, −0.2 T, and +0.2 T while B_{bias} remains in the *x* direction. As a result, the aligned spins alternate between the +*x*, −*y*, and +*y* directions, respectively. Because the applied fields B_y = ±0.2 T are much larger than the 0.03-T bias field, they are sufficient to align spins into the ±*y* directions. Figure 4.7(d) illustrates the measured R_s as a function of time. When B_y changes from 0 to –0.2 T, R_s increases abruptly by ~1.5 mΩ. When B_y changes from –0.2 T to +0.2 T, R_s stays at almost the same value. When B_y changes from +0.2 T to 0 T, R_s decreases by ~1.5 mΩ. As the field cycles go on, the same pattern is consistently reproduced and again provides clear evidence for an anisotropic signal. We take the average R_s values at ±0.2 T as the P state of the *y* spins and the R_s value at 0 T as the P state of the *x* spins. We extract the anisotropic signal, $(\Delta R_s^y - \Delta R_s^x)/2$ = 1.44 mΩ, by averaging the difference between two states over many cycles. The percentage anisotropic signal is $(\Delta R_s^y - \Delta R_s^x)/\Delta R_s^x$ = 26.8%.

Presence of anisotropic spin transport in nonlocal spin valves has been demonstrated at both 10 K and 295 K by the three different measurement techniques described above. Similar anisotropic signals have been observed from many NLSV devices. In the next section, the systematic trend of percentage anisotropic change $(\Delta R_s^y - \Delta R_s^x)/\Delta R_s^x$ as a function of Cu channel length *L* or the normalized channel length L/λ_x will be analyzed from many devices fabricated on two substrates.

4.4 Origin of Anisotropic Effects

The next important question is the origin of the anisotropic signal. Does it come from spin relaxation in the nonmagnetic Cu channel or spin polarization from the magnetic injector or detector? The quantitative description of the spin signals is useful for identifying the origin of the anisotropy. The spin signal of NLSVs with oxide interfaces is well described [38,40,54,55] by equation (4.1), which is $\Delta R_s = (P_1 P_2 \rho\lambda/A)e^{-L/\lambda}$, where P_1 and P_2 are the effective spin polarizations of F_1 and F_2, ρ is the resistivity of Cu, λ is the Cu spin-relaxation length, and A is the cross-sectional area of Cu. In NLSV studies [40,44–46] it is customary to assume that $P_1 = P_2 = P$ when F_1 and F_2 are made of same material (Py) and have similar dimensions.

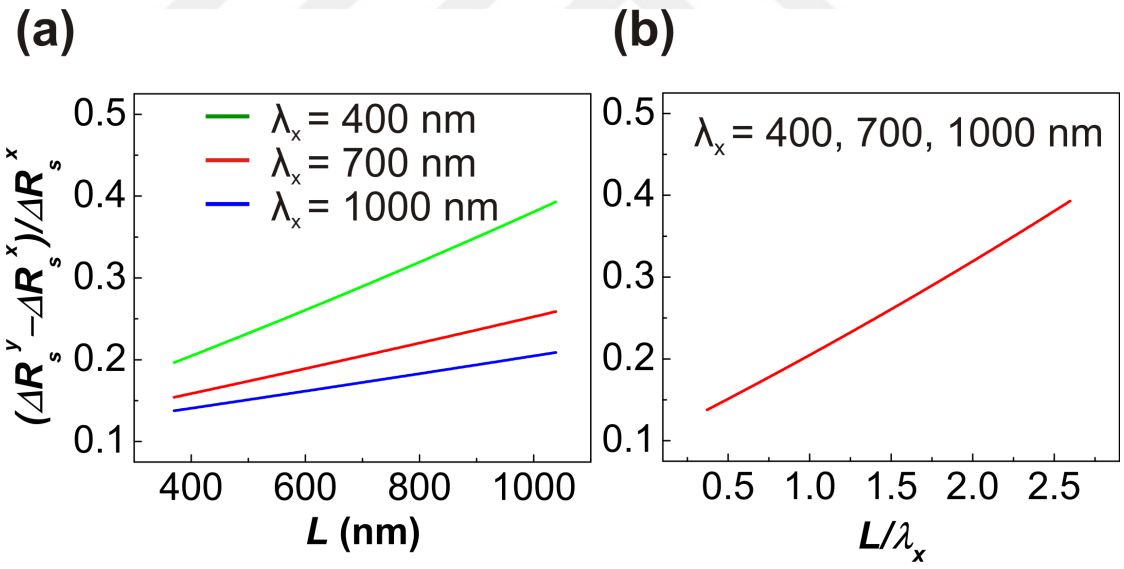

Figure 4.8: (a) Calculated percentage signal change $(\Delta R_s^y - \Delta R_s^x)/\Delta R_s^x$ as a function of L for various values of λ_x. The anisotropic change of λ is assumed to be $(\lambda_y - \lambda_x)/\lambda_x = 10\%$ (b) The same results as in (a) are plotted as a function of normalized channel length L/λ_x. Three curves collapse onto a single curve. Copyright 2017 by the American Physical Society.

Because A and ρ are spin-independent quantities, the observed anisotropic spin signals should originate from either the effective spin polarizations P of the ferromagnetic electrodes or spin-relaxation length λ of the Cu channel. F_1 and F_2 are polycrystalline, and the injection current is nearly perpendicular to the interface. Therefore, there is no reason for an anisotropic P between the x spins and y spins, and our results suggest an anisotropic λ. Moreover, if the P_x for x spins and P_y for y spins differs by a fixed percentage $(P_y - P_x)/P_x$, the percentage anisotropic signal $(\Delta R_s^y - \Delta R_s^x)/\Delta R_s^x$ should remain a constant and be independent of channel length L, according to Eq. (4.1). However, if the λ_x for x spins and the λ_y for y spins differ by a fixed percentage $(\lambda_y - \lambda_x)/\lambda_x$ due to the anisotropic spin relaxation, $(\Delta R_s^y - \Delta R_s^x)/\Delta R_s^x$ should increase as a function of L.

Figure 4.8(a) shows the calculated $(\Delta R_s^y - \Delta R_s^x)/\Delta R_s^x$ as a function of L from Eq. (4.1), assuming $(\lambda_y - \lambda_x)/\lambda_x$ = 10% for several λ_x values. The calculated $(\Delta R_s^y - \Delta R_s^x)/\Delta R_s^x$ increases monotonically with L. In Figure 4.8(b), a normalized channel length L/λ_x is used as the horizontal axis. All three curves in Figure 4.8(a) collapse to a single curve in Figure 4.8(b), giving a more universal relationship that is immune to variation in λ_x. The experimental values of $(\Delta R_s^y - \Delta R_s^x)/\Delta R_s^x$ for NLSVs on substrates A and B are plotted as a function of L in Figures 4.9(a) and (c), respectively. The highest value of $(\Delta R_s^y - \Delta R_s^x)/\Delta R_s^x$ at a particular L increases as a function L for both substrates. For substrate B, the highest percentage reaches ~46% for L = 1050 nm.

Note that the simple monotonic increase predicted in Figures 4.8(a) and (b) is not obvious because of data dispersion, which can be attributed to variations in λ

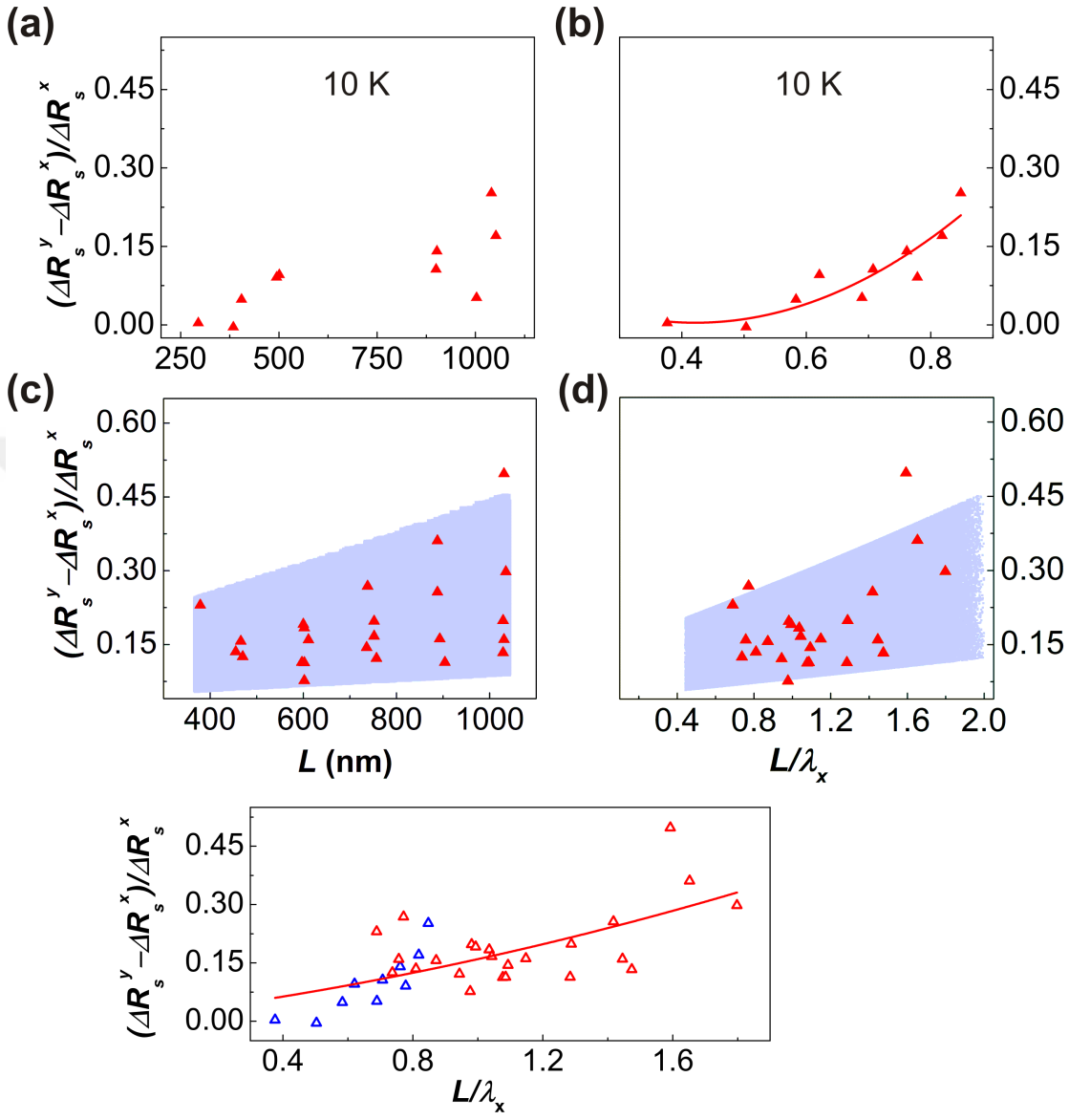

Figure 4.9: The percentage anisotropic signal, $(\Delta R_s^y - \Delta R_s^x)/\Delta R_s^x$, as a function of (a) L and (b) L/λ_x at 10 K for NLSVs on substrate A. The percentage anisotropic signal, $(\Delta R_s^y - \Delta R_s^x)/\Delta R_s^x$, as a function of (c) L and (d) L/λ_x at 10 K for NLSVs on substrate B. The shaded areas in (c) and (d) are calculation by randomized parameters in the range: $\lambda_x = 670 \pm 180$ nm and $(\lambda_y - \lambda_x)/\lambda_x = (9\pm5)\%$. (e) The plot of $(\Delta R_s^y - \Delta R_s^x)/\Delta R_s^x$ versus L/λ_x for NLSVs on both substrates A (blue symbols) B (red symbols). The solid line in (b) and (e) are guidance to eyes. (a-d) Copyright 2017 by the American Physical Society.

between NLSVs in spite of their being fabricated under identical conditions. The λ_x versus ρ graphs for Cu are plotted in Figures 4.10(a) and (b) for NLSVs on substrates A and B, respectively. We measure ρ for each NLSV by sending a current through the Cu and measuring a voltage between F_1 and F_2. We calculate λ_x from the ΔR_S^x and ρ of this NLSV using Eq. (4.1) and assuming $P = 20\%$, which is justified by previous

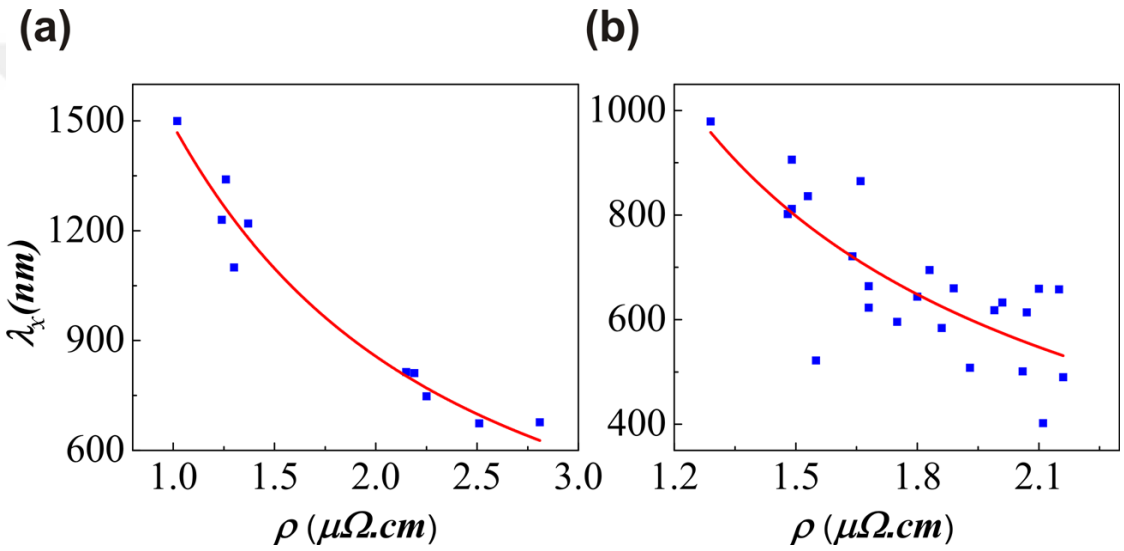

Figure 4.10: (a) The spin-diffusion length λ_x versus resistivity ρ for substrate A at 10 K and the fit (solid line) by Elliott-Yafet model (b) The λ_x versus ρ plot and fit (solid line) for substrate B at 10 K. The λ_x value on the fitted curve is used to determine normalized distance L/λ_x in Figure 4.9. Copyright 2017 by the American Physical Society.

measurements [50,54,59]. The data are fitted by $\lambda_x = \beta/\rho$, which is implied by the Elliot-Yafet model [24,25,54]. Here β is the fitting parameter and is related to the spin-relaxation rate in the Cu. The fitted λ_x corresponding to the measured ρ is used to calculate the normalized channel length (L/λ_x) for each NLSV. The $(\Delta R_S^y - \Delta R_S^x)/\Delta R_S^x$ is plotted as a function of L/λ_x for the substrates A and B in

Figures 4.9(b) and (d), respectively, and the increasing trends are clear. Furthermore, the all data for A and B can be combined to generate a single plot, shown in Figure 4.9(e), yielding a clear increase of $(\Delta R_S^y - \Delta R_S^x)/\Delta R_S^x$ versus L/λ_x that is qualitatively consistent with the calculation in Figures 4.8(a) and (b). Therefore, we conclude that the spin relaxation is anisotropic in the Cu channels and causes the observed anisotropic spin signals.

In Figure 4.9(d), there is still substantial data dispersion, which can be explained by variations in $(\lambda_y - \lambda_x)/\lambda_x$ in addition to the variations in λ_x. Using randomized parameters in the range of λ_x = 670 ± 180 nm and $(\lambda_y - \lambda_x)/\lambda_x$ = (9 ± 5)% for substrate B, we calculate the $(\Delta R_S^y - \Delta R_S^x)/\Delta R_S^x$ versus L/λ_x, which is shown as the shaded region in Figure 4.9(d). The dispersion of the experimental data is qualitatively reproduced. We also plotted the calculated $(\Delta R_S^y - \Delta R_S^x)/\Delta R_S^x$ as a function of L, which is shown as the shaded region in Figure 4.9(c). Again, the calculation shows the dispersion of experimental data and similarly for a particular L the highest $(\Delta R_S^y - \Delta R_S^x)/\Delta R_S^x$ increases as a function of L.

Overall, a systematic increase of $(\Delta R_S^y - \Delta R_S^x)/\Delta R_S^x$ as a function of L/λ_x is observed in experimental data. We therefore conclude that the anisotropic signal originates from the anisotropic spin relaxation in the Cu channels instead of the anisotropic spin polarization of the F_1 and F_2 electrodes. The average values of $(\Delta R_S^y - \Delta R_S^x)/\Delta R_S^x$ are lower for substrate A than for substrate B, because the average λ_x is longer for substrate A and the average normalized channel length L/λ_x is lower.

We have provided evidence that anisotropic signal is a direct result of anisotropic difference between the Cu spin-relaxation lengths λ_x for x spins and the λ_y for y spins. For each NLSV, the values of λ_y can be estimated from the spin signals of

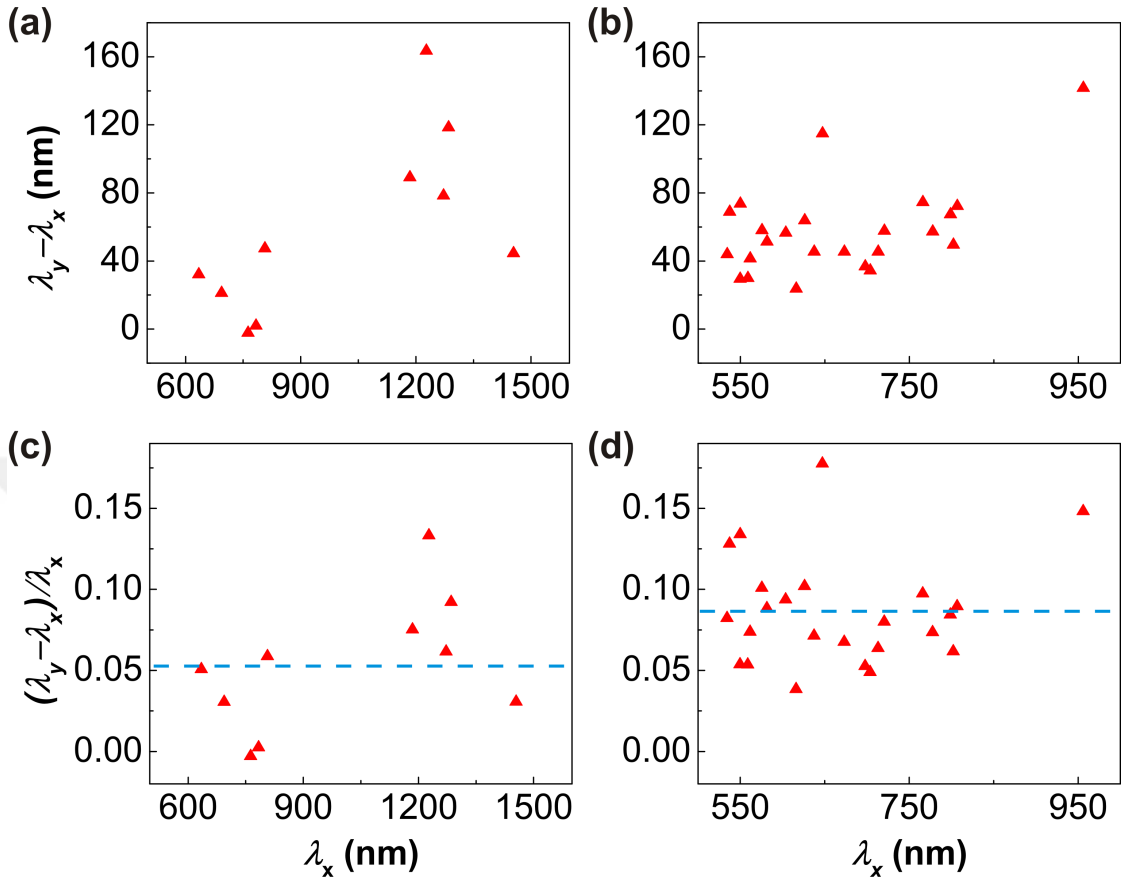

Figure 4.11: The estimated anisotropic change in spin diffusion length ($\lambda_y - \lambda_x$) at 10 K is plotted as a function of estimated λ_x for NLSVs on (a) substrate A and (b) substrate B. The percentage change ($\lambda_y - \lambda_x$) / λ_x versus λ_x at 10K for (c) substrate A and (d) substrate B. The dashed lines indicate average values.

y-spin ΔR_s^y in a way similar to how λ_x is obtained from ΔR_s^x. More specifically we assume $P = 20\%$ and calculate λ_y from Eq. (4.1) using measured ρ, L, and A for that NLSV. The obtained anisotropic difference of spin-relaxation length $(\lambda_y - \lambda_x)$ is plotted as a function of the λ_x for NLSVs on substrates A and B, as shown in Figures 4.11(a) and (b), respectively. The percentage change $(\lambda_y - \lambda_x)/\lambda_x$ is shown in Figures 4.11(c) and (d) as a function of λ_x for substrates A and B, respectively. The

average value is $(\lambda_y - \lambda_x)/\lambda_x$ = (5.3 ± 4.1) % for substrate A and $(\lambda_y - \lambda_x)/\lambda_x$ = (8.6 ± 3.3)% for substrate B.

The magnetoresistance effect that can mimic anisotropic spin signals in graphene [34,35] can be ruled out in this study. We use a small field (≤ 0.2 T) to rotate spins in the substrate plane. In Figure 4.5(b), the anisotropic signal difference between the red and blue curves is already quite obvious even at 0.05 T and saturates at higher fields. Furthermore, the metallic Cu channel has high carrier density and is not easily influenced by the applied magnetic field.

4.5 Discussion and Theory

All the relevant theories link anisotropic spin relaxation to various spin-orbit couplings [19–23], which should account for the observed anisotropic spin relaxation in Cu channels as well. Furthermore, we can rule out the contribution of bulk SO to the observed anisotropic spin relaxation by performing *ab initio* transport calculation of spin relaxation in bulk Cu. The calculation has been carried out by our collaborator Dr. Yuan Zhe of Beijing Normal University.

A bilayer along face-centered cubic (111) crystal plane is constructed. It consists of 10-nm-thick Py and 100-nm-thick Cu, both of which are made diffusive by imposing the frozen thermal lattice disorder [60]. The disorder is implemented in a 5×5 supercell in the lateral directions with periodic boundary condition. The electronic structure of the bilayer is calculated self-consistently based upon the local density approximation of density functional theory. The lattice constant of Cu, namely 3.614 Å, is used for the whole system. The potentials, charge and spin densities of Fe and Ni atomic spheres in Py are obtained within the coherent potential approximation [61] implemented with the minimal basis of tight-binding linear muffin-tin orbitals [62].

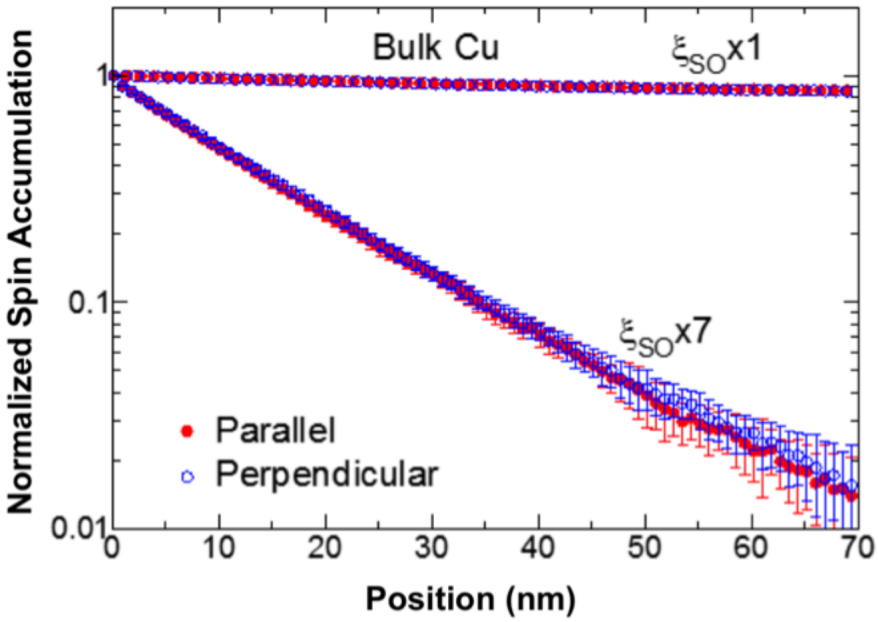

Figure 4.12: Calculated spin accumulation in bulk Cu as a function of distance from the Py/Cu interface. While the upper data are obtained using the real SO strength of bulk Cu, the lower ones are calculated with the SO strength artificially increased by a factor of 7. In both cases, the spins parallel to the spin-current direction (*y* spins, red symbols) are the same as the spins perpendicular to it (*x* spins, blue symbols), indicating the bulk SO interaction does not introduce the anisotropic spin relaxation. Copyright 2017 by the American Physical Society.

The magnetic moments in the Fe and Ni atomic spheres are 2.71 and 0.64 Bohr magneton, respectively.

Using semi-infinite ballistic Cu electrodes in both sides of the bilayer, the transport calculation is performed with the Pauli spin-orbit Hamiltonian perturbatively included. The strength of the spin-orbit interaction is determined from the potential gradient within the atomic spheres.

The spin accumulation in the Cu is plotted in Figure 4.12 as a function of the distance to the Py/Cu interface. It exhibits an exponential decay following the spin diffusion theory [63]. With the real SO strength of bulk Cu, λ is found to be larger than 400 nm. If we artificially increase the SO strength of Cu by a factor of 7, the calculated λ is reduced to ~16 nm. In both cases, however, the spin accumulation at various positions is independent of the polarization directions, indicating that the bulk SO cannot account for the anisotropic spin relaxation in the Cu channels.

For the calculation with artificially increased spin-orbit strength, we merely multiply the real spin-orbit strength by a factor of 7 for Cu atomic spheres in the scattering region [64]. The scattering states at the Fermi level are obtained using the so-called "wave-function matching" [65] and the position-dependent spin accumulation is determined by calculating the local spin polarization of electrical current density [66].

Besides bulk, SO effects could also be present at surfaces and interfaces. Our experiments were carried out at low temperatures, where phonon scattering is mostly suppressed. The electrical resistivity arises mainly from defect and surface scattering. The surface SO effect [48], originating from inversion asymmetry across a surface results in spin relaxation when conduction electrons are scattered from the surfaces of the mesoscopic Cu channels. For two-dimensional graphene [34,35] the SO effect on the top and bottom surfaces can induce anisotropy between out-of-plane polarization (z spins) and in-plane polarization (x spins and y spins) but will not induce anisotropy between x spins and y spins. However, the Cu channels in our experiments have comparable width and thickness. Therefore, the SO contribution from the side surfaces

should be comparable to that from the top and bottom surfaces and could account for the observed anisotropy between *x* spins and *y* spins.

We take the Cartesian coordinate as shown in Figure 4.13 and the spins diffuse along the *y*-axis in the Cu channel. In the bulk region, where conduction electrons are not influenced by surface scattering, spin-relaxation rate is isotropic with respect to the spin orientation. When conduction electrons are close to a surface of the Cu channel, SO interaction at the surface results in an additional spin relaxation mechanism, as conceptually illustrated in Figure 4.13.

Here we consider the spin-relaxation rates of *x* and *y* spins under the perturbation of the Rashba-Sheka-Vasko type [31,32] SO Hamiltonians at the top/bottom and side surfaces, respectively. The SO Hamiltonian of the top/bottom surfaces lying in the *x* - *y* plane can be expressed as

$$H_R^{t/b} = \frac{\alpha_R}{\hbar}\sigma\cdot(\hat{z}\times\vec{p}) = \frac{\alpha_R}{\hbar}(p_x\sigma_y - p_y\sigma_x) = \frac{\alpha_R}{\hbar}\begin{pmatrix} 0 & -ip_x - p_y \\ ip_x - p_y & 0 \end{pmatrix} \quad (4.2)$$

where the α_R is is the surface SO strength, $\boldsymbol{\sigma}$ is the Pauli matrix and $\boldsymbol{p}$ is the electron momentum. This type of SO interaction was derived by Rashba and Sheka [31] for wurtzite type crystals, and then by Vasko [33] for two-dimensional electron gas. We define the eigenstates of σ_x and σ_y, i.e.

$$\begin{aligned} |\pm x\rangle &= \frac{1}{\sqrt{2}}\begin{pmatrix} 1 \\ \pm 1 \end{pmatrix} \\ |\pm y\rangle &= \frac{1}{\sqrt{2}}\begin{pmatrix} 1 \\ \pm i \end{pmatrix} \end{aligned} \quad (4.3)$$

as ±*x*-spins and ±*y*-spins, respectively.

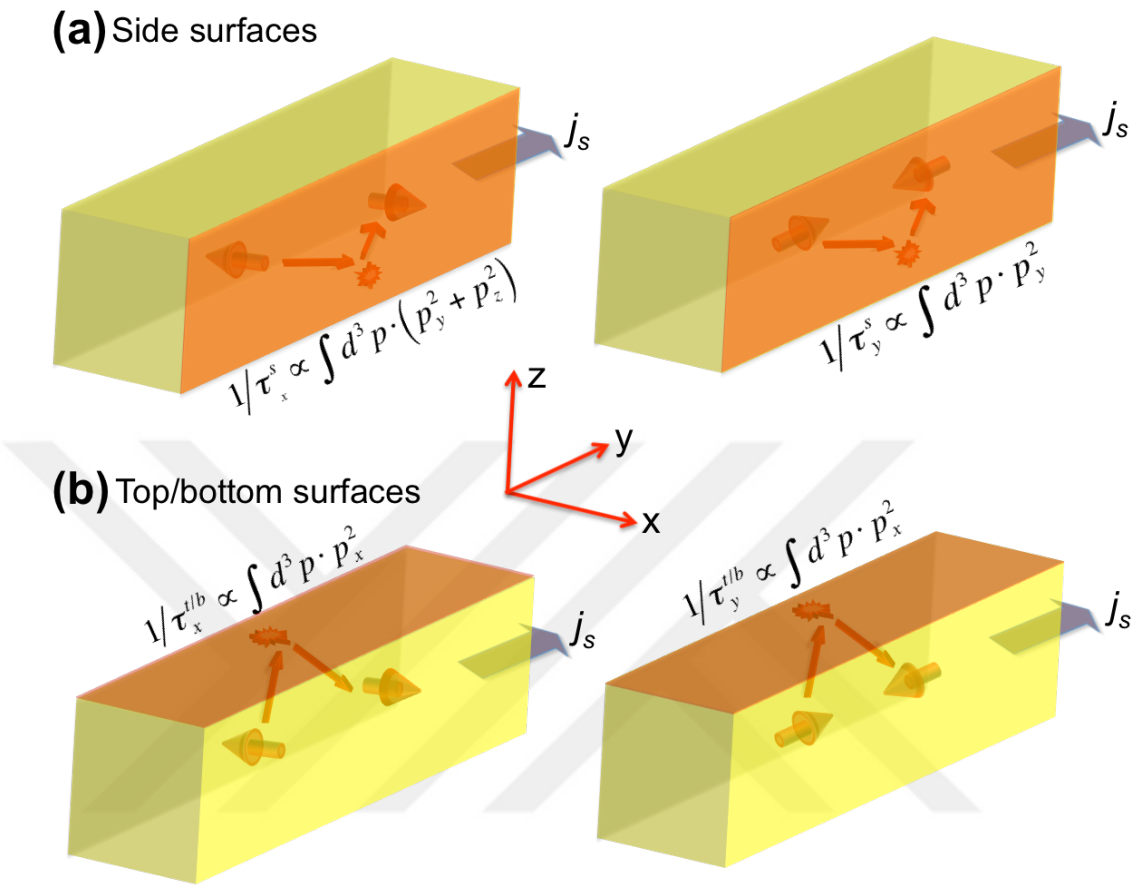

Figure 4.13: Surface spin-orbital effects. When electrons are scattered by a surface, the spin-flip probabilities are higher for spins perpendicular to the surface than for spins parallel to surface. (a) Scattering rate for *x* spins (on the left) is larger than scattering rate for *y* spins (on the right) on the side surfaces. (b) Scattering rate for *x* spins (on the left) is equal to scattering rate for *y* spins (on the right) on the top/bottom surfaces.

The spin-relaxation rate (inversely proportional to the spin-relaxation time) of the *x* spins due to the SO Hamiltonian Eq. (4.2) can be calculated via the Fermi golden rule [67]

$$\frac{1}{\tau_x^{t/b}} \propto \int d^3p \left| \left\langle +x \left| H_R^{t/b} \right| -x \right\rangle \right|^2 = \frac{\alpha_R^2}{\hbar^2} \int d^3p \cdot p_x^2 \tag{4.4}$$

The spin-relaxation rate of the *y* spins can be obtained in the same manner,

$$\frac{1}{\tau_y^{t/b}} \propto \int d^3p \left| \left\langle +y \left| H_R^{t/b} \right| -y \right\rangle \right|^2 = \frac{\alpha_R^2}{\hbar^2} \int d^3p \cdot p_x^2 \tag{4.5}$$

Here we find $1/\tau_x^{t/b} = 1/\tau_y^{t/b}$ indicating that the SO effect at the top/bottom surfaces as illustrated in Figure 4.13(b) does not introduce anisotropic spin-relaxation rate for *x* and *y* spins.

The side surfaces of the Cu channel offer another source of SO interaction, The SO Hamiltonian of the side surfaces lying in the *y* - *z* plane can be expressed as:

$$H_R^S = \frac{\alpha_R}{\hbar} \sigma \cdot (\hat{x} \times \vec{p}) = \frac{\alpha_R}{\hbar} (p_y \sigma_z - p_z \sigma_y) = \frac{\alpha_R}{\hbar} \begin{pmatrix} p_y & ip_z \\ -ip_z & -p_y \end{pmatrix} \tag{4.6}$$

using the eigenstates of σ_x and σ_y, given in the equation (4.3), the spin-relaxation rates of *x* spins and *y* spins can be calculated again perturbatively from the SO Hamiltonian of the side surfaces, and given by

$$\begin{aligned} \frac{1}{\tau_x^S} &\propto \int d^3p \left| \left\langle +x \left| H_R^S \right| -x \right\rangle \right|^2 = \frac{\alpha_R^2}{\hbar^2} \int d^3p \cdot (p_y^2 + p_z^2) \\ \frac{1}{\tau_y^S} &\propto \int d^3p \left| \left\langle +y \left| H_R^S \right| -y \right\rangle \right|^2 = \frac{\alpha_R^2}{\hbar^2} \int d^3p \cdot p_y^2 \end{aligned} \tag{4.7}$$

Therefore, the *y* spins have a smaller spin-relaxation rate and hence a longer spin-relaxation length than the *x* spins in the presence of the SO Hamiltonian of the side surfaces. The Rashba-Sheka-Vasko SO effect at the side surfaces of the Cu channel, which is illustrated in Figure 4.13(a), indeed results in anisotropic spin relaxation in agreement with our experimental measurement. Since we showed that the influence of the SO effect at the top and bottom surfaces lying in the *x* - *y* plane makes the same contribution to the spin-relaxation rates for *x* spins and *y* spins, the observed

anisotropic spin relaxation is a result of the SO interaction at the side surfaces of the Cu channels. Large SO effects on Cu (111) surfaces were experimentally observed [68] and theoretically justified [69,70]. For the polycrystalline NLSVs, high rates of spin relaxation on the surfaces of Cu channels [52] and SO effects on the surfaces of Ag channels covered with Bi_2O_3 [71] were reported.

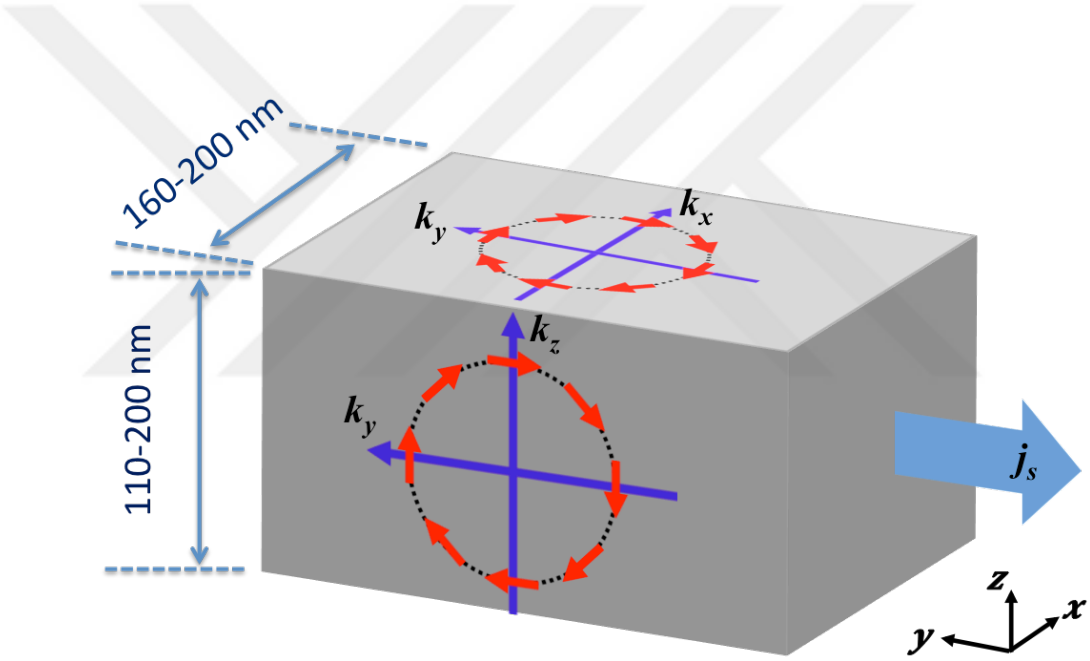

Figure 4.14: Sketch of the SO effective magnetic fields at the side and top surfaces of a Cu channel. Copyright 2017 by the American Physical Society.

The SO effective magnetic field is parallel to the surface and depends on the direction of electron momentum, as sketched in Figure 4.14. When an electron is moving in the vicinity of a surface, the effective magnetic field tends to align the electron spin with the direction of the field, and therefore causes relaxation of spins

that are not aligned with the field. For electrons near the side surfaces, the *x* spins are always perpendicular to the SO effective magnetic field of the side surfaces and consequently have a higher probability of spin relaxation than the *y* spins, which have finite components in the direction of the effective magnetic fields. For the top and bottom surfaces, the SO effective magnetic field rotates through the *x* - *y* plane and has the same effect on the spin relaxation for *y* spins and *x* spins. The SO effective electric field is perpendicular to the surfaces. It was demonstrated that the strength of SO interaction can be tuned by an applied electric field perpendicular to the surface via an electrostatic gate [48,49], indicating the possibility of manipulating the spin relaxation electrically.

The above interpretation does not depend on whether the spin relaxation is of Elliott-Yafet [24,25] (EY) or Dyakonov-Perel (DP) type [26]. The only assumption is that the electrons are under the influence of the SO effective magnetic field near the side surfaces. The spin-flip may occur upon momentum scattering (*i.e.* EY mechanism) or between momentum scattering events (*i.e.* DP mechanism). Both types would result in higher rates of spin relaxation for *x* spins than for *y* spins when electrons are moving near side surfaces. In principle, the EY and DP could coexist and contribute constructively to the anisotropic spin relaxation. The mechanisms could also be different between transport in the bulk and transport near surfaces. While EY is commonly viewed as the dominant mechanism in metals with bulk inversion symmetry, recent experimental [72] and theoretical [73] works point to the possibility of DP mechanism in Pt. Nevertheless, the λ_x versus ρ plots in Figures 4.10(a) and (b) for our two samples can be fitted reasonably well by the EY model.

The electron mean free paths in the Cu channels are relevant in the discussion of surface and bulk scattering. The momentum relaxation time τ_e can be estimated from Cu resistivity ρ using a Drude model $\tau_e = m/(\rho n e^2)$, where $n = 8.47 \times 10^{28}$ m^{-3} is Cu electron density [74], m is electron mass, and e is electron charge. The mean free path l is estimated by $l = v_F \tau_e$, where $v_f = 1.57 \times 10^6$ m/s is the Cu Fermi velocity [74]. The average ρ values at 10 K for NLSVs on samples A and B are both 1.8 μΩ·cm, yielding τ_e = 23.3 fs and l = 37 nm, which is obviously smaller than the Cu widths (w = 175 nm for A and w = 207 nm for B on average) and thicknesses (200 nm for A and 110 nm for B). Therefore, bulk momentum scattering dominates over surface scattering, and the electron transport is mainly diffusive. However, as the electrons diffuse in the Cu channel over a spin-relaxation length that is greater than the widths and thicknesses, there are still substantial surface scattering events.

The relation between the diffusion time τ_d and distance d is given by $d^2 = D\tau_d$, where D is the bulk diffusion constant. An application of this is $\lambda_{x(y)}^2 = D\tau_{x(y)}$, which links spin diffusion (relaxation) length and time. The diffusion constant can be evaluated by $D = 1/(\rho e^2 N)$ and $N = 3n/2E_F$, where N is the Fermi-level density of states and $E_F = 7.00$ eV is the Cu Fermi energy [74]. Electrons at the center of the cross-section of the Cu channel need to diffuse over $d = w/2$ in the ±x directions to reach the side surfaces. Using $d = w/2 = 88$ nm for sample A, the time for a diffusion distance of 88 nm in any direction is 405 fs. Considering the three possible dimensions for diffusion, the average time for electrons to diffuse 88 nm in ±x directions has to be increased by a factor of 3, yielding $\tau_e' = 1.22$ ps. The ratio $\tau_e'/\tau_e = 52$ indicates that an electron reaches a side surface after 52 bulk scattering events on average. From the average spin diffusion length λ_x = 1010 nm of sample A,

we estimate the spin-relaxation time $\tau_x = 53.4$ ps, which is the average diffusion time for an electron before a spin-flip event. During time interval τ_x, there are $\tau_x/\tau_e' = 44$ scattering events with the side surfaces. Similarly, we calculate ~34 scattering events with top and bottom surfaces of Cu channels (200 nm thick for A) during τ_x. The number of bulk scattering events during τ_x is $\tau_x/\tau_e = 2292$. Therefore, the overall bulk-to-surface scattering ratio is $2292/(44 + 34) = 29$. The spin relaxation and its anisotropy can be accounted for by assuming bulk spin-flip probabilities in the order of 10^{-4} and surface spin-flip probabilities in the order of 10^{-3} to 10^{-2}.

It is tempting to compare the magnitudes of the anisotropic effects between A and B, which have different thickness and thereby different areas of side surfaces. However, for a mainly diffusive Cu channel, a moderately reduced thickness actually forces the electrons to diffuse toward the side surfaces. Therefore, the anisotropic effect is not necessarily reduced for a thickness of 110 nm as compared to 200 nm. Quantitative comparison is challenging because of the various types of scattering and the variations of λ and ρ between devices. In Figure 4.9(e), it is reassuring to our interpretation that all data points from two samples scale with L/λ_x. If the Cu channel thickness is more drastically reduced, *e.g.*, to 10 nm, the scattering from top and bottom surfaces would be dominant and result in short spin diffusion lengths (< 100 nm), which makes NLSV measurements difficult. We propose for future work that many NLSVs can be fabricated under identical conditions, with Cu channels that have same thickness but different widths. Furthermore, values of ρ and λ have to be carefully evaluated and taken into account in the analysis.

4.6 Conclusions

In conclusion, we have demonstrated anisotropic spin relaxation in the mesoscopic metallic (Cu) channels of nonlocal spin valves. The spin signals for spins parallel to the spin current direction are higher than for spins perpendicular to it. The percentage signal difference between the two spin directions increases as a function of normalized channel length. Therefore, the origin of the effects is the anisotropic spin relaxation in the Cu channels instead of the anisotropic spin polarizations of spin injectors and detectors. The anisotropic differences in spin-relaxation lengths are as great as 9% at 10 K. Consequently, the spin current in the Cu channel can be tuned by its polarization direction. Surface spin-orbit effects of the Rashba-Sheka-Vasko type account for the observed anisotropy and offer the prospect of electrical tuning of spin currents via electrostatic gating.

REFERENCES

[1] C. Zhou*, F. Kandaz*, Y. Cai, C. Qin, M. Jia, Z. Yuan, Y. Wu, and Y. Ji, Phys. Rev. B **96**, 94413 (2017).

[2] S. O. Valenzuela and M. Tinkham, Nature **442**, 176 (2006).

[3] T. Kimura, Y. Otani, T. Sato, S. Takahashi, and S. Maekawa, Phys. Rev. Lett. **98**, 156601 (2007).

[4] I. M. Miron, G. Gaudin, S. Auffret, B. Rodmacq, A. Schuhl, S. Pizzini, J. Vogel, and P. Gambardella, Nat. Mater. **9**, 230 (2010).

[5] L. Liu, O. J. Lee, T. J. Gudmundsen, D. C. Ralph, and R. A. Buhrman, Phys. Rev. Lett. **109**, 96602 (2012).

[6] S. Mühlbauer, B. Binz, F. Jonietz, C. Pfleiderer, A. Rosch, A. Neubauer, R. Georgii, and P. Böni, Science (80-.). **323**, 915 (2009).

[7] X. Z. Yu, Y. Onose, N. Kanazawa, J. H. Park, J. H. Han, Y. Matsui, N. Nagaosa, and Y. Tokura, Nature **465**, 901 (2010).

[8] S. Emori, U. Bauer, S. Ahn, E. Martinez, and G. S. D. Beach, Nat. Mater. **12**, 611 (2013).

[9] G. Chen, J. Zhu, A. Quesada, J. Li, A. T. N. Diaye, Y. Huo, T. P. Ma, Y. Chen, H. Y. Kwon, C. Won, Z. Q. Qiu, A. K. Schmid, and Y. Z. Wu, Phys. Rev. Lett. **110**, 177204 (2013).

[10] S. Datta and B. Das, Appl. Phys. Lett. **56**, 665 (1990).

[11] H. C. Koo, J. H. Kwon, J. Eom, J. Chang, S. H. Han, and M. Johnson, Science **325**, 1515 (2009).

[12] W. Y. Choi, H.-J. Kim, J. Chang, S. H. Han, H. C. Koo, and M. Johnson, Nat. Nanotechnol. **10**, 666 (2015).

[13] A. Manchon, H. C. Koo, J. Nitta, S. M. Frolov, and R. A. Duine, Nat. Mater. **14**, 871 (2015).

[14] M. I. D'yakonov and V. I. Perel', JETP Lett. **13**, 467 (1971).

[15] M. I. D'yakonov and V. I. Perel', Phys. Lett. A **35**, 459 (1971).

[16] M. I. D'yakonov, Phys. Rev. Lett. **99**, 126601 (2007).

[17] H. Nakayama, M. Althammer, Y. T. Chen, K. Uchida, Y. Kajiwara, D. Kikuchi, T. Ohtani, S. Geprägs, M. Opel, S. Takahashi, R. Gross, G. E. W. Bauer, S. T. B. Goennenwein, and E. Saitoh, Phys. Rev. Lett. **110**, 206601 (2013).

[18] G. E. W. Bauer, E. Saitoh, and B. J. van Wees, Nat. Mater. **11**, 391 (2012).

[19] Y. Tserkovnyak, a Brataas, G. E. W. Bauer, and B. I. Halperin, Rev. Mod. Phys. **77**, 1375 (2005).

[20] N. S. Averkiev, L. E. Golub, and M. Willander, J. Phys. Condens. Matter **14**, R271 (2002).

[21] J. Fabian, A. Matos-Abiague, C. Ertler, P. Stano, and I. Zutic, Acta Phys. Slovaca **57**, 565 (2007).

[22] D. Huertas-Hernando, F. Guinea, and A. Brataas, Phys. Rev. Lett. **103**, 146801 (2009).

[23] S. Fratini, D. Gosálbez-Martínez, P. Merodio Cámara, and J. Fernández-Rossier, Phys. Rev. B **88**, 115426 (2013).

[24] Y. Mokrousov, H. Zhang, F. Freimuth, B. Zimmermann, N. H. Long, J. Weischenberg, I. Souza, P. Mavropoulos, and S. Blügel, J. Phys. Condens. Matter **25**, 163201 (2013).

[25] R. J. Elliott, Phys. Rev. **96**, 266 (1954).

[26] Y. Yafet, Phys. Lett. **98**, 287 (1983).

[27] M. I. D'yakonov and V. I. Perel', Sov. Phys. Solid State **13**, 3023 (1972).

[28] N. S. Averkiev, L. E. Golub, A. S. Gurevich, V. P. Evtikhiev, V. P. Kochereshko, A. V. Platonov, A. S. Shkolnik, and Y. P. Efimov, Phys. Rev. B **74**, 33305 (2006).

[29] A. Balocchi, T. Amand, G. Wang, B. L. Liu, P. Renucci, Q. H. Duong, and X. Marie, New J. Phys. **15**, 95016 (2013).

[30] P. Scarlino, E. Kawakami, P. Stano, M. Shafiei, C. Reichl, W. Wegscheider,

and L. M. K. Vandersypen, Phys. Rev. Lett. **113**, 256802 (2014).

[31] G. Dresselhaus, Phys.Rev. **100**, 580 (1955).

[32] V. I. Rashba, E.I. and Sheka, Sov. Phys. Solid State **1**, 143 (1959).

[33] F. T. Vasko, JETP Lett. **30**, 541 (1979).

[34] M. I. D'yakonov and V. Y. Kachororovskii, Sov. Phys. Semicond. **20**, 110 (1986).

[35] N. Tombros, S. Tanabe, A. Veligura, C. Jozsa, M. Popinciuc, H. T. Jonkman, and B. J. Van Wees, Phys. Rev. Lett. **101**, 46601 (2008).

[36] B. Raes, J. E. Scheerder, M. V. Costache, F. Bonell, J. F. Sierra, J. Cuppens, J. Van de Vondel, and S. O. Valenzuela, Nat. Commun. **7**, 11444 (2016).

[37] M. Johnson and R. H. Silsbee, Phys. Rev. Lett. **55**, 1790 (1985).

[38] F. J. Jedema, A. T. Filip, and B. J. Van Wees, Nature **410**, 345 (2001).

[39] F. J. Jedema, H. B. Heersche, A. T. Filip, J. J. A. Baselmans, and B. J. van Wees, Nature **416**, 713 (2002).

[40] T. Kimura, J. Hamrle, Y. Otani, K. Tsukagoshi, and Y. Aoyagi, Appl. Phys. Lett. **85**, 3501 (2004).

[41] S. O. Valenzuela and M. Tinkham, Appl. Phys. Lett. **85**, 5914 (2004).

[42] Y. Ji, A. Hoffmann, J. S. Jiang, and S. D. Bader, Appl. Phys. Lett. **85**, 6218 (2004).

[43] R. Godfrey and M. Johnson, Phys. Rev. Lett. **96**, 136601 (2006).

[44] T. Yang, T. Kimura, and Y. Otani, Nat. Phys. **4**, 851 (2008).

[45] Y. Fukuma, L. Wang, H. Idzuchi, S. Takahashi, S. Maekawa, and Y. Otani, Nat. Mater. **10**, 527 (2011).

[46] E. Villamor, M. Isasa, L. E. Hueso, and F. Casanova, Phys. Rev. B **87**, 94417 (2013).

[47] L. O'Brien, M. J. Erickson, D. Spivak, H. Ambaye, R. J. Goyette, V. Lauter, P. A. Crowell, and C. Leighton, Nat. Commun. **5**, 3927 (2014).

[48] Y. A. Bychkov and E. I. Rashba, JETP Lett. **39**, 66 (1984).

[49] J. Nitta, T. Akazaki, H. Takayanagi, and T. Enoki, Phys. Rev. Lett. **78**, 1335 (1997).

[50] E. Lesne, Y. Fu, S. Oyarzun, J. C. Rojas-Sánchez, D. C. Vaz, H. Naganuma, G. Sicoli, J.-P. Attané, M. Jamet, E. Jacquet, J.-M. George, A. Barthélémy, H. Jaffrès, A. Fert, M. Bibes, and L. Vila, Nat. Mater. **15**, 1261 (2016).

[51] H. Zou and Y. Ji, Appl. Phys. Lett. **101**, 82401 (2012).

[52] Y. Ji, A. Hoffmann, J. E. Pearson, and S. D. Bader, Appl. Phys. Lett. **88**, 52509 (2006).

[53] T. Kimura, T. Sato, and Y. Otani, Phys. Rev. Lett. **100**, 66602 (2008).

[54] H. Zou, X. J. Wang, and Y. Ji, J. Vac. Sci. Technol. B **28**, 1314 (2010).

[55] Y. Cai, Y. Luo, C. Zhou, C. Qin, S. Chen, Y. Wu, and Y. Ji, J. Phys. D. Appl. Phys. **49**, 185003 (2016).

[56] M. Johnson, Phys. Rev. Lett. **70**, 2142 (1993).

[57] E. Y. Tsymbal and I. Zutic, *Handbook of Spin Transport and Magnetism* (CRC Press, Boca Raton FL, 2012).

[58] M. Johnson and R. H. Silsbee, Phys. Rev. B - Condens. Matter Mater. Phys. **76**, 153107 (2007).

[59] X. J. Wang, H. Zou, and Y. Ji, Phys. Rev. B **81**, 104409 (2010).

[60] Y. Cai, Y. Luo, C. Qin, S. Chen, Y. Wu, and Y. Ji, J. Magn. Magn. Mater. **405**, 145 (2016).

[61] Y. Liu, A. A. Starikov, Z. Yuan, and P. J. Kelly, Phys. Rev. B **84**, 14412 (2011).

[62] I. Turek, V. Drchal, J. Kudrnovsky, M. Sob, and P. Weinberger, *Electronic Structure of Disordered Alloys, Surfaces and Interfaces* (Kluwer, Dordrecht, 1997).

[63] O. K. Andersen, Z. Pawlowska, and O. Jepsen, Phys. Rev. B **34**, 5253 (1986).

[64] J. Bass and W. P. Pratt, J. Phys. Condens. Matter **19**, 183201 (2007).

[65] Z. Yuan, Y. Liu, A. A. Starikov, P. J. Kelly, and A. Brataas, Phys. Rev. Lett. **109**, 267201 (2012).

[66] K. Xia, M. Zwierzycki, M. Talanana, P. J. Kelly, and G. E. W. Bauer, Phys. Rev. B **73**, 64420 (2006).

[67] L. Wang, R. J. H. Wesselink, Y. Liu, Z. Yuan, K. Xia, and P. J. Kelly, Phys. Rev. Lett. **116**, 196602 (2016).

[68] J. J. Sakurai, *Modern Quantum Mechanics*, Revised ed (Addison-Wesley, Reading, MA, 1994).

[69] A. Tamai, W. Meevasana, P. D. C. King, C. W. Nicholson, A. De La Torre, E. Rozbicki, and F. Baumberger, Phys. Rev. B **87**, 75113 (2013).

[70] H. Ishida, Phys. Rev. B **90**, 235422 (2014).

[71] L. Petersen and P. Hedegård, Surf. Sci. **459**, 49 (2000).

[72] S. Karube, H. Idzuchi, K. Kondou, Y. Fukuma, and Y. Otani, Appl. Phys. Lett. **107**, 122406 (2015).

[73] J. Ryu, M. Kohda, and J. Nitta, Phys. Rev. Lett. **116**, 256802 (2016).

[74] N. H. Long, P. Mavropoulos, D. S. G. Bauer, B. Zimmermann, Y. Mokrousov, S. Bl, and P. Gr, Phys. Rev. B **94**, 180406 (2016).

[75] N. W. Ashcroft and N. D. Mermin, *Solid State Physics* (Saunders College Publishing, Philadelphia, PA, 1976).

Chapter 5

UNSOLVED QUESTIONS AND FUTURE WORK

5.1 Unsolved Questions

While exploring anisotropic measurements, we also observed a small difference between the spin signals for +*y*-direction spins and –*y*-direction spins. Figure 5.1 shows the measured R_s as a function of the applied magnetic field B_y in the *y* direction. When a large magnetic field is applied in +*y* (-*y*) direction, the spins of F_1

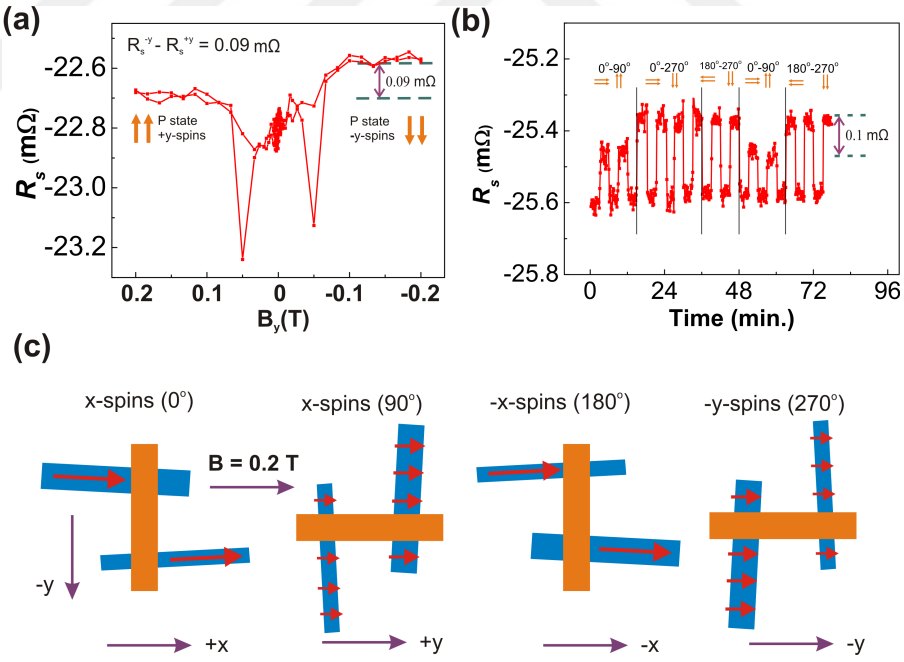

Figure 5.1: (a) The R_s versus B_y curve. (b) The R_s versus time plot at 295 K while the same NLSV is rotated between 0°, 90°, 180°, and 270° under a 0.2-T magnetic field. c) Illustrates the rotation of the NLSV relative to the fixed magnetic field, the spins alternate between the +*x*, +*y*, -*x*, and –*y* directions.

and F2 are aligned parallel in the +*y* (-*y*) direction, and therefore we can compare the R_s values corresponding to +*y*- and –*y*-direction parallel states; R_s^{+y} and R_s^{-y}. It is observed that the R_s^{-y} is 0.09 mΩ higher than the R_s^{+y}. The same NLSV device is also rotated in a 0.2 T magnetic field between the 0°, 90°, 180°, and 270° to alternate the P state spin configurations between the +*x*, +y, –x and –y directions as shown in Figure 5.1(c). A difference of 0.1 mΩ in R_s change is observed as shown in figure 5.1(b), with the parallel states of -*y* spins (270°) being higher than the P states of +*y* spins (90°). In contrast, the R_s values for 0° and 180° positions are the same.

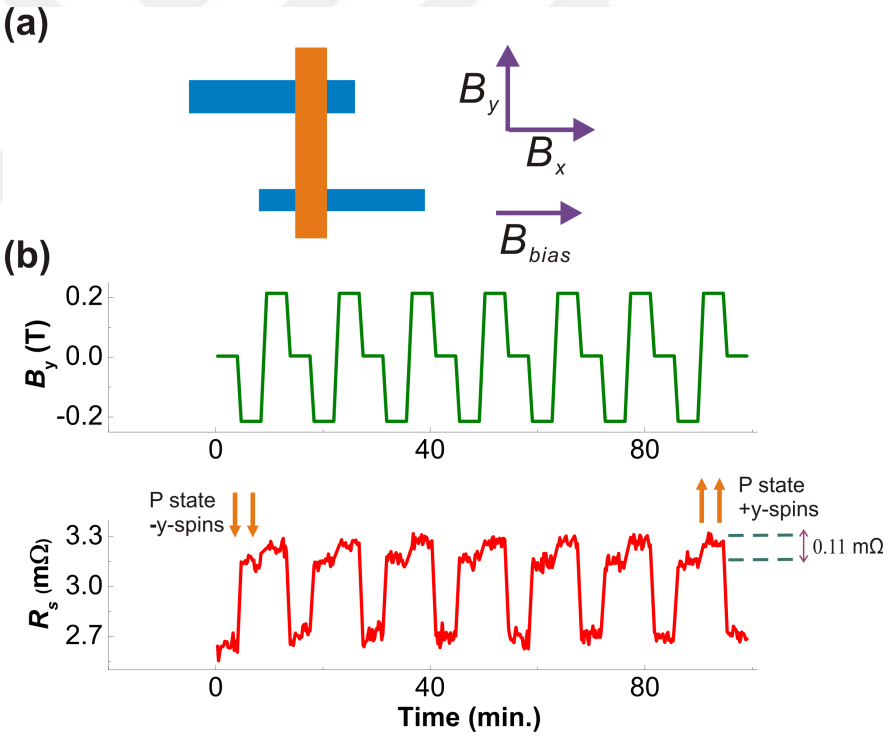

Figure 5.2: (a) Illustration of a fixed bias field B_{bias} in the *x* direction. (b) The applied field in *y* direction B_y as a function of time and the R_s as a function of time.

Similar results is also obtained using the rotating-field method in which 0.2 T applied magnetic field is alternated periodically between three values: 0 T, -0.2 T, and +0.2 T in the presence of a bias field. In this case the spins of F_1 and F_2 are always parallel but alternate between the +*x*, -*y*, and +*y* directions. A small R_s change is observed for +*y* and –*y* direction spins, with the R_s for P state along +*y* direction being higher than that of the –*y* direction [Fig. 5.2]. However, this difference is much smaller than the difference of ~1.5 mΩ between the *x*- and *y*-spins.

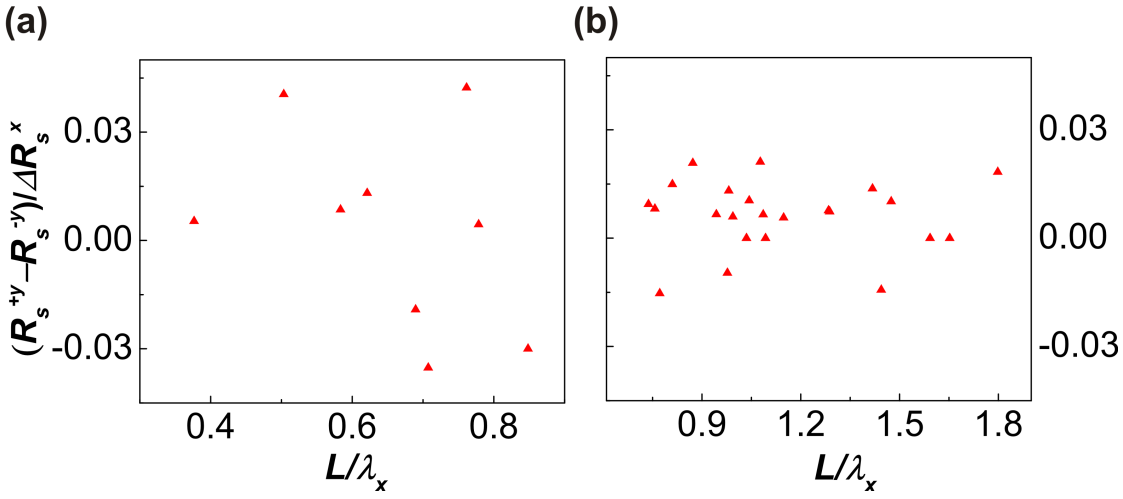

Figure 5.3: (a) The $(R_s^{+y} - R_s^{-y})/\Delta R_s^x$ versus L/λ_x for NLSVs on substrate A. (b) The $(R_s^{+y} - R_s^{-y})/\Delta R_s^x$ versus L/λ_x for devices on substrate B.

Using the rotating-field method, the difference of R_s values between +*y* and –*y* directions are systematically measured for NLSV devices from substrates A and B, which are used in Chapter 4 of this dissertation. Percentage signal change $(R_s^{+y} - R_s^{-y})/\Delta R_s^x$ is plotted as a function of L/λ_x in Figure 5.3. It is observed that for some devices the R_s^{+y} is larger and for some other devices the R_s^{-y} is larger. As can be

seen in figure 5.3, the percentage signal change does not depend on the normalized Cu channel length. Therefore the origin of the signal difference between +*y*- and –*y*-direction spins might be spin polarizations of the magnetic electrodes. However, further experiments are necessary to fully understand the effects.

5.2 Suggestions for Future Work

In chapter 4, we concluded that the origin of the anisotropic spin relaxation in the Cu channel is the spin-orbital effects (Rashba-Sheka-Vasko type [1–3]) on the side or top/bottom surfaces of the channel. We considered the spin-relaxation rates of *x* spins and *y* spins under the perturbation of the Rashba-Sheka-Vasko type SO Hamiltonians at the side surfaces (perpendicular to *x* channel). These calculations proved that spin-relaxation rates are higher for *x* spins than those for *y* spins. If SO effects are also present on the top and bottom surfaces, spin-relaxation rate for *z* spins could also be greater than *y* spins. Therefore, the spin signals related to *z* spins can be measured in the future.

A series of experiments can be designed to further confirm the physical origin of the anisotropic spin signals. First, the signal of the *z*-direction spins can be compared to those of the *y*-direction and *x*-direction spins. Figure 5.4 shows an illustration of spin transport for *x*-, *y*-, and *z*-direction spins. These experiments can be done with two different methods, either rotating the magnetic field toward the *z* direction, or rotating the sample stage relative to the magnetic field. The SO effects on the top and bottom surfaces (perpendicular to *z* direction) could result in increase of spin-relaxation rate for z-direction spins. Therefore, spin-relaxation length for *z*-direction spins should have shorter than *y*-direction spins. If this is observed, it will

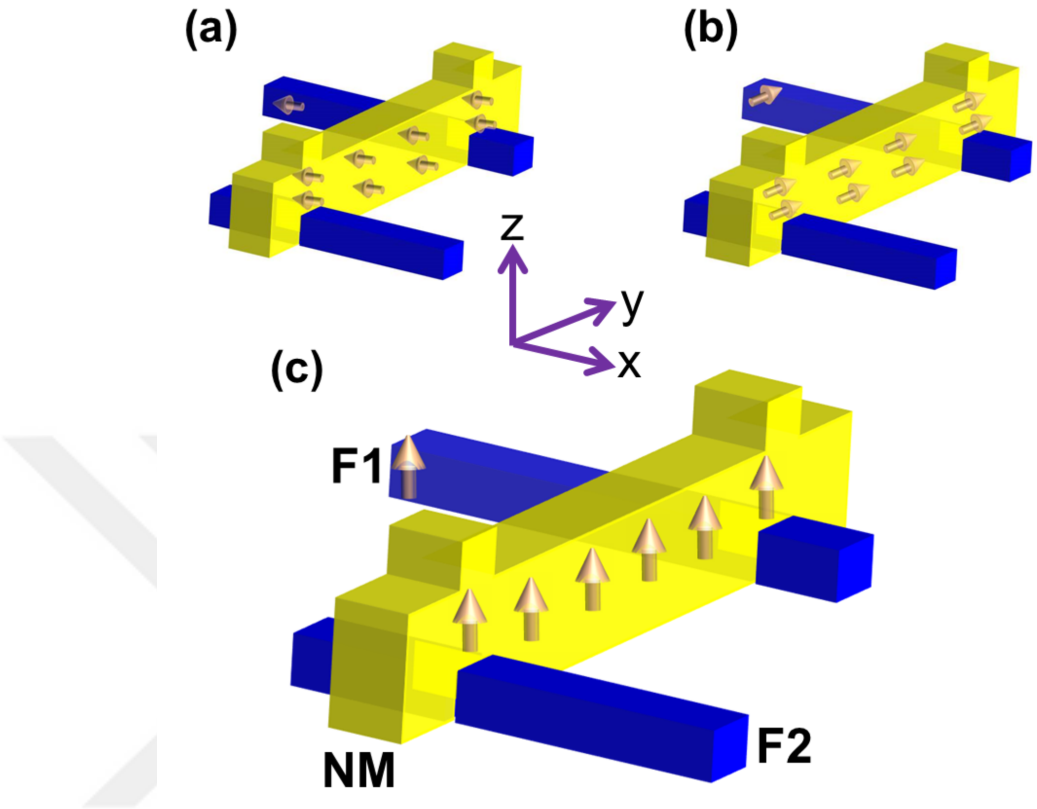

Figure 5.4: Illustration of anisotropic spin transport. The spins are aligned in the (a) *x*, (b) *y*, and (c) *z* direction.

further verify the anisotropy of spin signals and spin-orbital effects on the surfaces of Cu channel.

The SO Hamiltonian of the top/bottom surfaces lying in the *x*-*y* plane can be expressed as [1,2],

$$H_R^{t/b} = \frac{\alpha_R}{\hbar}\sigma\cdot(\hat{z}\times\vec{p}) = \frac{\alpha_R}{\hbar}(p_x\sigma_y - p_y\sigma_x) = \frac{\alpha_R}{\hbar}\begin{pmatrix} 0 & -ip_x - p_y \\ ip_x - p_y & 0 \end{pmatrix} \quad (5.1)$$

Spin-relaxation rates for the electrons with *x* spins and *y* spins were calculated via the Fermi golden rule and obtained,

$$\frac{1}{\tau_x^{t/b}} = \frac{1}{\tau_y^{t/b}} = \frac{\alpha_R^2}{\hbar^2}\int d^3p \cdot p_x^2 \tag{5.2}$$

The z spins are represented as the eigenstates of σ_z, i.e.

$$\begin{aligned} \left|+z\right\rangle &= \begin{pmatrix} 1 \\ 0 \end{pmatrix} \\ \left|-z\right\rangle &= \begin{pmatrix} 0 \\ 1 \end{pmatrix} \end{aligned} \tag{5.3}$$

The spin-relaxation rate of the z spins can be obtained in the same manner,

$$\frac{1}{\tau_z^{t/b}} \propto \int d^3p \left|\left\langle +z\left|H_R^{t/b}\right|-z\right\rangle\right|^2 = \frac{\alpha_R^2}{\hbar^2}\int d^3p \cdot (p_x^2 + p_y^2) \tag{5.4}$$

Here we find that spin-relaxation rate for the electrons with z spins is larger than x and y spins on the top and bottom surfaces, indicating that Rasba effect on the top/bottom surfaces reduce the spin-relaxation time of z spins. Similar calculations also show that spin-relaxation rate for the electrons with z spins and y spins is equal on the side surfaces,

$$\frac{1}{\tau_z^S} = \frac{1}{\tau_y^S} \propto \frac{\alpha_R^2}{\hbar^2}\int d^3p \cdot p_z^2 \tag{5.5}$$

Therefore, the electrons with z spins have shorter spin-relaxation length than y spins in the Cu channel.

Another possible future study could be comparing the spin signals for the x- and z-direction spins. In this way, the effects of the side and top/bottom surfaces can be investigated. Because, both x-direction and z-direction spins are perpendicular to Cu channel (y direction) but each of those spin signals are affected by different surfaces; x spins by side surfaces and z spins by top/bottom surfaces.

As changing the thickness and width of the Cu channels systematically, the anisotropic effects can be measured. Changing the dimensions of the Cu channel will affect the relative influences of side and top/bottom surfaces. Thickness can be in the range of 30 nm to 300 nm and width be in the range of 100 nm to 300 nm. For instance, it is expected that thicker and narrower Cu channels [Fig. 5.5(a)] should have more influence from side surfaces. This will cause higher spin-relaxation rate for the

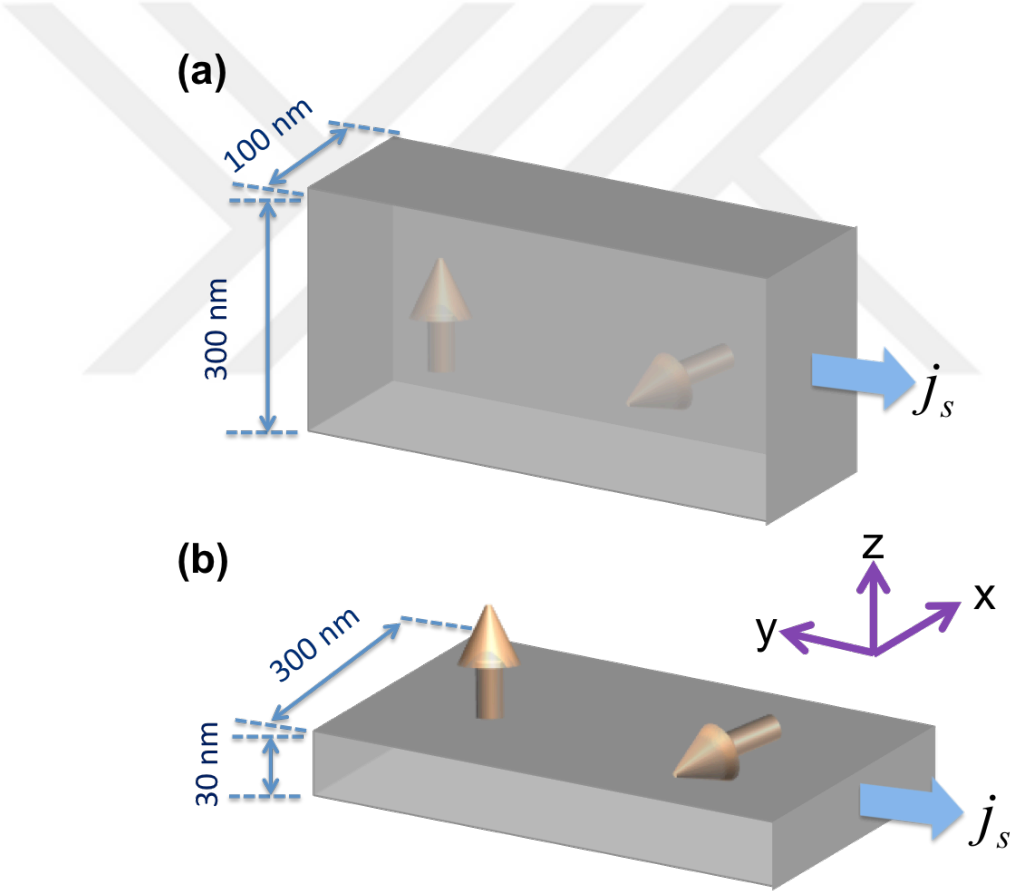

Figure 5.5: Illustration of anisotropic effects as changing the dimensions of Cu channels. (a) 300-nm thick and 100-nm wide Cu channel should have little influence from the top and bottom surfaces. (b) 30-nm thick and 300-nm wide Cu channel should have little influence from the side surfaces.

x-direction spins than *z*-direction spins. On the other hand, thinner and wider Cu channels [Fig. 5.5(b)] should have more influence from top/bottom surfaces and it will cause higher spin-relaxation rate for *z*-direction spins than *x*-direction spins. The thickness and width of the Cu channels can be systematically changed and anisotropic signal measurements can be carried out for these NLSVs. Changing the dimensions of Cu channels will also change the resistivity and spin-relaxation length in the channel. This research allows studying the anisotropic effects in wider range of λ values.

It can also be interesting to study anisotropic effects by tuning the surface conditions of Cu channels. In previous studies, enhanced spin-relaxation lengths for *x* spins have been observed during the natural oxidation of the NM channels [4,5]. Anisotropic effects can be investigated by measuring the particular NLSVs as those oxidized in air over time. The spin-orbital effects can be increased on the surfaces of the Cu channels by covering the surfaces with a heavy metal (such as Pt or Bi). Therefore, using these Cu/heavy metal systems, which have strong SO effects, in the NLSVs, stronger anisotropic effects can be observed. Inversion symmetry breaking can be enhanced on the surfaces of Cu channels by evaporating the AlO_x, WO_x, or TaO_x on the surfaces of the channels. Inversion symmetry breaking is essential for SO effects.

Anisotropic effects can also be investigated on the surfaces of different nonmagnetic channel materials such as Au, Ag and Al. Surface conditions and channel dimensions can also be varied with these materials and the anisotropic effects can be explored.

Rashba effective fields can be modulated by an electric field applied perpendicular to surface. Hence, according to our postulate, the spin-relaxation length

should have been changed by an electrostatic gating. The anisotropic measurements can be performed under the electric field and the results can be compared with the measurements performed without the electric field. The measurements can also be done as changing the gate voltages. If changing gate voltage indeed modulates the accumulation of spin currents, then it will further confirm that Rashba mechanism on the surfaces is the origin of the anisotropic spin relaxation.

REFERENCES

[1] V. I. Rashba, E.I. and Sheka, Sov. Phys. Solid State **1**, 143 (1959).

[2] F. T. Vasko, JETP Lett. **30**, 541 (1979).

[3] Y. A. Bychkov and E. I. Rashba, JETP Lett. **39**, 78 (1984).

[4] H. Zou and Y. Ji, Appl. Phys. Lett. **101**, 82401 (2012).

[5] X. J. Wang, H. Zou, and Y. Ji, Phys. Rev. B **81**, 104409 (2010).

Chapter 6

CONCLUSION

In this dissertation, various experiments are designed to investigate anisotropic spin transport in mesoscopic nonmagnetic Cu channels of lateral non-local spin valves (NLSV). The NLSV devices are fabricated by electron beam lithography followed by an angle evaporation technique. The measurements are performed by using lock-in techniques with a rotatable sample stage in an electromagnet or with a rotating magnetic field. Low temperature has been achieved either in a variable temperature probe station or in a pulse-tube cryostat. Anisotropic spin relaxation in mesoscopic polycrystalline Cu channels is observed in these experiments and it is attributed to the spin-orbital effects of the Rashba-Sheka-Vasko type [1–3] on the surfaces of the Cu channels.

We define the sample substrate plane as the *x*-*y* plane of the coordinate system, with y direction being parallel to the Cu channel and x direction being perpendicular to the Cu channel. In the first type of experiments, specially designed NLSV devices with tilted F_1 and F_2 electrodes are used. With this special design, an antiparallel state between F_1 and F_2 can be reached even with magnetic field scans in the y direction. The spin signals for *x* spins and *y* spins are measured with magnetic fields applied in the *x* and *y* directions, respectively. A clear difference in signals between *x* spins and *y* spins are observed, and provides the initial evidence for anisotropic spin transport. In the second type of experiments, the same NLSV device is rotated in a fixed 0.2 T magnetic field between 0° and 90° periodically to alternate the spins between the *x*-

spin P state and *y*-spin P state, respectively. Periodic R_s change is observed with the P state of the *y*-spins (90°) higher than the P state of *x*-spins (0°), confirming the anisotropic signals. To obtain an accurate anisotropic signal, the small baseline change induced by subtle mechanical motions of measurement circuits during rotations is subtracted. The anisotropic signal measured in the second type of experiments matches the anisotropic spin signal observed in the first type of experiments. These two types of experiments are carried out at room temperatures.

In the third type of experiments, we rotate the magnetic field between x direction and y direction instead of rotating the samples. In this method, we completely eliminate any possible baseline change, which could be induced by the motion of samples and circuits. The rotating magnetic field is realized by a bias field $B_{bias} \sim 0.03$ T in the *x* direction from a permanent magnet and a variable applied field By in the y direction from an electromagnet. The purpose of the bias field is to align the F_1 and F_2 into a good x-spin P state under zero applied field. The spin signal R_s is measured constantly while applied magnetic field in the y direction is alternated periodically among three values: 0 T, -0.2 T, and +0.2 T in the presence of the bias field. In this case the spins in F_1 and F_2 electrodes remain parallel but alternate between the +*x*, -*y*, and +*y* directions. The sample temperature remains 10 K in this method. It is observed that the R_s values correspond to the P state of *y* spins is higher than the R_s values correspond to the P states of *x* spins, and provides clear evidence for an anisotropic spin signal at 10 K.

In the next step, systematic measurements of anisotropic spin signals for NLSVs of various channel lengths *L* are carried out to investigate the origin of the anisotropic spin signals. There are two possible origins: either the spin polarizations F_1

and F_2 are anisotropic or the Cu spin-relaxation length λ is anisotropic. These two possibilities imply different dependence of anisotropic signal on the channel length L. The experimental anisotropic spin signals from many NLSV devices on two substrates are plotted as a function of Cu channel length L and normalized channel length L/λ_x. An increasing trend is clearly observed and indicates that the anisotropic spin signals originate from the anisotropic spin relaxation in the Cu channels. The observed anisotropic differences in spin-relaxation lengths are as great as 9% at 10 K.

Finally, the origin of the anisotropic spin relaxation in the Cu channel is attributed to spin-orbit interactions on the surfaces of the Cu channels. The lack of inversion symmetry on the surfaces of mesoscopic Cu channels induces Rashba-Sheka-Vasko type spin-orbital effect. This SO effect induces spin-flip scatterings and the calculations by perturbation method gives different probabilities of spin-flip scatterings at side surfaces for different spin directions. Because the Rashba effects can be modulated by an electric field near the surface, the finding offers the prospect of electrical tuning of large spin currents via electrostatic gating.

REFERENCES

[1] V. I. Rashba, E.I. and Sheka, Sov. Phys. Solid State **1**, 143 (1959).

[2] F. T. Vasko, JETP Lett. **30**, 541 (1979).

[3] Y. A. Bychkov and E. I. Rashba, JETP Lett. **39**, 78 (1984).

Appendix

REPRINT PERMISSION LETTERS

Reprint Permission for Figure 1.1:

Figure 1.1: Reprinted by permission from [K. Fujiwara, Y. Fukuma, J. Matsuno, H. Idzuchi, Y. Niimi, Y. Otani, and H. Takagi, Nature Communications, 4, 1-6, 2013].

Copyright 2013 Macmillan Publishers Limited.

SPRINGER NATURE LICENSE TERMS AND CONDITIONS

This Agreement between Fatih Kandaz ("You") and Springer Nature ("Springer Nature") consists of your license details and the terms and conditions provided by Springer Nature and Copyright Clearance Center.

License Number	4270670969617
License date	Jan 16, 2018
Licensed Content Publisher	Springer Nature
Licensed Content Publication	Nature Communications
Licensed Content Title	5d iridium oxide as a material for spin-current detection
Licensed Content Author	Kohei Fujiwara, Yasuhiro Fukuma, Jobu Matsuno, Hiroshi Idzuchi, Yasuhiro Niimi et al.
Licensed Content Date	Dec 11, 2013
Licensed Content Volume	4
Type of Use	Thesis/Dissertation
Requestor type	academic/university or research institute
Format	print and electronic
Portion	figures/tables/illustrations
Number of	1

figures/tables/illustrations	
High-res required	no
Will you be translating?	no
Circulation/distribution	>50,000
Author of this Springer Nature content	no
Title	Anisotropic Spin Relaxation in Mesoscopic Nonmagnetic Channels
Instructor name	Fatih Kandaz
Institution name	University of Delaware
Expected presentation date	Jan 2018
Portions	Figure 2 (a)
Requestor Location	Fatih Kandaz 217 Sharp Lab Newark, DE 19716 United States Attn:
Billing Type	Invoice
Billing Address	Fatih Kandaz 217 Sharp Lab Newark, DE 19716 United States Attn:
Total	0.00 USD

Reprint Permission for Figure 2.1(b):

Figure 2.1(b): Reprinted with permission from [M. N. Baibich, J. M. Broto, A. Fert, F. Nguyen Van Dau, and F. Petroff, Physical Review Letters, 61, 2472, 1988]. Copyright 1988 by the American Physical Society

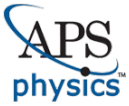

American Physical Society
Reuse and Permissions License

16-Jan-2018

This license agreement between the American Physical Society ("APS") and Fatih Kandaz ("You") consists of your license details and the terms and conditions provided by the American Physical Society and SciPris.

Licensed Content Information

License Number:	**RNP/18/JAN/000550**
License date:	16-Jan-2018
DOI:	10.1103/PhysRevLett.61.2472
Title:	Giant Magnetoresistance of (001)Fe/(001)Cr Magnetic Superlattices
Author:	M. N. Baibich et al.
Publication:	Physical Review Letters
Publisher:	American Physical Society
Cost:	USD $ 0.00

Request Details

Does your reuse require significant modifications: No

Specify intended distribution locations:	Worldwide
Reuse Category:	Reuse in a thesis/dissertation
Requestor Type:	Student
Items for Reuse:	Figures/Tables
Number of Figure/Tables:	1
Figure/Tables Details:	Figure 3
Format for Reuse:	Print and Electronic
Total number of print copies:	Up to 1000

Information about New Publication:

University/Publisher:	University of Delaware
Title of dissertation/thesis:	Anisotropic Spin Relaxation in Mesoscopic Nonmagnetic Channels
Author(s):	Fatih Kandaz
Expected completion date:	Jan. 2018

License Requestor Information

Name:	Fatih Kandaz
Affiliation:	Individual
Email Id:	fatihk@udel.edu
Country:	United States

Reprint Permission for Figure 2.6:

Figure 2.6: Reprinted by permission from [M. Johnson and R.H. Silsbee, Physical Review Letters, 55, 1790, 1985].

Copyright 1985 by the American Physical Society.

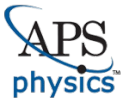

American Physical Society
Reuse and Permissions License

16-Jan-2018

This license agreement between the American Physical Society ("APS") and Fatih Kandaz ("You") consists of your license details and the terms and conditions provided by the American Physical Society and SciPris.

Licensed Content Information

License Number:	**RNP/18/JAN/000536**
License date:	16-Jan-2018
DOI:	10.1103/PhysRevLett.55.1790
Title:	Interfacial charge-spin coupling: Injection and detection of spin magnetization in metals
Author:	Mark Johnson and R. H. Silsbee
Publication:	Physical Review Letters
Publisher:	American Physical Society
Cost:	USD $ 0.00

Request Details

Does your reuse require significant modifications: No

Specify intended distribution locations:	Worldwide
Reuse Category:	Reuse in a thesis/dissertation
Requestor Type:	Student
Items for Reuse:	Figures/Tables
Number of Figure/Tables:	1
Figure/Tables Details:	Figure 1 (c)
Format for Reuse:	Electronic and Print
Total number of print copies:	Up to 1000

Information about New Publication:

University/Publisher:	University of Delaware
Title of dissertation/thesis:	Anisotropic Spin Relaxation in Mesoscopic Nonmagnetic Channels
Author(s):	Fatih Kandaz
Expected completion date:	Jan. 2018

License Requestor Information

Name:	Fatih Kandaz
Affiliation:	Individual
Email Id:	fatihk@udel.edu
Country:	United States

Reprint Permission for Figure 2.7:

Figure 2.7: Reprinted by permission from [F. J. Jedema, A. T. Filip, and B.J. van Wees, Nature, 410, 345, 2001].

Copyright 2001 Macmillan Magazines Limited.

SPRINGER NATURE LICENSE TERMS AND CONDITIONS

This Agreement between Fatih Kandaz ("You") and Springer Nature ("Springer Nature") consists of your license details and the terms and conditions provided by Springer Nature and Copyright Clearance Center.

License Number	4270640532192
License date	Jan 16, 2018
Licensed Content Publisher	Springer Nature
Licensed Content Publication	Nature
Licensed Content Title	Electrical spin injection and accumulation at room temperature in an all-metal mesoscopic spin valve
Licensed Content Author	F. J. Jedema, A. T. Filip, B. J. van Wees
Licensed Content Date	Mar 15, 2001
Licensed Content Volume	410
Licensed Content Issue	6826
Type of Use	Thesis/Dissertation
Requestor type	academic/university or research institute
Format	print and electronic
Portion	figures/tables/illustrations
Number of figures/tables/illustrations	2
High-res required	no
Will you be translating?	no
Circulation/distribution	>50,000
Author of this Springer Nature content	no

Title	Anisotropic Spin Relaxation in Mesoscopic Nonmagnetic Channels
Instructor name	Fatih Kandaz
Institution name	University of Delaware
Expected presentation date	Jan 2018
Portions	Figure 1, Figure 2 (a) and (b)
Requestor Location	Fatih Kandaz 217 Sharp Lab Newark, DE 19716 United States Attn:
Billing Type	Invoice
Billing Address	Fatih Kandaz 217 Sharp Lab Newark, DE 19716 United States Attn:
Total	0.00 USD

Reprint Permission for Figure 2.8:

Figure 2.8: Reprinted by permission from [F. J. Jedema, H. B. Heersche, A. T. Filip, J. J. A. Baselmans, and B.J. van Wees, Nature, 416, 713, 2002].

Copyright 2002 Macmillan Magazines Limited.

SPRINGER NATURE LICENSE TERMS AND CONDITIONS

This Agreement between Fatih Kandaz ("You") and Springer Nature ("Springer Nature") consists of your license details and the terms and conditions provided by Springer Nature and Copyright Clearance Center.

License Number	4270651106317
License date	Jan 16, 2018
Licensed Content Publisher	Springer Nature
Licensed Content Publication	Nature
Licensed Content Title	Electrical detection of spin precession in a metallic mesoscopic spin valve
Licensed Content Author	F. J. Jedema, H. B. Heersche, A. T. Filip, J. J. A. Baselmans, B. J. van Wees
Licensed Content Date	Apr 18, 2002
Licensed Content Volume	416
Licensed Content Issue	6882
Type of Use	Thesis/Dissertation
Requestor type	academic/university or research institute
Format	print and electronic
Portion	figures/tables/illustrations
Number of figures/tables/illustrations	2
High-res required	no
Will you be translating?	no
Circulation/distribution	>50,000
Author of this Springer Nature	no

content	
Title	Anisotropic Spin Relaxation in Mesoscopic Nonmagnetic Channels
Instructor name	Fatih Kandaz
Institution name	University of Delaware
Expected presentation date	Jan 2018
Portions	Figure 1 (a) and Figure 2 (a)
Requestor Location	Fatih Kandaz 217 Sharp Lab Newark, DE 19716 United States Attn:
Billing Type	Invoice
Billing Address	Fatih Kandaz 217 Sharp Lab Newark, DE 19716 United States Attn:
Total	0.00 USD

Reprint Permission for Chapter 4:

Dear Dr. Kandaz,

As the author, you have the right to use the article or a portion of the article in a thesis or dissertation without requesting permission from APS, provided the bibliographic citation and the APS copyright credit line are given on the appropriate pages.

Best wishes,

Jamie Casey
Consortia Coordinator
American Physical Society
http://librarians.aps.org/

American Physical Society
Reuse and Permissions License

19-Jan-2018

This license agreement between the American Physical Society ("APS") and Fatih Kandaz ("You") consists of your license details and the terms and conditions provided by the American Physical Society and SciPris.

Licensed Content Information

License Number:	**RNP/18/JAN/000689**
License date:	19-Jan-2018
DOI:	10.1103/PhysRevB.96.094413
Title:	Anisotropic spin relaxation induced by surface spin-orbit effects
Author:	Chao Zhou et al.
Publication:	Physical Review B
Publisher:	American Physical Society
Cost:	USD $ 0.00

Request Details

Does your reuse require significant modifications: No

Specify intended distribution locations:	Worldwide
Reuse Category:	Reuse in a thesis/dissertation
Requestor Type:	Author of requested content
Items for Reuse:	Whole Article
Format for Reuse:	Print and Electronic
Total number of print copies:	More Than 10000

Information about New Publication:

University/Publisher:	University of Delaware
Title of dissertation/thesis:	Anisotropic Spin Relaxation in Mesoscopic Nonmagnetic Channels
Author(s):	Fatih Kandaz
Expected completion date:	Jan. 2018

License Requestor Information

Name:	Fatih Kandaz
Affiliation:	Individual
Email Id:	fatihk@udel.edu
Country:	United States